ABSTRACT

CAO, YANG. Fabrication, Control, and Applications of Programmable Soft Electrothermal Actuators. (Under the Direction of Dr. Jingyan Dong).

Soft actuators are widely studied due to their high flexibility and adaptability. This study reports a new cost-effective approach to fabricate soft electrothermal actuators. Polyimide (PI) and polydimethylsiloxane (PDMS) were selected as the two structural layer materials due to their large difference in coefficient of thermal expansion (CTE). Embedded in between these two layers, a metallic microfilament heater made of a low-melting-point alloy (Bi58/Sn42) was directly printed using the electrohydrodynamic (EHD) printing process. The pattern of the microfilament heater and the thickness of the structural layers were carefully designed towards improved actuation capability. The fabricated electrothermal actuator was characterized on its heating and bending performance. It can achieve a maximum bending curvature of 1 cm^{-1} under an extremely low voltage about 3 V.

Closed-loop control of soft actuators is critical for high precision applications, due to the nonlinear relationship between actuation voltage and output bending motion. Meanwhile, operation of soft electrothermal actuators usually has a long transient time and is susceptible to external environment variations. In this dissertation, a resistive self-sensing approach was developed to enable the closed-loop control of the actuator without external sensors. To accommodate the different response characteristics of the actuator in the heating and cooling stages, a switching proportional–integral–derivative (PID) control algorithm was designed. Specifically, two sets of control parameters were tuned and used for the heating and cooling stages, respectively. The performance of the designed control algorithm was evaluated for setpoint tracking, step response, wave signals tracking, and disturbance rejection. Compared with the open-loop

operation, the closed-loop controlled actuator demonstrated much more rapid and accurate response, and excellent tracking and disturbance rejection capabilities.

Finite element analysis (FEA) is the simulation of physical phenomena using a numerical mathematic technique. Our electrothermal actuator is an electric-thermal-mechanical coupled multiphysical system. FEA is a powerful tool to simulate and analyze the actuation process and the relationship between supply voltage, temperature distribution, and bending deformation. Due to its high nonlinearity, simulation of elastic materials is much difficult than the conventional rigid structures. Nonlinear adaptive region and semi-implicit solving techniques were used to overcome the convergence difficulties. FEA software ANSYS was then successfully utilized for the thermal and deformation analysis of the electrothermal actuator.

In recent years, there has been an increasing interest in the research of soft actuators that exhibit complex programmable deformations. Complex programmable deformations of soft electrothermal actuators are difficult due to the limitations of conventional fabrication methods. The direct patterning capabilities of EHD printing allows free-form design of the heater. By changing the design of the heater pattern on the actuator, different heat distributions can be achieved and utilized to realize complex programmable deformations, including uniform bending, customized bending, folding, and twisting. FEA was used to validate the thermal distribution and deformation for different actuator designs.

Finally, the soft electrothermal actuators were demonstrated for various biomimetic applications, including a soft lifter, soft grippers, a two-degree-of-freedom soft robot arm, and soft walkers.

Fabrication, Control, and Applications of Programmable Soft Electrothermal Actuators

by
Yang Cao

A dissertation submitted to the Graduate Faculty of
North Carolina State University
in partial fulfillment of the
requirements for the degree of
Doctor of Philosophy

Industrial Engineering

Raleigh, North Carolina
2020

APPROVED BY:

Dr. Jingyan Dong Committee Chair	Dr. Yuan-Shin Lee
Dr. Paul Cohen	Dr. Yong Zhu

DEDICATION

To my parents, Xincheng Cao and Meifang Gao

To my wife, Jingyi Zhang

BIOGRAPHY

Yang Cao was born in 1991, in Xiaogan, Hubei, China. He received the B.S. Degree in Mechanical Design and Manufacturing & Automation from Wuhan University of Technology, Wuhan, China, in 2013. He received the M.S. degree in Mechatronic Engineering from Chongqing University, Chongqing, China, in 2016. He joined the Ph.D. program in the Edward P. Fitts Department of Industrial and Systems Engineering at North Carolina State University in 2016. He worked in the Micro/Nano Manufacturing Lab under the guidance of Dr. Jingyan Dong. His research focuses on micro-scale fabrication, EHD printing, and flexible sensors and actuators.

ACKNOWLEDGEMENTS

I would like to express my deepest gratitude to my advisor Dr. Jingyan Dong for his continuous support, guidance, and encouragement in the past four years. This work cannot be accomplished without his mentorship. His personalities and research ethics keep encouraging me and set a role model for my future faculty career. I am also truly grateful to my committee, Dr. Yuan-Shin Lee, Dr. Paul Cohen, Dr. Yong Zhu, and Dr. Nam Dinh, for their valuable feedback and comments.

I would like to thank my former and current colleagues, Dr. Yiwei Han, Ping Ren, Hengfeng Gu, and Yi Wang. Thank you all for your support and help. You have made my journey at NC State much more wonderful and memorable.

TABLE OF CONTENTS

LIST OF TABLES

LIST OF FIGURES

CHAPTER 1: INTRODUCTION

1.1 Background

Unlike traditional mechanical devices, soft actuators and robotics are built with highly resilient materials (usually, polymer or polymeric composites), similar to those found in living organisms. As a result, soft actuators can easily deform and adapt to changing environments. Compared with their conventional counterparts, soft actuators are lightweight, can easily achieve multi-degree-of-freedom motion, and have high load-to-weight ratio. These characteristics give them great potential to be used in many applications, including soft robotics [1], drug delivery [2], artificial muscles [3, 4], and so on.

Soft actuators deform and change their shapes when exposed to external stimuli, such as electricity, magnetic field, chemical, heat, light, pressure, etc. Depending on the type of stimuli, soft actuators can be classified into electrically responsive actuators, magnetically responsive actuators, chemically responsive actuators, thermally responsive actuators, photo responsive actuators, and pressure driven actuators [5]. The energy of soft thermal actuators comes from different sources, such as electricity or light, corresponding to electrothermal actuators and photothermal actuators, respectively. Electrothermal actuators usually have a conductive layer as the heater to provide necessary Joule heat for actuation, while photothermal actuators are based on light-thermal conversion using the light absorbing materials such as graphene or graphene oxide. Electrothermal actuators are usually fabricated in a bimorph structure with two layers that have significantly different coefficient of thermal expansion (CTE). When exposed to temperature change from thermal energy, the large thermal expansion mismatch between the two layers makes the bimorph structure to bend. A conductive path of the electrothermal actuator provides Joule heat as the stimulus for actuation when actuated by a given voltage. The resulting temperature change drives the actuator to bend.

There are numerous ways to fabricate electrothermal actuators, while the major difference lies in the conductive layer: materials and fabrication methods. Three factors need to be considered: a) The conductive layer should not add too much stiffness to the actuator, which will adversely affect its actuation and flexibility; b) The conductive layer needs to have an appropriate electrical resistivity so that the actuation voltage and current will not be over high; and c) A feasible method to deposit conductive materials on the polymer structural films. These three requirements are extremely hard to be fulfilled by a conventional material. For this reason, most existing research used expensive nano materials like carbon nanotubes [6-8], silver nanowires [9-11], graphene [12-15], etc. in the fabrication of soft electrothermal actuators. The main reason is that those materials can be easily used as a solution to be coated as a thin conductive film.

In this study, we developed an innovate method to fabricate soft electrothermal actuators – electrohydrodynamic (EHD) printing. Assisted by its high-resolution, wide range of printable materials, as well as direct and free-form patterning capabilities, it is easy to overcome the above fabrication difficulties. We used a very cheap low melting point alloy Bi58/Sn42 (58% Bismuth, 42% Tin) as the printing material. By printing a fine microscale filament, the heater's bending stiffness can be reduced to an acceptable level. Bi58/Sn42 has a relatively high electrical resistivity of 34.5 μΩ-cm. The resulting heater filament has an electrical resistance about 5-10 Ω, which can be actuated using an appropriate voltage and current.

Another advantage of this directly printed metallic filament heater is that it can be utilized to sense the actuator's deformation, as the deformation is due to temperature change which can be detected by the heater's electric resistance. Closed-loop operation of soft actuators is critical for high-precision applications. By measuring the real-time electric resistance of the embedded heater filament, we are able to detect the actuator's bending curvature. Based on this self-sensing mechanism and appropriate control techniques, the closed-loop operation of the soft electrothermal actuator can be achieved.

Meanwhile, the direct patterning capabilities of EHD printing allow free-form design of the embedded heater. By changing the design of the heater pattern, different heat distributions can be created and utilized to realize complex programmable deformations, including uniform bending, customized bending, folding, and twisting. This is not easy for other soft electrothermal actuators reported due to the limitations of conventional fabrication methods.

1.2 Research Objectives

The overall objective of this dissertation is to develop a new method to fabricate soft electrothermal actuators, to accurately control their bending curvature, to realize complex programmable deformations, and apply them for soft robotic applications. The following part discusses the detailed objectives as well as the approach to solve them.

1) Explore the printing technology of low melting point alloys

The EHD printing technology can be used for a wide range of materials, such as low melting point alloys, solution of silver nanowires, carbon nanotubes, and graphene, etc. We selected a low melting point alloy Bi58/Sn42 for its low-cost, appropriate melting point, and relatively high electrical resistivity among most solders. Even though the printing technology and parameters for various materials have been studied, Bi58/Sn42 has never been reported for EHD printing uses. It is critical to experimentally optimize the printing parameters, including printing temperature, printing voltage, pneumatic pressure, printing speed and nozzle-substrate standoff distance.

2) Fabrication and characterization of the electrothermal actuator

PI and PDMS were selected as the structural materials for the soft electrothermal actuator, due to their large difference in CTE. A fabrication process needs to be explored to make the sandwich structured PI/Bi58/PDMS electrothermal actuator. The heater pattern and structural film thickness need to be carefully designed for optimized bending actuation. Due to the addition of an embedded heater layer, our fabricated actuator is largely different from traditional bimorph actuators. A theoretical model needs to be built to predict the actuator's bending deformation. Also, the heating and bending performance of the electrothermal actuator need to be characterized experimentally.

3) Self-sensing control of the electrothermal actuator

Closed-loop control of soft actuators is a critical but rarely studied area. One inherent drawback of electrothermal actuators is the nonlinear and complex relationship between the actuation voltage and the resulting bending curvature. Moreover, due to the low stiffness structure and long thermal time constant, the open-loop operation of soft electrothermal actuators usually has a long transient time and is susceptible to external environment variations. Therefore, the closed-loop control is critical to improve the performance of soft actuators for high precision and dedicated applications. Compared with closed-loop control with external sensors, self-sensing control integrates the actuation and sensing functions together, which largely simplifies the complexity of the control system. We need to build the dynamic model of the electrothermal actuator, find a feasible self-sensing mechanism, and develop a control system and algorithm for the feedback control of the electrothermal actuator.

4) Complex programmable deformations of the electrothermal actuator

Most reported electrothermal actuators can only generate a uniform curvature bending. Assisted by the direct and free-form patterning capabilities of EHD printing, we are able to print different heater pattern designs. An evenly distributed heater filament generates a homogeneous heating area that leads to uniform bending. A heater pattern with changing line spacing can create a temperature gradient, which leads to customized bending. A heater pattern distributed only in the middle section of the actuator results in localized heating and hence folding deformation. A skewed heater pattern can also be printed, which creates a parallelogram high temperature zone that leads to coupled bending and twisting deformation.

5) FEA simulation of the electrothermal actuator

Our fabricated electrothermal actuator is a complex electric-thermal-mechanical coupled multiphysical system. FEA simulation is useful for the thermal analysis and deformation analysis of the electrothermal actuator. However, several difficulties need to be overcome. Firstly, the actuator has a microscale heater filament, whose dimensions are much smaller than the actuator's overall size, which brings difficulties to the meshing process. Secondly, our electrothermal actuator is generally made of elastic materials, can generate large deformation when heated. Due to its high nonlinearity, simulation of elastic materials is much more difficult than the conventional rigid structures. In this dissertation, we will use ANSYS for the electric-thermal-mechanical multiphysics simulation to obtain the temperature distribution and deformation profile of the soft electrothermal actuator.

6) Apply the electrothermal actuator for biomimetic applications

Due to their high flexibility and adaptability, electrothermal actuators have great potential to be used for soft robotic applications. In this dissertation, we applied the fabricated electrothermal actuators for a soft lifter, soft grippers, a two-degree-of-freedom soft robot arm, and soft walkers. They can be used for applications that interact with fragile or delicate objects that cannot be handled by the conventional rigid devices.

1.3 Dissertation Outline

This dissertation is composed of nine chapters. Chapter 2 is the literature review which covers the major types of soft actuators. Chapter 3 introduces the EHD printing system, and presents the design, fabrication, and characterization of the electrothermal actuator. Chapter 4 discusses the self-sensing control of the electrothermal actuator. Chapter 5 presents the study on the twisting deformation of the electrothermal actuator. Chapter 6 explains the process for the multiphysics simulation of the electrothermal actuator. Chapter 7 focuses on the programmable deformations of the electrothermal actuator. Chapter 8 demonstrates the electrothermal actuators for various biomimetic applications. Chapter 9 summarizes the research work and contributions, and discusses the potential future research directions.

1.4 Chapter Summary

This chapter discusses the research motivations of developing a new approach to fabricate soft electrothermal actuators. It is cost-effective and capable of achieving self-sensing control and complex programmable deformations. The main research objectives are detailed in the following section. The outline of this dissertation is presented at last.

CHAPTER 2: OVERVIEW OF SOFT ACTUATORS

2.1 Electrically Responsive Actuators

Electrically responsive actuators are actuators that can convert electrical energy to mechanical energy. Electrically responsive soft actuators are generally based on electroactive polymers (EAPs), which exhibit a change in size or shape when stimulated by an electric field. EAPs can be divided into two principal classes: dielectric and ionic.

Actuation of dielectric EAPs is caused by the electrostatic force between the two electrodes. Dielectric EAPs are fundamentally a polymer capacitor that changes its capacitance by compressing in thickness and expanding in area when a voltage is applied. This type of EAP typically requires a large actuation voltage to produce high electric fields, but has very low electrical power consumption, and requires no power to keep the actuator at a given position. Examples are electrostrictive polymers and dielectric elastomers.

One of the most widely studied electrostrictive polymers is polyvinylidene fluoride (PVDF), as well as its copolymers and terpolymers. In 1969, strong piezoelectricity was observed in PVDF, with its piezoelectric coefficient of poled thin films being 10 times larger than that

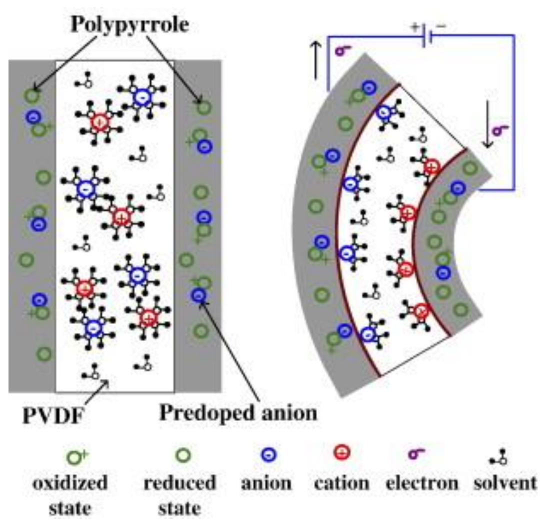

Figure 2.1 Illustration of the actuation mechanism of a PVDF based trilayer actuator [17].

observed in any other polymers [16]. Piezoelectricity is a property exhibited by some materials that accumulates electrical charge resulting from an applied mechanical force. It is also reversible that a mechanical strain can be generated in response to an applied electric field, which is the mechanism that PVDF is used for electrically responsive actuators. Figure 2.1 shows the actuation mechanism of a PVDF-based trilayer actuator. Both sides of the actuator are coated with polypyrrole (PPy) as electrodes. When a voltage is applied across the actuator, the PPy on the anode side is oxidized while that on the cathode side is reduced. The oxidized layer absorbs anions and expands, while the reduced layer gives up anions and contracts. The differential expansion thus leads to bending of the actuator [17]. Perez et al. [18] fabricated a PVDF based bimorph actuator for high-speed laser beam manipulation. A compact mirror was placed at the tip of the PVDF bimorph actuator allowing scanning of the beam in two directions. Experimental results indicated that the PVDF actuator responded conveniently to manipulate the laser beam at kHz frequency. Wu et al. [19] reported a pre-curved PVDF based soft inchworm actuator that have large curvature changes under a relatively low driving voltage (200 V), and is able to crawl with a moving speed up to 1.9 mm/s on a rough surface. Copolymers and terpolymers of PVDF are also attractive materials for electroactive actuators [20]. In article [21], a comparison between PVDF and poly(vinylidenefluoride-co-trifluoroethylene) P(VDF-TrFE) films in terms of deposition conditions and their effect on the piezoelectric response is presented. Engel et al. [22] fabricated a self-sensing electroactive polymer bimorph actuator. The tip deflection of the actuator is sensed by the voltage measured across the bimorph's integrated layer of PVDF. The actuation layer is based on a PVDF terpolymer polyvinylidene fluoride-trifluoroethylene chlorotrifluoroethylene (P(VDF-TrFE-CTFE)). The actuator reached a magnitude of 350 μm under an electric field of about 55 MV/m. Shklovsky et al. [23] fabricated a near fully polymeric electroactive actuator based on P(VDF-TrFE-CFE). The active layer is a thin P(VDF-TrFE-CFE) layer squeezed between polyaniline (PANI) electrodes, and the passive layer is a polyimide substrate.

Compared with the small deformations of electrostrictive polymers, dielectric elastomers can produce much larger strains. Figure 2.2 shows the driving mechanism of the dielectric elastomer actuator. Applying a voltage difference across the stretchable electrodes causes a squeeze as the stretchable electrodes pull against each other. This squeeze contracts the actuator in the thickness direction and expands it in the plane direction due to the incompressibility of the rubber [24]. Because all dielectrics experience this electrostatic stress, a great many polymer materials can be utilized as dielectric elastomer actuators. The most successful materials have a relatively low modulus of elasticity and can sustain high electric fields. These materials include commercially available formulations of silicone rubber polydimethylsiloxane (PDMS) and acrylic elastomers [25]. Jun et al. [26] developed an electroactive haptic interface utilizing soft elastomer actuators. The electroactive layer was fabricated by blending PDMS and Ecoflex prepolymer. By properly adjusting the applied electrical stimuli, it was possible to control the heights of the void regions of the electroactive layer to different levels, thus producing various active surface textures. Nicolau-Kuklińska et al. [27] fabricated a dielectric elastomer actuator made of PDMS, multi-

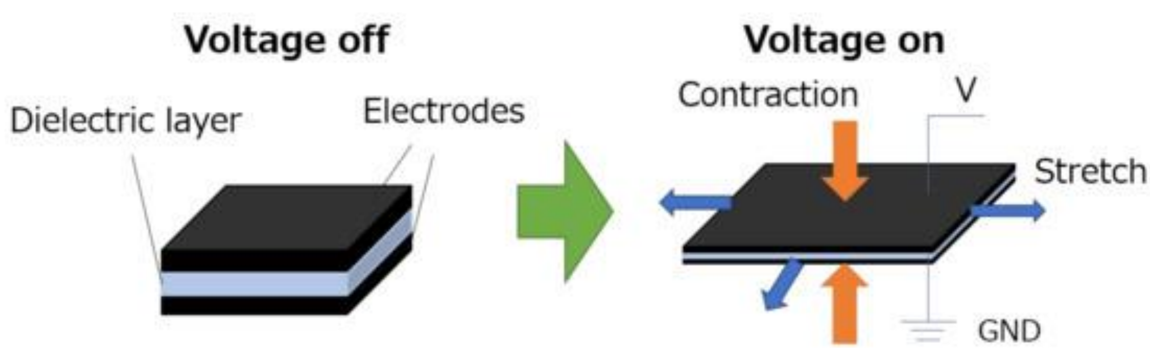

Figure 2.2 Driving principle of the dielectric elastomer actuator [24].

walled carbon nanotubes, and carbon grease. The largest deformation of 47% was obtained for electrodes made of 2 wt% of multi-walled carbon nanotubes and 20 wt% of carbon grease. Lau et al. [28] fabricated a multilayer acrylic dielectric elastomer actuator coated with silicone gel. The gel coating helps suppress the electro-thermally induced puncturing of DEA membrane at the hot spot and enables the DEAs to produce 30% more isometric stress change as compared to those none-coated. Thermoplastic polyurethane (TPU) has also been used as material for dielectric elastomer actuators. Gonzalez et al. [29] fabricated a dielectric electroactive polymer actuator using 3D printing technology. TPU was fused deposition modeling (FDM) printed as EAP actuators. Under a supplied voltage about 5 kV, the actuators exhibited around 5% area expansion.

(a) (b)

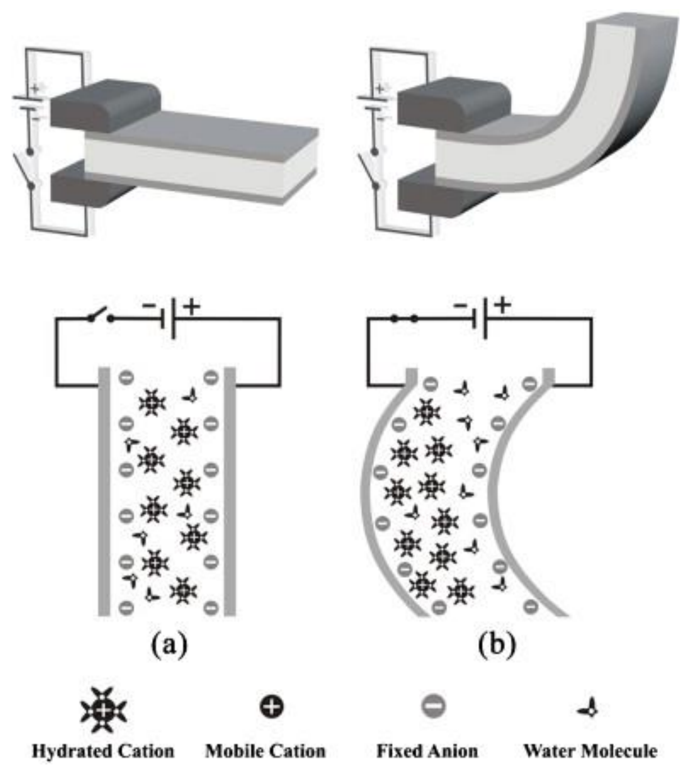

Figure 2.3 Working principle of an IPMC actuator: (a) before applying an electric field; (b) after applying an electric field [32].

In ionic EAPs, actuation is caused by the displacement of ions inside the polymer. Only a few volts are needed for actuation, but the ionic flow implies a higher electrical power needed for actuation, and energy is needed to keep the actuator at a given position. Examples of ionic EAPs are ionic polymer-metal composites (IPMCs), conductive polymers and carbon nanotubes [30].

IMPC is garnering growing interest for ionic artificial muscle, soft actuators and sensors due to its inherent properties of low weight, flexibility, softness, and particularly, efficient transformation of electrical energy into mechanical energy, with large bending strain response under a low activation voltage [31]. Figure 2.3 shows an IPMC strip actuator, which is a combination of a thin membrane coated by two metallic plates on both sides. Under the stimulus of a relatively low electric field (2–3 V) through the thickness of an IPMC, its internal hydrated cations will flow toward the cathode. This transportation leads to inflation in the cathode side and causes a bending response of the IPMC as shown in Figure 2.3 (b) [32]. Nakshatharan et al. [33] developed a self-sensing ionic electroactive polymer actuator based on IPMC. As IPMC also exhibits sensorial behavior by generating a small electrical potential on the application of mechanical force, the actuator integrated sensing and actuation, and shown excellent control and tracking accuracy.

Nafion is a brand name for a sulfonated tetrafluoroethylene based fluoropolymer-copolymer discovered in the late 1960s. Nafion's unique ionic properties are a result of incorporating perfluorovinyl ether groups terminated with sulfonate groups onto a tetrafluoroethylene (PTFE) backbone [34,35]. As an ionic conductive polymer, Nafion has received considerable attention as EAP actuators. Ru et al. [36] developed an ionic EAP actuator based on Nafion/$EMImBF_4$ (50 wt% and 50 wt% composite). Under a 4 V voltage, the actuator reached a 1.26% strain and 5.27 MPa stress, and also demonstrated excellent electromechanical controllability and durability. Palmre et al. [37] developed an EAP actuator that has a Nafion electroactive layer, and carbon aerogel electrodes. At 2 V voltage, the carbon aerogel activated and non-activated actuators displayed a maximum strains of 1.2% and 1.3%, respectively.

CNTs and other nanoparticles or nanofibers represent emerging materials that used as a filler in polymeric matrix to form an electroactive polymer. Melvin et al. [38, 39] found that by including CNTs as the filler for polyurethane (PU), the electrical properties of the films improved significantly. The PU/CNTs film bends toward the cathode when an electric field was applied, and it reverted to its original position when the electric field was removed. Mazzoldi et al. [40] fabricated an electroactive carbon nanotube actuator by mixing carbon nanotubes with polyvinyl alcohol (PVA) and polyallylamine (PAA). The fabricated actuator reached an electro-mechanical conversion efficiency of about 0.2 μm/mV. Yan et al. [41] fabricated an electroactive ionic soft actuator based on electroactive ionic gel/metal nanocomposites that produced by implanting supersonically accelerated neutral gold nanoparticles into a novel chemically cross-linked ion conductive soft polymer. Ebadi et al. [42] fabricated an electroactive actuator based on conductive polymer. A nanofibrous conductive polymer layer was fabricated by polyurethane/polypyrrole (PU/PPy), through electrospinning and in-situ chemical polymerization, respectively. The fabricated actuator was capable of undergoing 141 ° reversible angular displacement during a potential cycle.

2.2 Magnetically Responsive Actuators

Magnetically responsive soft actuators usually involve the incorporation of magnetic particles and/or ferrofluid into polymer matrices. Such actuators have been realized across a wide range of soft polymers, such as PDMS [43, 44], Ecoflex [45], rubbers [46] and polyurethanes [47]. When these actuators are subjected to an external magnetic field, the embedded magnetic particles

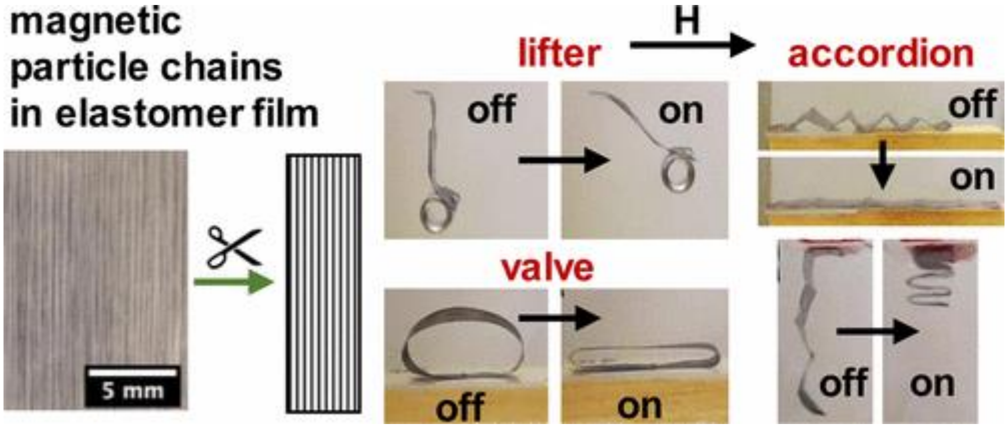

Figure 2.4 An elastomer film containing magnetic microparticles as well as its applications as a lifter, accordion, valve, and pump [50].

try to align with the fields, and generate forces and deflections. The generated forces and deflections are affected by the diameter, thickness, and concentration of magnetic fillers [48]. As magnetic fields can penetrate through a wide range of materials, these magnetic actuators are ideal candidates for working in enclosed spaces like drug delivery and microsurgery within the body [49]. Another advantage of magnetically responsive actuators is that their response is relatively fast compared to other kinds of soft actuators, with demonstrations up to 100 Hz presented [43]. The shortcomings of magnetically responsive actuators are that they need large external magnetic coils and have high power consumption.

Elastomer films containing chained magnetic microparticles were developed by Schmauch et al. [50]. By changing the structure and orientation of the polymer films, and strength and direction of the applied magnetic field, they were able to demonstrate applications as different soft actuators, including a cantilever lifter, an accordion structure, a valve, and a peristaltic pump as shown in Figure 2.4. Fuhrer et al. [51] dispersed carbon-coated cobalt nanoparticles (C/Co) into a polymer matrix poly(2-hydroxyethyl methacrylate), resulting in an ultra-flexible, yet strong magnetic actuator. Yamanishi et al. [52] developed a magnetically driven soft micro actuator by suspending magnetite (Fe_3O_4) particles in PDMS. The actuators demonstrated great potentials as microtools for bio-applications, due to their non-intrusive and non-contamination natures. Taniguchi et al. [53] developed a magnetic responsive soft actuator by mixing magnetic fluid with silicone rubber. The rubber actuator can be driven by several electromagnetic coils to move as a flexible walking robot. Ji et al. [54] developed a magnetic resin by incorporating Fe_3O_4 nanoparticles into flexible 3D printing resins, and used it to fabricate arbitrary-shape soft magnetic actuators by digital light processing (DLP). DLP 3D printing enables the free assembly manufacturing of actuators with complicated architectures to achieve bending, deformation, cargo transportation, and so on.

2.3 Chemically Responsive Actuators

The transformation of chemical energy into mechanical energy is called chemomechanical motion. Chemically responsive actuators are a rather broad category. The stimulus, in the form of liquid or vapor, typically involve some chemical reactions, swelling or shrinking due to pH level change in the surrounding environment, or simply water or moisture induced volumetric change.

Chemically responsive shape memory polymers (SMPs) have gained considerable attention in the past decade, especially in the field of medical applications. Similar to thermal-induced SMPs, chemical-induced SMPs have an original shape, and can be bent to a temporal shape. After immersing in a chemical solution, they can recover their original shapes. Chemical-induced SMPs usually have a long response time, varying from hours to days, and are nonreversible if only rely on chemical reactions. For instance, Dong et al. [55] prepared a redox-induced SMP by crosslinking β-cyclodextrin modified chitosan (β-CD-CS) and ferrocene modified branched ethylene imine polymer (Fc-PEI). The resulting β-CD-CS/Fc-PEI contains two crosslinks: reversible redox-sensitive β-CD-Fc inclusion complexes serving as reversible phases, and covalent crosslinks serving as fixing phases. This material can be processed into temporary shapes as needed in the reduced state and recovers its initial shape after oxidation. Yasin et al. [56] prepared a ferric-phosphate induced shape memory hydrogel by the one-step copolymerization of isopropenyl phosphonic acid (IPPA) and acrylamide (AM) in the presence of a crosslinker polyethylene glycol diacrylate (PEGDA). The shape memory hydrogel can be processed into various shapes as needed and recovers to its original form in ‘multiconditions’ such as a reducing agent erythorbic acid solution or a competitive complexing agent ethylenediamine tetraacetic acid disodium salt (EDTA·2Na) solution.

Vapor or solvent absorption induced volumetric change can also serve as an actuation mechanism for chemically responsive actuators, and often has a rapid response speed. Zhao et al. [57] fabricated a porous polymer actuator that bends in response to acetone vapor (as shown in

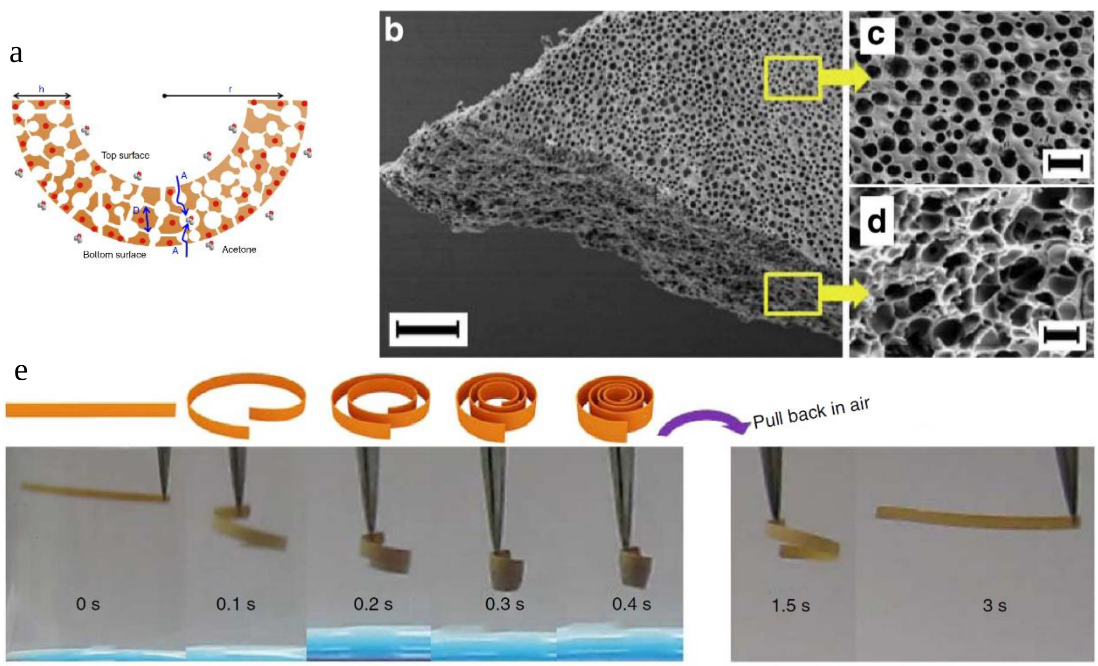

Figure 2.5 (a) Actuation mechanism of the porous membrane actuator. (b) SEM morphologies of the membrane actuator: general view (b, scale bar 30 μm); top surface (c, scale bar 3 μm); and cross-section (d, scale bar 1 μm). (e) Actuation of the membrane actuator when placed in acetone vapor [57].

Figure 2.5). When placed in acetone vapor (24 kPa, 20 °C), the flat membrane bent quickly into a closed loop in about 0.1 s. Due to the gradient in the degree of electrostatic complexation along the membrane cross-section, the bottom surface region is more solvated by acetone compared with the top. As such, the local solvent osmotic pressure increase leads to more swelling of the bottom layer, and the membrane bends towards the top side. Lee et al. [58] developed a microgel actuator that bends as one side with microfluidic channels swells in applying of acetone solvent, and jumps due to elastic instability, i.e. snap-buckling in the de-swelling process when the solvent in the microfluidic channels evaporates.

Besides, Belousov-Zhabotinsky reaction (BZ reaction) is also a notable mechanism for chemically responsive actuators [59-61]. Polymers and gels undertaking BZ reaction can produce a self-oscillating motion which can be utilized as soft actuators and robotics.

Researchers also found some polymers [62] and hydrogels [63] that exhibit swelling or shrinking depending on the level of pH in the surrounding fluid. Soft actuators based on this mechanism are considered especially useful for medical and biological applications, where other stimuli such as heating and light can be hard to apply, but physiological pH values exist naturally. According to study by Lee et al. [64] and Choe et al. [65], polyacrylonitrile (PAN) fiber exhibits diameter and volume change when subjected to a pH activated solution environment. PAN fiber contracts when exposed to a low pH environment and expands when exposed to a high pH environment. Park et al. [66] fabricated a pH-responsive hydrogel microsphere based on 4-hydroxybutylacrylate and acrylic acid. The microsphere shrinks when pH level is low (acidic solution) and swells when pH level is high (basic solution). Employing this hydrogel microsphere, a microfluidic valve has been successfully developed by researchers. Dong et al. [67] fabricated liquid microlenses whose focal length can be adjusted through the shape changing of the lens by the surrounding temperature or the pH value of the solution. The pH-sensitive hydrogels are based on acrylic acid and 2-(dimethylamino)ethyl methacrylate. By introducing pyridine rings into the backbone of polyurethane, Chen et al. [68] synthesized a pH-sensitive shape memory polymer which has been demonstrated to be used for drug delivery. Ye et al. [69] fabricated silk based self-rolling and unrolling biopolymer microstructures that respond to pH value. They can self-roll into distinct 3D structures including microscopic rings, tubules, and helical tubules.

As a biocompatible and safe stimulus, water or moisture can also be used to actuate chemically responsive actuators [70, 71]. Ma et al. [72] developed a polypyrrole (PPy) based water-responsive polymer film that can exchange water with the environment to induce film expansion and contraction, resulting in rapid and continuous locomotion. A generator was assembled by associating this actuator with a piezoelectric element, which can output alternating

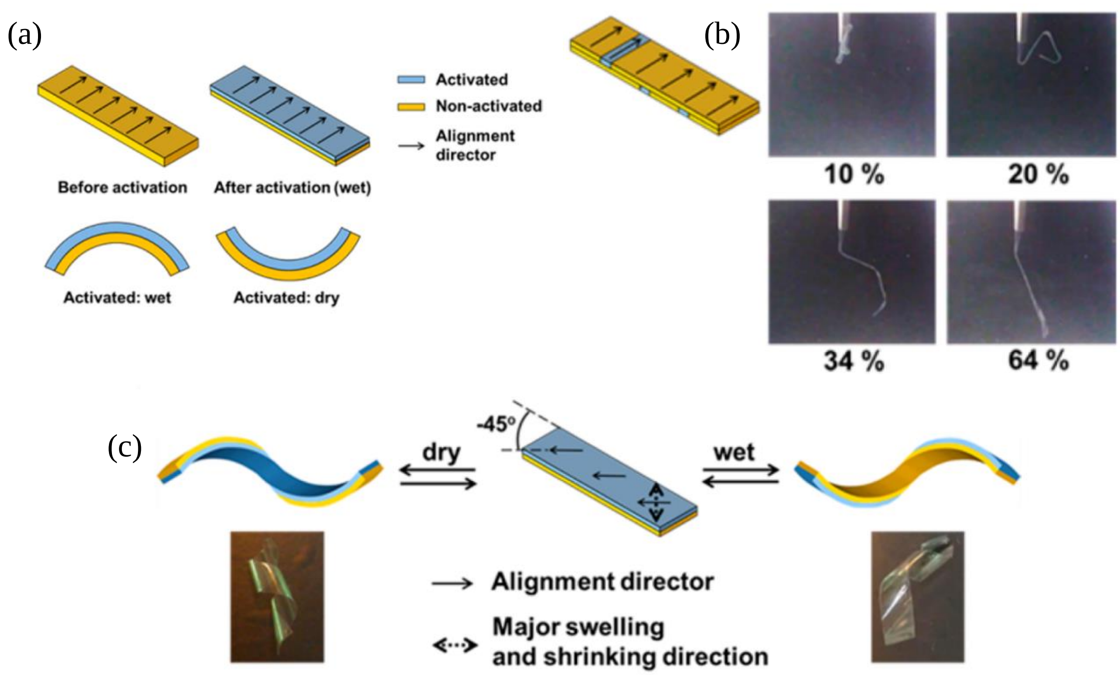

Figure 2.6 Actuation of a humidity-responsive liquid crystalline polymer actuator: (a) Schematic representation of the bending behavior. (b) Folding behavior. (c) Curling behavior [74].

electricity at about 0.3 Hz, with a peak voltage of about 1 V. Dai et al. [73] developed a humidity-responsive bilayer actuator that consists of an oriented polyamide-6 substrate and a liquid-crystalline polymer coating. The liquid-crystalline polymer consists of a supramolecular network having hydrogen-bonded entities that, after activation with an alkaline solution, exhibits deformation in response to a change in humidity. Haan et al. [74] fabricated a liquid crystalline polymer based humidity responsive actuator. By selective actuation and alignment direction of the activated layer, the actuator was able to realize bending, folding, and curling operations (as shown in Figure 2.6). Ma et al. [75] fabricated a polyelectrolyte multilayer soft walking device that can be activated by an alternating relative humidity between 11% and 40%. By coating a spore layer on polyimide tape, Chen et al. [76] were able to fabricate humidity driven artificial muscles, which are further assembled into evaporation-driven engines.

2.4 Thermally Responsive Actuators

Using heat as the stimulus, thermal actuators are usually fabricated with a bimorph structure with two layers that have significantly different coefficient of thermal expansion (CTE). When exposed to temperature change from thermal energy, the mismatch of thermal expansion between the two layers cause the actuator to bend. Although heat can be the direct stimulus for the motion of thermal actuators [77-82], it is not a convenient way. Instead, most thermally responsive actuators are based on electro-thermal or photo-thermal conversion, corresponding to electrothermal actuators and photothermal actuators, respectively. Electrothermal actuators either have an embedded heater or have one of the structural layers being conductive and actuating as the heater. With applied electrical energy, the generated Joule heat drives the actuator. Similarly, for photothermal actuators, an active layer containing light-absorbing nanomaterials absorbs and converts light into heat, and produces the deformation of the bimorph structure.

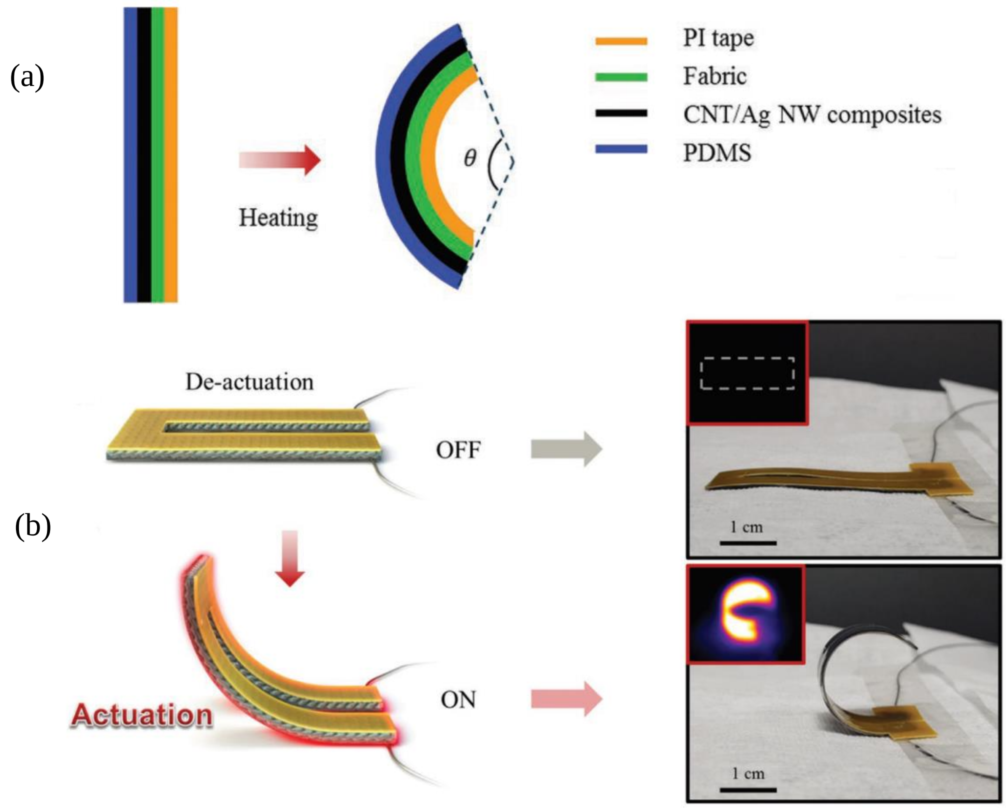

Figure 2.7 (a) The typical structure of an electrothermal actuator. (b) Schematics and images of the actuation process [10].

Soft bimorph electrothermal actuators usually involve non-conductive polymers as the structural layers for large deformation, and conductive paths as the resistive heater. Figure 2.7 shows the structure and actuation mechanism of a typical electrothermal actuator, in which PDMS and PI serve as the structural layers, and CNT/Ag nanowires coated fabric serves as the conductive heater layer [10]. To achieve soft conductive path, conductive materials/fillers (e.g. carbon nanotubes, metal nanowires, etc.) are often mixed with polymer matrices to form conductive composites with tailored conductivity and CTE. Carbon nanotubes (CNTs) and graphene are widely used materials for soft actuators. A multi-walled CNT/polymer composites electrothermal actuator was reported to achieve a curvature up to 0.29 cm^{-1} under a low voltage of 7 V [6]. By impregnating epoxy resin into the multi-walled CNT monolithic sheet, a composite with a negative CTE was produced [7]. After combining with an aluminum foil as the second layer, the fabricated electrothermal actuator with a length of 16 mm showed a 10 mm bending displacement under 6 V DC voltage. Polydimethylsiloxane (PDMS) as a silicon-based polymer has a relatively large CTE (linear CTE = 320×10^{-6} C^{-1} [83]). After embedding super-aligned CNT into PDMS matrix, it was observed that the CTE of the CNT-PDMS composite has been remarkably reduced [8], from which a CNT-PDMS composite/PDMS bimorph electrothermal actuator was fabricated and tested. Similarly, due to its extremely low resistivity and unique negative CTE [84], graphene has attracted great interests in applications for thermal or electrothermal actuators [12,13]. Taking the advantage of the negative CTE from graphene and large positive CTEs from polymers (e.g., PDMS, PVDF, polypropylene), thermal actuators with large actuation effect and quick actuation response were designed and fabricated [14, 15, 85], which have been applied in soft robotics applications. Besides carbon-based fillers, nanowires have also been used as conductive fillers to fabricate nanowire composites, which were used to fabricate the resistive heater in soft actuators [9, 86, 87] due to their high flexibility and conductivity. Other adopted materials include thermal expansion microspheres (TEMs) [88], polypyrrole (PPy) [89], and printing papers [90].

Besides electrothermal actuators, photothermal actuators are based on light-thermal conversion using the light absorbing materials, such as graphene or graphene oxide. Near infrared (nIR) radiation is widely used to fabricate nIR-responsive actuators, since nIR light can penetrate well into most biomaterials and is much safer than UV light. Graphene nanoplatelets (GNPs) based photothermal actuators were fabricated [91, 92] by mixing GNP with PDMS as the photo-active layer. When exposed to nIR light, the GNPs absorb and convert the radiation energy to heat, hence bend the designed bimorph structures. Graphene oxide (GO) [93] or reduced graphene oxide (RGO)

[94-96] were also used in nIR-responsive photothermal actuators for the applications in walking devices, remote assembly, and sunlight-driven smart curtains.

2.5 Photo Responsive Actuators

Photo responsive actuators, also known as photomechanical actuators, convert light energy directly into physical motion. Note that this is different from photothermal actuators, which use heat as the intermediary for heat-induced motions. Light-induced soft actuators are compelling because it can be remotely and accurately controlled, usually by varying the wavelength and intensity of the light. Actuation of photo responsive actuators is due to a chemical process called photoisomerization. Photoisomerization is the process by which one molecule, induced by

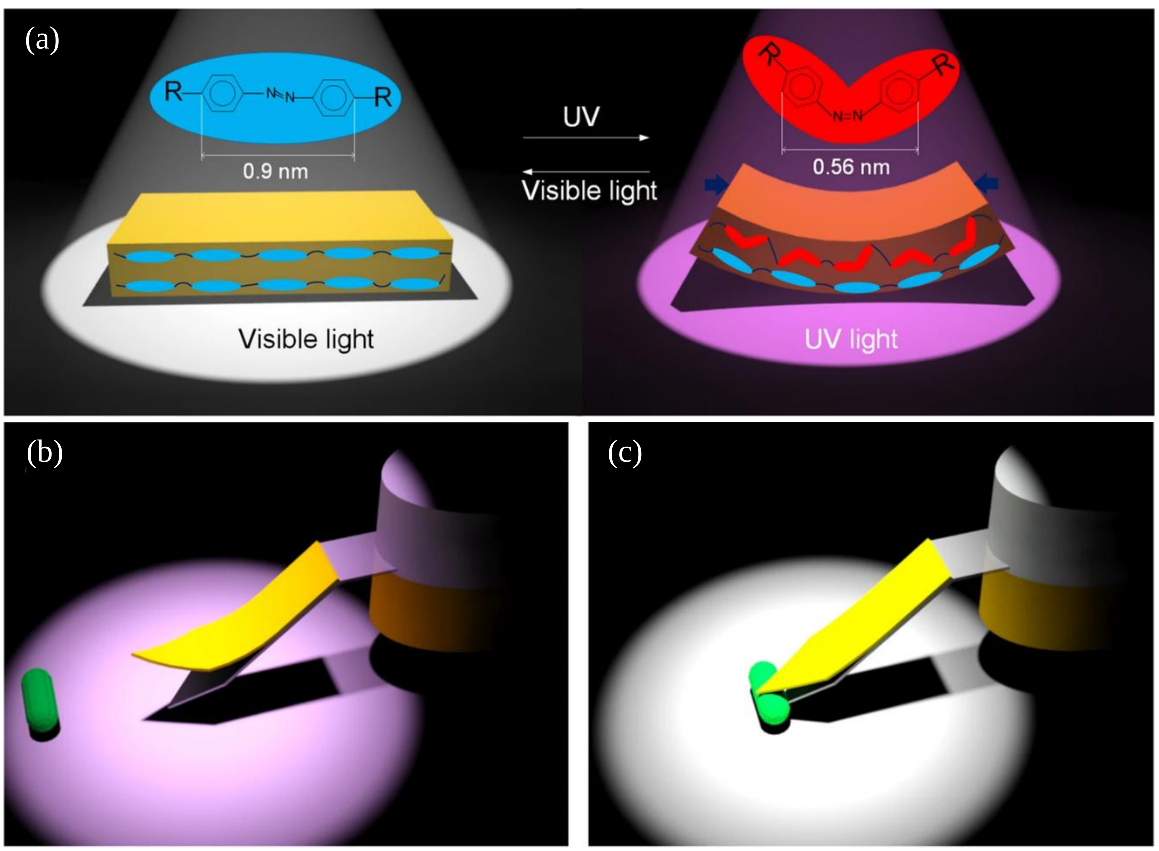

Figure 2.8 (a) Transformation of trans/cis isomeric azobenzene. (b, c) The schematic diagrams of gripper opened by UV light and closed by white light [97].

photoexcitation, is transformed into another molecule which has exactly the same atoms, but a different arrangement. Figure 2.8 shows the photoisomerization process of azobenzene when irradiated by ultraviolet (UV) light and visible light, as well as a gripper based on that [97]. To enable light-driven actuation, the soft actuators are filled with photosensitive fillers such as azobenzene [98], diarylethene [99], spiropyran [100], and liquid crystal polymer network [101].

Lv et al. [102] synthesized a reactive azobenzene liquid-crystalline block copolymer that showed reversible photodeformation regulated by alternating irradiation of UV and visible light. The bending direction of the actuator can even be precisely controlled by varying the polarization direction of the polarized light. Qin et al. [103] synthesized a cross-linked azobenzene/polymers supramolecular that exhibits reversible light-driven actuation. Inspired by the predation motion of pythons, Hu et al. [104] fabricated a bilayer photo-liquefiable azobenzene derivative/low density polyethylene photo actuator. By controlling the handedness and pitch of the helical deformation, it can grasp a variety of objects with different sizes and shapes. While typical crystalline elastomer actuators have very limited output force, Harris et al. [105] were able to fabricate an azobenzene based light responsive polymer networks that were heavily crosslinked with room temperature elastic moduli in the order of 1 GPa. Ryabchun et al. [106] fabricated a photo actuator based on stretched porous polyethylene and an azobenzene-containing liquid crystalline polymer network. Oosten et al. [107] utilized inkjet printing technology to fabricate azobenzene-containing liquid-crystal network photo actuators, which can be easily adapted for large-scale and low-cost production of miniaturized biomimetic devices. One of the shortcomings of photo responsive actuators is that UV light is utilized as the stimulus. Such high-energy light is not ideal for biomedical applications for safety considerations. Photo actuators driven by visible light have also been studied. For example, Jiang et al. [108] developed an azobenzene containing liquid-crystal soft actuator that can be actuated by red light based on triplet-triplet annihilation. Li et al. [109] synthesized a bridged azobenzene contained polyureas photo actuator that can bend above 110 ° in several seconds under irradiation of 405 nm blue light, and then recovers to its initial state under irradiation of 532 nm green light. Gelebart et al. [110] reported a rewritable and reprogrammable light responsive polymer actuator based on liquid crystalline. The contained azomerocyanine dye can be locally converted into the hydroxyazopyridinium form by acid treatment. These two dye forms absorb different wavelength, giving possibility to control the folding of the actuator by light of different wavelengths. Also, the acidic patterning is reversible and allows the erasing and rewriting of patterns in the polymer film. Kitagawa et al. [111] reported a photochromic diarylethene crystal that can twist by alternating irradiation with UV and visible light. The crystal twisting can take place in both left-handed and right-handed directions, depending upon the face irradiated with UV light.

Polymer gel is another base material for photo actuators [112]. For example, Ma et al. [113] developed a thermo-/photo- dual responsive actuator based on azobenzene containing ion gel. The photo-induced actuation can be realized reversibly be alternate irradiation with visible and UV light. Francis et al. [114] reported a spiropyran based hydrogel photo actuator. Due to the presence of the photochromic spiropyran molecule in the polymer structure, the phdrogels reversibly shrink and swell in aqueous environment when exposed to different light conditions. When placed onto a ratcheted surface, the actuation of the bipedal gel produces a walking motion.

2.6 Pressure Driven Soft Actuators

Most pressure driven soft actuators are pneumatic, though hydraulic soft actuators can be fabricated in a similar way. To generate effective actuation, pressure driven actuators have to spatially pattern their stiffness characteristics so that they can be stimulated by external pressure or forces to produce desired deformations. By varying the stiffness pattern, the bending profile of pneumatic actuators can be controlled. It has been shown that these pneumatic soft actuators can produce admirable force, even at small scales. Combined with their customized motions, pneumatic soft actuators are very suitable for wearable rehabilitative applications [115, 116] and soft grippers with high adaptability. However, pneumatic actuators need to be connected with a bulky compressor. Although battery powered microcompressors are available, they can only provide very low pressure. Pneumatic soft actuators are usually fabricated by casting elastic materials like silicone rubber [117] into molds. Some are fiber reinforced to constrain deformation in certain directions [118, 119]. Due to the difficulty in making microscale voids and channels, it is still challenging to fabricate soft pneumatic actuators on millimeter scale [120].

(a)

(b)

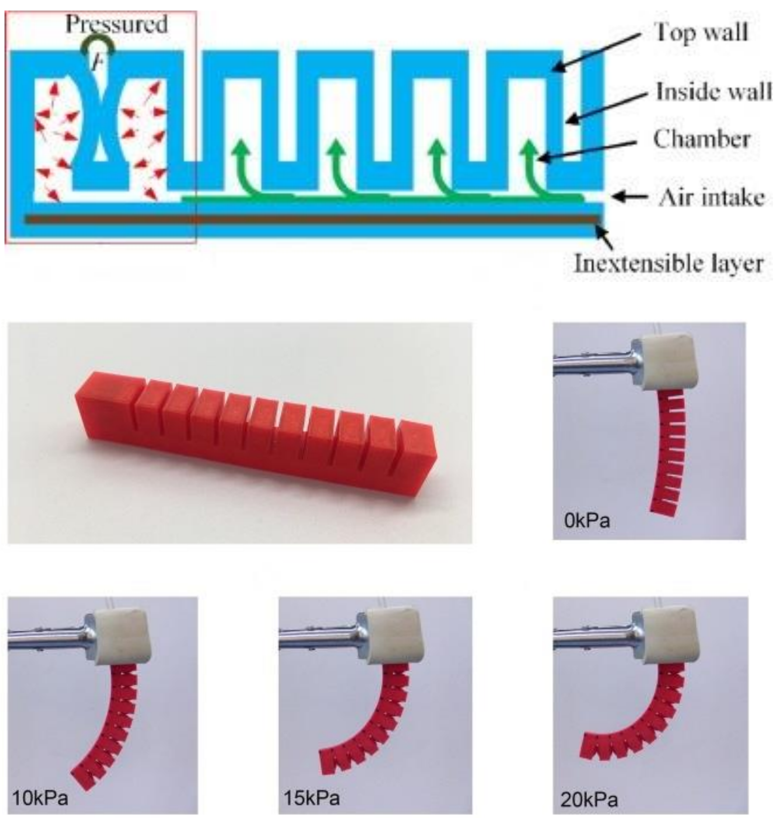

Figure 2.9 (a) Scheme of a pneu-net actuator [123]. (b) A pneu-net actuator and its deformations under different air pressure [127].

As a notable example of soft pneumatic actuators, pneu-net actuators [121, 122] consist of an extensible top layer and an inextensible but flexible bottom layer. The top layer is divided into multiple chambers, whose lateral walls are thinner than the rest part. When air is pumped in, the chamber would inflate, and the wall expands. The expanded chambers push each other and consequently the whole structure bends. Figure 2.9 shows the scheme and actuation of a pneu-net actuator. Tao et al. [123] developed a toothed pneu-net actuator, which was inspired by the scales of pangolins. For the fabrication process, the molds were 3D printed, and a soft silicone elastomer was used as the structure material. A three-finger soft gripper with autonomous controlling was fabricated and tested. Wang et al. [124] designed a soft pneumatic glove with five segmented pneu-net bending actuators. The segmented structure of the actuator was designed according to the anatomy of human fingers, which makes the actuator fit better than those of homogenous structure. Udupa et al. [125] developed an asymmetric bellow flexible pneumatic actuator for miniature robotic soft grippers. The actuator was divided into two symmetrical equal halves along the axis. Each half part involved machining process for the molds and silicone rubber paste for compression molding. Suzumori et al. [126] developed a bending pneumatic rubber actuator realizing manta swimming robot. The actuator has two internal chambers, in which the pressure is controlled independently. The rubber is reinforced with nylon cords in the circular direction to resist deformation in the radial direction. Therefore, when the pressure is increased in one chamber, the chamber stretches in the axial direction and the actuator bends in the direction opposite to the pressure-increased chamber.

In addition to the mold casted soft pneumatic actuators, 3D printed soft pneumatic actuators are also getting increasing attention. 3D printing can largely reduce the time and complexity of fabricating pneumatic soft actuators. Ge et al. [127] built up a digital light processing (DLP) 3D printer that can be employed to fabricate soft pneumatic actuators and micro soft pneumatic grippers with fast speed and high precision. Herianto et al. [128] studied the design optimization and fabrication of soft pneumatic actuators using fused deposition modeling (FDM) method.

2.7 Chapter Summary

This chapter covers a brief overview of different soft actuators, including electrically responsive actuators, magnetically responsive actuators, chemically responsive actuators, thermally responsive actuators, photo responsive actuators, and pressure driven soft actuators.

CHAPTER 3: FABRICATION OF THE ELECTROTHERMAL ACTUATOR

3.1 Introduction to EHD Printing

EHD printing is a maskless printing technology that uses an electric field to induce fluid flows from micro capillary nozzles. It can realize direct high-resolution patterning with more modest instrumentation requirements and simpler processing than lithography and etching based technologies. Due to its unique conical shape of the liquid meniscus at the nozzle end, EHD printing is capable of printing a droplet or a jet of fluid that is much smaller than the nozzle size. Resolution of EHD printing typically ranges from several to tens of micros, and even down to hundreds of nanos as reported [129, 130], while those of conventional thermal or piezoelectric inkjet systems are limited to around 30 μm [131]. Figure 3.1 shows a schematic of a typical EHD printing system. It consists of a three-axis motion stage, a pneumatic dispensing system, a high voltage supply, and a microscope camera. The stage, directed by CNC program, can move in XYZ

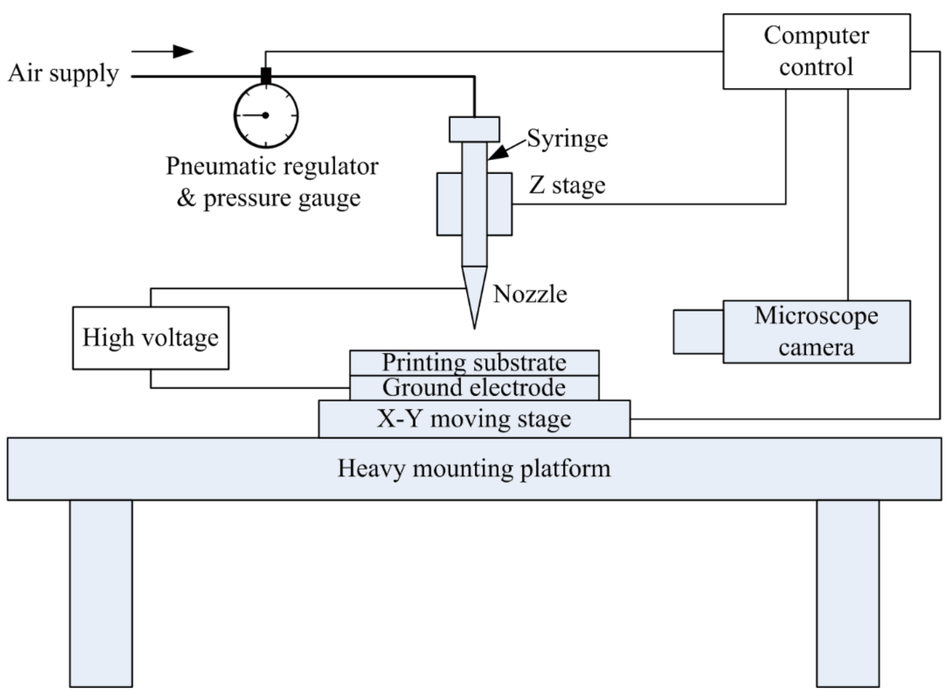

Figure 3.1 Schematic illustration of the EHD printing system.

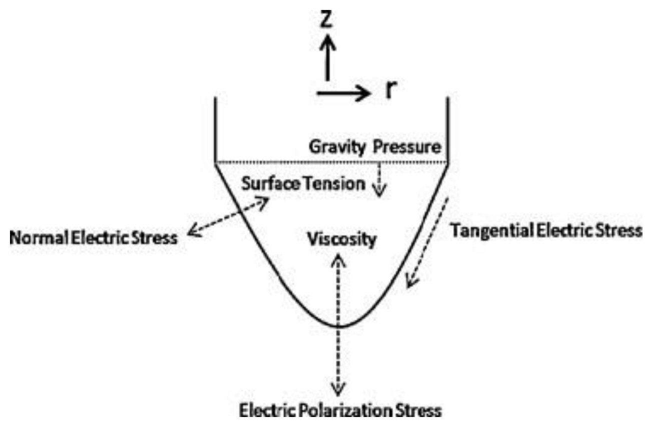

Figure 3.2 Stresses acting on the liquid meniscus of the EHD printing nozzle [132].

directions with high resolution. The printing nozzle (usually made of or coated with metal) and the ground electrode are connected to a high-voltage power supply. The pneumatic dispersing system is modulated by a precision pneumatic regulator to provide needed pressure to ensure a stable flow of the printing ink from the syringe to the nozzle tip. The microscope camera is used to monitor the printing process.

Figure 3.2 shows a schematic illustration of the liquid meniscus on the EHD printing nozzle tip. A conductive liquid (i.e. printing ink) is supplied to a nozzle where it is electrified by the high electric potential between the nozzle and the ground electrode. Electric charges accumulate at the surface of the liquid meniscus. The electrostatic stress causes the meniscus to deform into a conical shape called Tyler cone. When the electric field exceeds a critical limit, the stress from the surface charge repulsion at the cone apex exceeds the surface tension and a droplet of fluid is emitted towards the grounded substrate [132]. At sufficiently high fields, a stable jet mode can be achieved. In this situation, a continuous stream of liquid emerges from the nozzle [133]. The EHD printing system can be adapted or expanded to realize different patterning functions. For instance, by regulating a pulsed voltage to realize high speed drop-on-demand printing [134], integrating multiple nozzles to enable multi-material printing [135-137], and adopting the layer-by-layer stacking principle for 3D structures printing [131, 138].

A wide range of functional materials can be printed using the EHD printing technology, including low melting point metals [139, 140] (e.g., Field's metal, Wood's metal, Bi58/Sn42, and common Sn-Pb solders), nanomaterial solution (e.g., silver nanoparticles [141, 142], silver nanowires [87], silicon nanoparticles [133], carbon nanotubes [143], graphene [144], and graphene oxide [145, 146]), polymer-based ink [147, 148], and even biomaterial suspensions (e.g., deoxyribonucleic acid (DNA) [149] and living cells [150, 151]). Due to its high-resolution direct patterning capabilities, EHD printing is widely used in fabrication of thin film transistors [152] and memristors [153], flexible and stretchable electronics [87, 154], metal grid transparent electrodes [129, 155], light-emitting diodes [156, 157], and sensors and bioapplications [158, 159].

In this study, to reduce the stiffness from the microfilament heater and to minimize its influence on the actuation capability of the bimorph actuator, the diameter of the filament needs

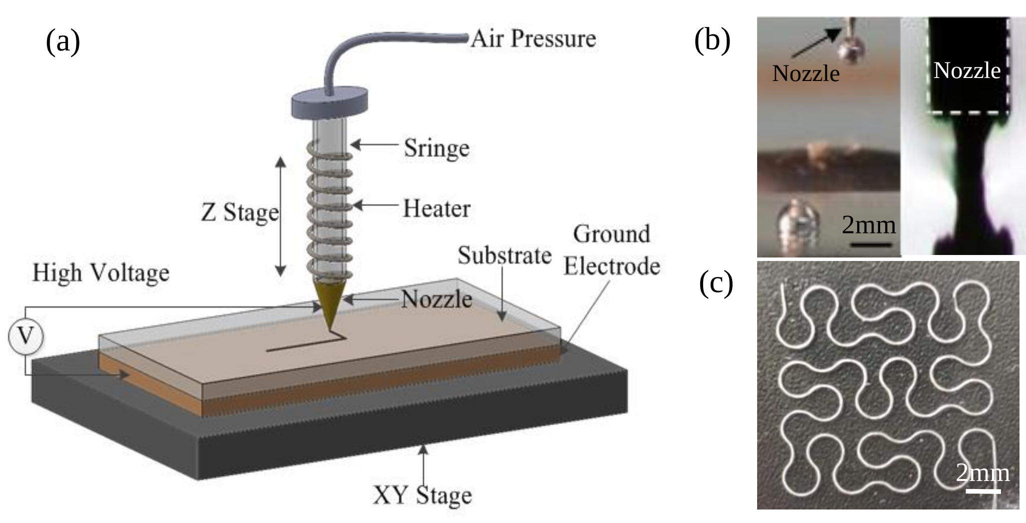

Figure 3.3 (a) Schematic of the EHD printing system. (b) Droplet printed by extrusion method (left) and cone shape (right) of EHD metal printing. (c) An EHD printed circuit pattern.

to be very small. It is very difficult for the traditional printing process to print molten metal ink due to its extremely large surface tension. An EHD printing process was developed to print the low melting point solder ink with high resolution into fine metal filaments as the resistive heater. The direct fabrication capability from EHD printing enables customized design and placement of the heater in the soft actuator. The EHD printing system used in this study is shown in Figure 3.3 (a). Compared with other EHD printing systems, the major difference is the addition of a PID-controlled heater, which is used to melt printing metals. The stage can move in XYZ directions, and has a motion accuracy about 100 nm. The PID-controlled heating system can heat the syringe up to 480 °C with a resolution of 0.5 °C. The EHD printing system can realize resolution up to 50 μm (here resolution is defined as the smallest achievable printed line width). Figure 3.3 (b) compares the printing behaviors between direct extrusion based printing and EHD printing. It clearly shows that the diameter of the ejected droplet in direct extrusion is much larger than the

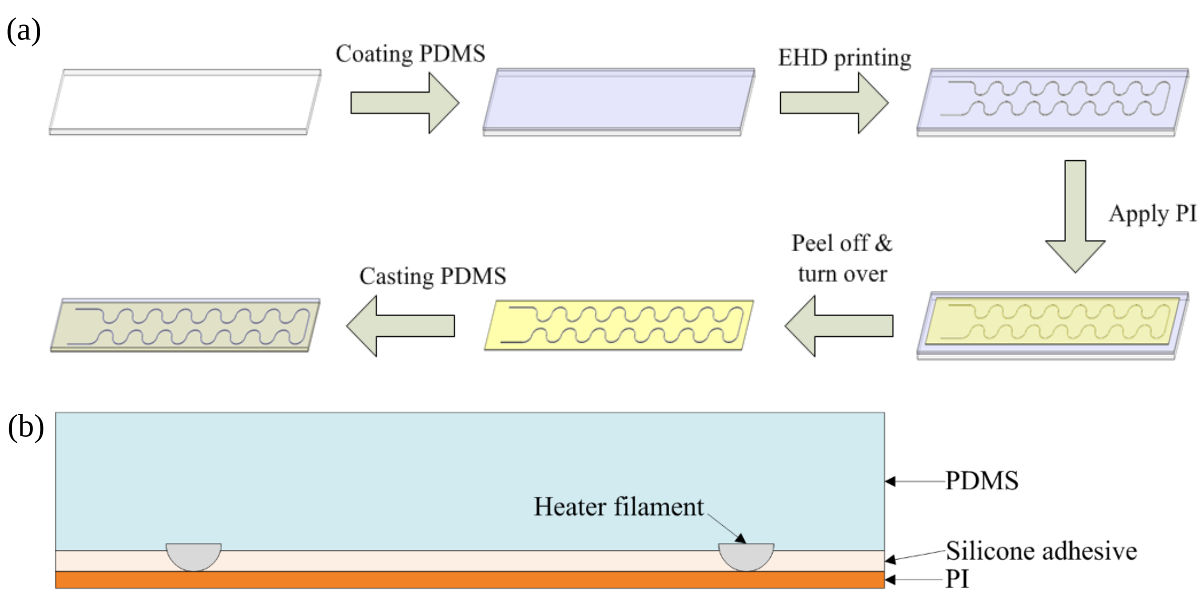

Figure 3.4 (a) Fabrication process of the soft PI/Bi58/PDMS electrothermal actuator. (b) Cross-section view of the electrothermal actuator.

nozzle size, because the large surface tension of the molten metal ink can balance a large gravity force and extrusion force. However, for EHD printing, the formed cone shape and ejected filament have a smaller size than the nozzle diameter, which can print high-resolution features as shown in Figure 3.3 (c). The printing parameters are summarized in Table 3.1, which were optimized by experiments. The nozzle we used has an inner diameter of 160 μm and an outer diameter of 250 μm and printing temperature was maintained at about 260 °C to achieve a good ink flowability. Only a small pneumatic pressure (about 0.1 to 0.2 psi, or 689 to 1379 Pa) was used to ensure smooth ink flow. A printing voltage of 1700 V was applied between the printing nozzle and the ground electrode.

Table 3.1 The printing parameters.

Parameter	Value
Nozzle size (inner diameter)	160 μm
Printing temperature	260 °C
Pneumatic pressure	0.1 to 0.2 psi
Printing voltage	1700 V or higher
Standoff distance	100-200 μm
Printing speed	0.5-1 mm/s

3.2 Fabrication of the Electrothermal Actuator

The overall fabrication process of the PI/Bi58/PDMS electrothermal actuator is illustrated in Figure 3.4 (a). To prepare a suitable substrate for EHD printing, a layer of PDMS was coated onto a glass slide. The PDMS was prepared using Sylgard 184 (from The Dow Chemical Company). The silicone elastomer base and curing agent were mixed with a suggested ratio of 10:1. After adequate agitation, it was degassed for 2 hours before coating. When the PDMS was fully cured, the microfilament heater was printed on the substrate by EHD printing. Then, a PI tape, which has a 30 μm PI layer and 38 μm thickness silicone adhesive layer, was pressed against the heater. After peeling off PDMS from the PI tape, the heater was transferred from PDMS substrate to the PI tape. Thereafter, copper wires were connected to the printed heater using gallium-indium liquid metal drops. Finally, a layer of PDMS was coated onto the microfilament heater and the PI layer with controlled PDMS layer thickness. When the top PDMS layer was fully cured, the actuator was produced by cutting the bimorph film into a 7×35 mm strip. Figure 3.4 (b) shows the sectional view of the fabricated electrothermal actuator.

3.3 Design and Modeling of the Electrothermal Actuator

To improve the overall performance of the soft electrothermal actuator, the heater needs to be designed carefully. The Bi58/Sn42 solder was selected to print the heater due to its appropriate melting point of 138 °C and suitability for EHD printing. The embedded resistive heater generates Joule heat when a voltage or current is applied. The induced temperature change causes large thermal expansion mismatch between the PDMS and PI layers, which results in bending actuation.

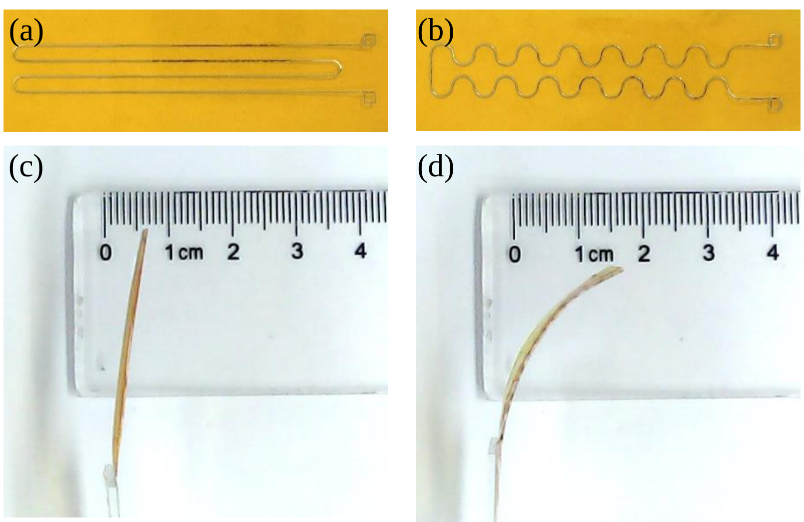

Figure 3.5 Bending performance of actuators with different heater patterns. (a, b) Two designed patterns of the printed heater. (c, d) The corresponding bending deformation of the two actuators at the same temperature.

The area coverage and the stiffness are two major design considerations of the microfilament heater. The embedded heater could adversely increase the overall stiffness of the soft actuator and reduce its deformation and actuation capability, especially considering the fact that the Young's modulus of Bi58/Sn42 is much larger than that of PI and PDMS. Nevertheless, the good thing is that we can freely design the printing pattern of the heater using EHD printing technology. It is therefore very important to design a heater pattern that covers the whole actuator efficiently, while on the other hand, does not add too much stiffness to the actuator. We designed and compared two different heater patterns: a reciprocating zigzag pattern and a half circle curved pattern. Figure 3.5 (a) and (b) show the two printed heater patterns. Apparently, to cover the same heating area, the zigzag pattern has four parallel filaments on the bending plane, while the half circle curved pattern has only two filaments, which indicate a smaller bending stiffness to resist the actuation effect. As a result, a large actuation can be expected from the half circle curved pattern, which was proven experimentally as shown in Figure 3.5 (c) and (d). When both actuators were heated up to 60 °C, the actuator with the half circle patterned heater reached a displacement of 15 mm while the other actuator only had a bending deformation of about 6 mm. Moreover, compared with zigzag lines patterned heater, the heater with the half-circle pattern can more easily resist strains induced during bending actuation [139, 160]. Therefore, in this study, the half circle patterned heater with a low bending stiffness was selected for the fabrication of the soft electrothermal actuator.

The other factor that significantly influences the actuator's bending performance is the thickness of each layers in the bimorph structure. The bending actuation of the bimorph structure has been well studied [161] with the derived theoretical equation to calculate the bending curvature of a bi-layer thermostat when submitted to a uniform heating. The bending curvature can be calculated as follows:

$$\kappa = \frac{6(\alpha_2 - \alpha_1)(1+m)^2 \Delta T}{h(3(1+m)^2 + (1+mn)(m^2 + \frac{1}{mn}))} \tag{3.1}$$

where κ is the curvature, α_1 and α_2 are CTEs of the materials in two layers (i.e. PI and PDMS, respectively), t_1, t_2 are the thickness of the two layers, $h = t_1 + t_2$, $m = t_1 / t_2$, E_1 and E_2 are Young's modulus of the two layers, and $n = E_1 / E_2$, ΔT is the temperature change.

Using Equation 3.1, the optimal layer thickness of the actuator can be estimated theoretically. However, for our soft actuator design, with the extra printed microfilament heater, the analysis of the bending curvature will be more complicated. To simplify the analysis, approximation was taken to convert our actuator into a bimorph model. For our soft actuator design, the PI tape was purchased directly from market with the given thickness, which had a 30 μm PI film and 38 μm silicone adhesive film. Silicone adhesive has a Young's modulus 1-50 MPa and CTE 250-300×10^{-6} °C^{-1} [162], both of which are very close to PDMS, as PDMS belongs to one kind of silicone. Hence, it should not cause significant deviation if we count the thickness of silicone adhesive to the PDMS layer. For the Bi58/Sn42 solder, its CTE is 16.7×10^{-6} °C^{-1} [163], which is very close to that of PI and significantly different from PDMS. During the actuation, the larger expansion of PDMS layers drives both the PI film and the microfilament heater to bend. The PI film and the microfilament heater can be estimated as a composite layer with the same CTE, but increased stiffness or equivalent modulus by adding the stiffness of the heater and the PI layer together. Since the heater has a repeated half-circle pattern, it is hard to calculate its stiffness directly. We utilized ANSYS FEA simulation to estimate the stiffness of the PI/heater composite film. We compared the deformations of the microfilament heater and pure PI film when the same force was applied on the free end with the other end fixed. At the room temperature, the simulation results showed that the tip deformation of the heater was about the same to that of the PI layer,

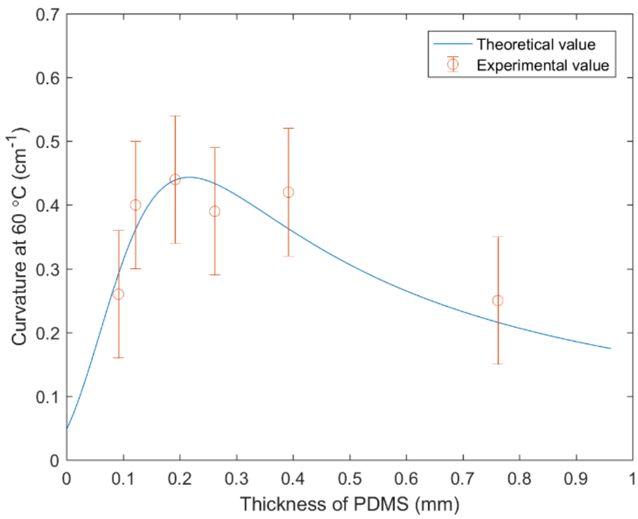

Figure 3.6 The theoretical model and experimental results of relationship between curvature and PDMS thickness at a given actuation temperature.

which indicated the heater's stiffness is approximately same to the PI layer. Note that we want to calculate the actuator's bending curvature at the actuated condition when the temperature is increased from room temperature to the temperature close to the melting point of the solder. Since Bi58/Sn42 is a low melting point alloy, and the heater usually has a higher temperature than the rest area of the actuator, its stiffness will reduce as the temperature is increased by actuation. Assuming an average Young's modulus of the solder to be half its original value, i.e. 19.5 GPa. Then the heater's stiffness is approximately half of that of the PI layer. As we know, stiffness is linearly related to Young's modulus. Therefore, when estimating the bending curvature, the Young's modulus of PI/heater composite layer was selected to be one and half of the original value of the PI film, so as to compensate the stiffness of the microfilament heater.

Now, our soft actuator can be estimated by a bimorph structure. One layer is PI/heater composite film with adjusted Young's modulus of E_1 = 1.5E_0 = 3750 MPa (E_0 is Yong's modulus of PI), the other layer is PDMS with adjusted thickness t_2 = t_0 + 0.038 mm (t_0 is the thickness of coated PDMS, 0.038 mm is the thickness of silicone adhesive) and Young's modulus of E_2 = 2.6 MPa [164]. By varying the thickness of the coated PDMS layer, and for a given temperature change, we can estimate the bending curvature theoretically against the thickness of PDMS (as shown in Figure 3.6 when the temperature change is selected as ΔT = 40 °C from room temperature 20 °C to 60 °C). The maximum curvature was achieved when the thickness of PDMS is approximately 0.25 mm. Too thick or too thin PDMS layer will reduce the actuation capability of the soft actuator. When the PDMS layer is too thin, it cannot generate enough stretching force to bend the PI layer and the heater. On the other hand, if the PDMS layer is too thick, the overall actuation will mostly be thermal expansion rather than bending. To verify the theoretical model, we fabricated a set of actuators with different PDMS layer thickness. These actuators were supplied with DC current and heated to 60 °C. The resulting curvatures were recorded and plotted in Figure 3.6. As can be observed, the experimental results were generally in accordance with the theoretical values. The deviation estimated in the range of ± 0.1 cm^{-1} was due to curvature measuring errors as well as inaccuracy in controlling the layer thickness.

Figure 3.7 The temperature measurement equipment infrared camera FLIR A655sc.

3.4 Characterization and Evaluation of the Electrothermal Actuator

The soft electrothermal actuator was fabricated with the optimized heater pattern and layer thickness. This actuator has a dimension of 7×35 mm, a total thickness of 0.32 mm. The resistance

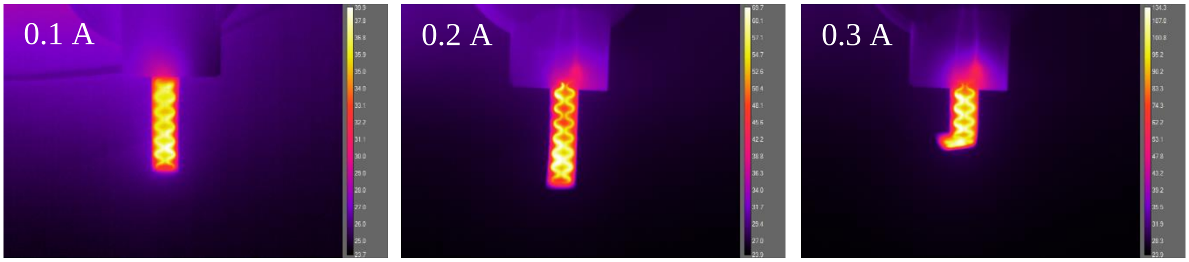

Figure 3.8 Thermograms of the actuator under different currents.

of the printed heater at room temperature was measured to be about 9 Ω. The actuator was first characterized on its heating performance with regard to the applied electric current. The temperature of the actuator was measured by an infrared camera FLIR A655sc (as shown in Figure 3.7). From the obtained thermal images, the average temperature of the actuator can be estimated. Figure 3.8 shows the thermograms of a fabricated actuator under different DC currents from 0.1 A to 0.3 A. Even though the temperature of the heating filament is apparently higher, the heat distribution on the bimorph films is generally uniform.

To explore the heating and cooling response of the electrothermal actuator, we measured the average temperature of the actuator over time when the current was first applied at 0 s and cut

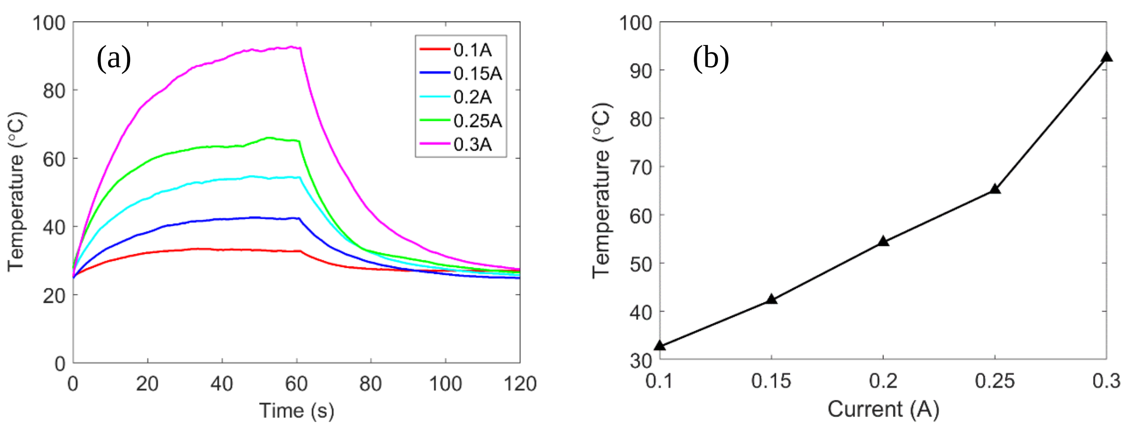

Figure 3.9 Heating performance of the actuator. (a) The temperature change as a function of time at different applied currents. (b) The achieved stable temperature at different currents.

off at 60 s. Figure 3.9 (a) shows the change of the average temperature as a function of time at different applied actuation currents. In general, the temperature of the actuator increased rapidly when the current was applied with a time constant about 15 s. Then the temperature increased slowly thereafter and eventually approached and maintained a stable temperature within 60 s. Upon turning off the current, the temperature dropped down sharply at the beginning, and then gradually return to the ambient temperature within 1 minute. Figure 3.9 (b) shows the relationship between achieved stable average temperature of the actuator and the supplied currents. The relationship between applied current and actuator temperature is approximately linear, but a larger gradient is observed at 0.25-0.3 A (probably owe to the increased electrical resistivity at higher temperature).

Along with the temperature change of the actuator, the soft bimorph structure underwent bending deformation. Figure 3.10 shows the gradual bending status of the actuator when the microfilament heater in the actuator was supplied with a 0.3 A current at 0 s, and then cut off at 60 s. We measured the bending curvature of the actuator each 5 seconds. The bending curvature

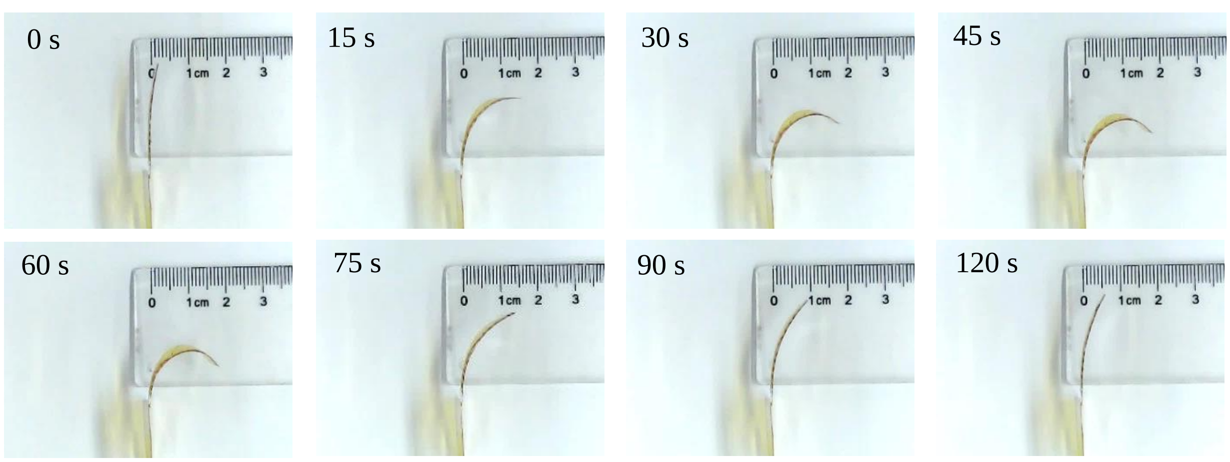

Figure 3.10 The bending of the soft actuator at different time moments.

of the actuator over time followed the trend of the temperature change as measured by the infrared camera in Figure 3.9. As shown in Figure 3.10, the actuator responds quickly within the first 30 seconds, and then deforms slowly and eventually approaches a stable curvature or bending radius. Using the graphical fitting with the captured image, the maximum curvature of about 1.0 cm^{-1} was achieved at the current of 0.3 A. After turning off the current, the actuator restored quickly to a curvature 0.3 cm^{-1} within 20 s. Since the heat dissipation is proportional to the temperature gradient, along with the decrease of the actuator's temperature, the temperature drop rate was reduced as well. As a result, the curvature of the soft actuator decreased slowly back to 0.15 cm^{-1} about 1 minute after turning off the current. The actuator can restore back to its initial shape with little residual deformation (smaller than 0.1 cm^{-1}) after about an extra 30 seconds.

The bending deformation of the soft actuator at five different actuation currents was also characterized, as shown in Figure 3.11 (a). Since the deformation of the actuator is directly controlled by the temperature, the trend of the actuator bending is very similar to that of the temperature. As can be observed, the bending deformation of the actuator increased rapidly at the beginning when the currents were first applied. Then the deformation increased slowly thereafter and approached to and maintained the steady state maximum deformation within 60 s. Upon turning off the current, the deformation of the actuator dropped down sharply at the beginning, and then gradually return to their initial shape with very little residual deformations within 1 minute. Figure 3.11 (b) shows the relationship between the achieved maximum bending deformation of the actuator and the supplied currents, in which an approximately exponential relationship was observed. This exponential relationship between the actuation current and the resulting deformation is a little different from the previous observation of the linear relationship between the actuation current and the resulting temperature in Figure 3.9 (b) and the linear relationship between the temperature and the bending curvature from the theoretical model in Equation 3.1. Such a discrepancy can be well explained by the reduced stiffness of the heater when the temperature goes up, which is not counted in the theoretical model and Equation 3.1. At the elevated temperature, the solder alloy and the polymer layers (PI and PDMS) in the soft actuator all have a lower Young's modulus and become less stiff, which produce larger bending deformation with the same thermal expansion effect.

Reliability is another important factor for the soft electrothermal actuators. To evaluate the performance of the actuator under repetitive operations, we tested the soft actuator under a cyclic current for tens of time. A current with a waveform of square wave was applied with current ON for 60 s and OFF for the other 60 s. Figure 3.11 (c) shows the response of the soft actuator as a function of time for five cycles. As can be clearly observed, the deformation of the actuator demonstrated stable and consistent responses under cyclic current waves. We further tested the actuator more than 100 times, and the almost identical bending responses were observed.

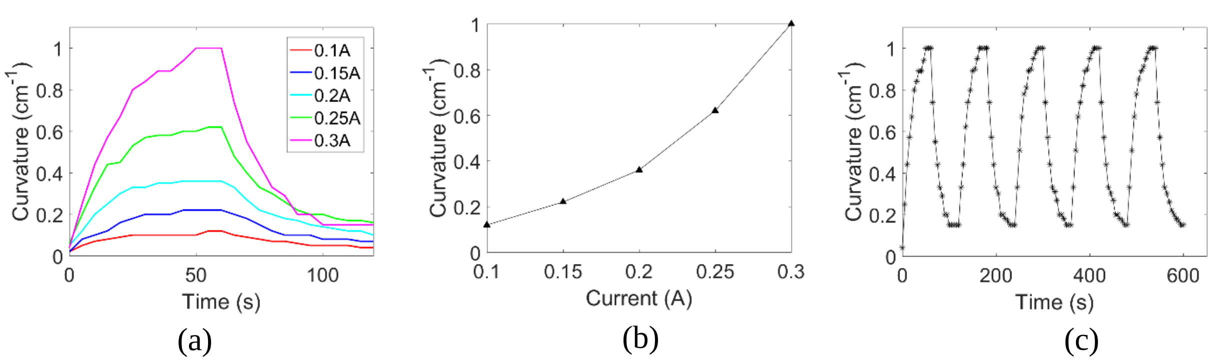

Figure 3.11 Characterization of the bending performance of the actuator. (a) The bending curvature of the soft actuator over time at different currents. (b) Maximum curvatures achieved at different currents. (c) The resulting actuator curvature over time for five repetitive cycles.

3.5 Chapter Summary

This chapter discusses the EHD printing technology and system. Printing parameters for

Bi58/Sn42 are provided. The fabrication process, design, and modeling of the electrothermal actuator are illustrated. Finally, the electrothermal actuator is characterized on its heating and bending performance.

CHAPTER 4: SELF-SENSING CONTROL OF THE ELECTROTHERMAL ACTUATOR

4.1 Introduction to Self-Sensing Control of Soft Actuators

High precision operation of soft actuators is critical, while challenging, for many applications. One inherent drawback of electrothermal actuators is the nonlinear and complex relationship between the actuation voltage and the resulting bending curvature. Moreover, due to the low stiffness structure and longer thermal time constant, the open-loop operation of soft electrothermal actuators usually has a long transient time and is susceptible to external environment variations. Therefore, the closed-loop control is critical to improve the performance of the soft actuators for high precision and dedicated applications.

Closed-loop control of soft actuators or other micro-scale devices can be realized either using an external sensor or the so-called self-sensing technology, also known as sensorless control. Adding an external sensor to the soft actuator not only increases the fabrication complexity and device costs, but also has a negative influence on its structural flexibility and weight. Instead, self-sensing technology integrates the actuation and sensing functions together, eliminates the need for external sensors, and could largely simplify the development of the closed-loop control system. Two most commonly used self-sensing methods are resistive self-sensing [165-168] and capacitive self-sensing [169-173]. Selection of these sensing strategies largely depends on the correlation between the measurands and the features of the actuator. Resistive sensing usually involves the temperature or strain related electrical resistance change of a conductive or semi-conductive component of the actuator. Capacitive sensing, on the other hand, needs a built-in capacitor structure (two electrical conductors separated by a dielectric medium), and is often used to sense position/shape changes related signals. For instance, Merced et al. [165] used a self-sensing approach to control the displacement of a vanadium dioxide (VO_2) based microelectromechanical actuator by monitoring the resistance of the VO_2 film. Tang et al. [166] applied resistive self-sensing technology for the closed-loop position control of a twisted and coiled actuator. The actuation is resulted from the thermal expansion of polymer fibers when heated by the coiled nickel wire, whose resistance varies linearly with the temperature. Sonar et al. [167] developed a closed-loop haptic feedback control of a soft pneumatic actuator. The actuator's inflation state was detected by the resistance change of the embedded thin biphasic metal films, for the purpose of controlling the average strain of the actuator and allowing for generating uniform output force under different loading conditions. Ouyang et al. [168] utilized the piezoresistive feature of a silicon-based microactuator to realize its positioning control. Capacitive self-sensing has also been widely studied for the closed-loop control of dielectric elastomer actuators (DEAs) and MEMS devices. For instance, Gisby et al. [169] created a self-sensing system for measuring the key electrical parameters of DEAs, and used it for the closed-loop control of the area of an expanding dot DEA using capacitive feedback. Zhang et al. [170] proposed a capacitive self-sensing mechanism in the closed-loop control of the actuation force in a DEA. Rosset et al. [171] studied the self-sensing of DEAs, and implemented capacitive self-sensing on the closed-loop control of the strain of a DEA tunable grating. Rizzello et al. [172] realized the closed-loop control of the displacement of DEAs based on resistive and capacitive self-sensing. The actuator's displacement was estimated by the relationship between electrical parameters and actuator geometry. Dong et al. [173] adopted a capacitive self-sensing approach to realize the simultaneous actuation and displacement sensing of MEMS electrostatic drives.

The electrothermal actuator is a nonlinear system (active heating, passive cooling [174, 175]). This asymmetry imposes difficulties for the control system. The control capabilities for heating and cooling responses usually are different. Specifically, when the actuator is directed to heat up, the initial control voltage can be excessive to accelerate the process. Most of the time, this ephemerally excessive voltage does not need to be limited and will not damage the actuator. However, the control effort for the cooling operation, even though can still drop to a lower level temporarily, is restricted by the zero-power limit, as a saturation nonlinearity [176]. To the best of our knowledge, this issue is not well studied by previous research. For example, in [165], an actuation region is selected so that the step-up and step-down responses are similar. In [166], the step-down response of the actuator is largely a natural heat dissipation process in which the controller has little influence over the control signal. In the work of [167, 168], only step-up response and setpoint holding were tested, respectively. Meanwhile, most of these previous works used a single set of control parameters for both heating and cooling, which could be ineffective for unbalanced heating and cooling capability.

In this work, a self-sensing approach was developed to sense the displacement (i.e. bending) of the soft electrothermal actuator. The self-sensing mechanism is based on temperature-incurred resistance change of the soft electrothermal actuator. As the changed temperature acts as the actuation effect to bend the actuator by the mismatch of thermal expansions between the two films, the temperature and the resulting displacement of the actuator can be detected by the resistance change of the heater filament from the linearly related temperature-resistive effect. In this work, a proportional-integral-derivative (PID) controller was designed for the closed-loop control of the bending curvature of the electrothermal actuator, due to its simplicity, efficiency, and reliability [177, 178]. To accommodate the different control capabilities of the actuator in the heating (bending) and cooling (retracting) stages, a switching PID control algorithm with two sets of control parameters was designed and tuned to control the actuator separately in the heating and cooling stages. Compared with the open-loop operation, the PID controlled actuator largely enhances the response stability, rapidity, and robustness.

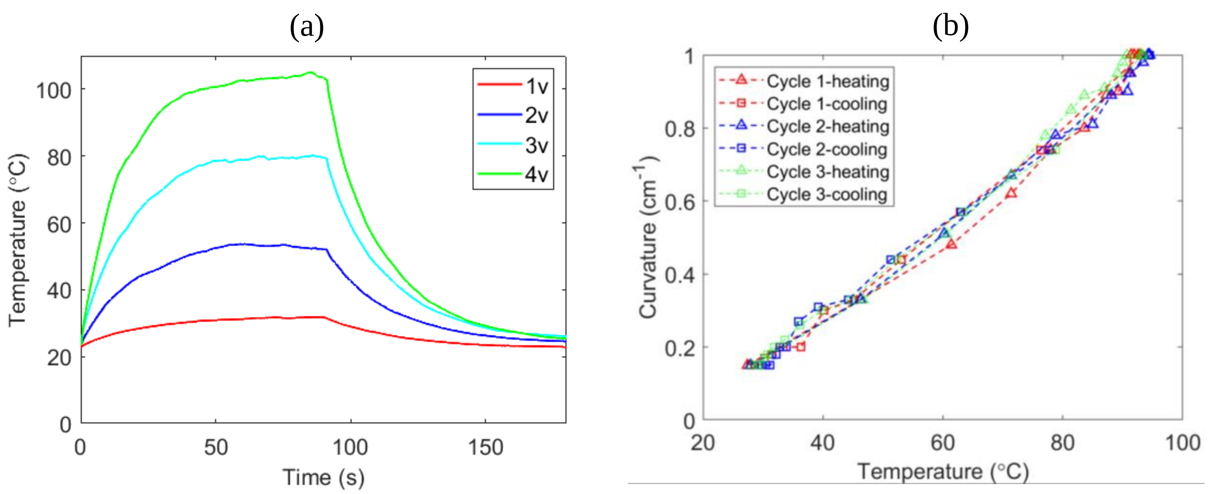

Figure 4.1 (a) The change of the average temperature of the actuator as a function of time at different actuation voltages. (b) The achieved curvature at different measured average temperature of the actuator.

4.2 System Description and Dynamic Model of the Electrothermal Actuator

The fabricated actuator was characterized on its heating performance and the actuation capability with regard to the applied electrical signal. The temperature of the actuator was measured by an infrared camera (FLIR A655sc). From the obtained thermal images, the average temperature of the actuator can be estimated. To characterize the dynamic heating and cooling responses of the soft actuator, the average temperature of the actuator was measured over time when the voltage was first applied at 0 s and turned off at 90 s. Figure 4.1 (a) shows the change of the average temperature as a function of time at different applied actuation voltages. The temperature of the actuator increased rapidly when the voltage was applied. Then the temperature increased slowly thereafter and eventually approached and maintained a stable temperature within 50 s. Upon turning off the voltage, the temperature dropped down sharply at the beginning, and then gradually returned to the room temperature within 1 minute. For both the heating and cooling stages, a rough first-order response is observed from Figure 4.1 (a). The time constant is about 15 s in the heating stage and 18 s in the cooling stage. We also measured the bending curvature of the actuator at different temperatures, as shown in Figure 4.1 (b). A curvature gauge, consisting of a series of circles with different curvatures (0.1 cm^{-1} resolution), was used to measure the bending curvature. The profile of the actuator was projected to the gauge using a digital camera, and the bending curvature was decided by the best fitted circle. From Figure 4.1 (b), an approximately linear relationship is observed. Along with the temperature change of the actuator, the soft bimorph structure produces bending deformation.

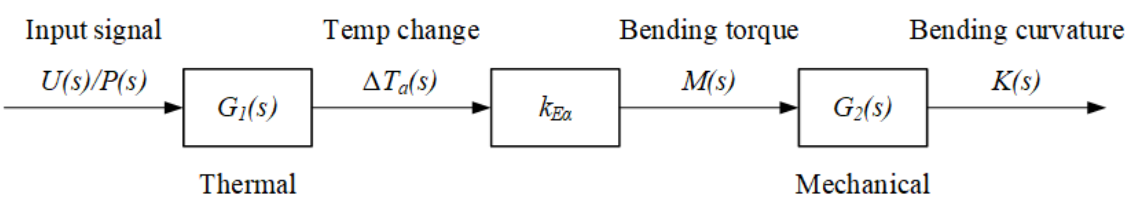

Figure 4.2 The dynamic model of the soft electrothermal actuator.

The operation of the soft electrothermal actuator includes coupled electrothermal and thermal-mechanical behavior. The block diagram for the dynamic model of the soft electrothermal actuator is shown in Figure 4.2. The input signal of the soft actuator is the supply actuation voltage or the related heating power $P(s)$ of the actuator. $G_1(s)$ describes the thermal transfer function from heating power to the temperature change of the actuator $\Delta T_a(s)$. The temperature increase of the bimorph structure generates a bending torque $M(s)$ due to the mismatch of thermal expansions by a linear coefficient $k_{E\alpha}$. The thermally induced bending torque drives the actuator and produces a certain bending curvature $K(s)$. The transfer function of the mechanical response of the actuator from the bending torque to the resulting bending curvature is described by $G_2(s)$.

To model the thermal response of the actuator, the heating/cooling process of the actuator can be expressed by the following formula [179]:

$$C_H m(T_a - T_0) = Q_g - Q_d \tag{4.1}$$

where C_H is heat capacity ratio of the actuator and m is mass of the actuator, T_a and T_0 are the temperature of the actuator under actuation and initial temperature of the actuator, Q_g is the thermal energy from Joule heating generated by the heater and Q_d is the total dissipated thermal energy. The dynamic model of the temperature change and the actuation input can be derived by differentiating Equation (4.1) with respect to time t:

$$C_H m \frac{dT_a}{dt} = P - \Phi \tag{4.2}$$

where P is the Joule heating power, Φ is the heat dissipation power. Heat dissipation from the actuator involves conduction, radiation, and convection. Conduction is negligible if the film is not connected with a good thermal conductor. Radiation is also negligible in the temperature range of interest in the paper [180]. Air convection is the major mechanism of heat dissipation, which is proportional to the temperature difference:

$$\Phi = hA\Delta T_a \tag{4.3}$$

where h is the heat transfer coefficient, A is the surface area of the actuator, $\Delta T_a = T_a - T_0$ is the difference between the actuator temperature and its environmental temperature. Considering $d\Delta T_a / dt = dT_a / dt$, we can rearrange Equation (4.2) to:

$$C_H m \frac{d\Delta T_a}{dt} = P - hA\Delta T_a \tag{4.4}$$

Through Laplace transform, we can obtain the transfer function from the input power to the resulting temperature change of the actuator as:

$$G_1(s) = \frac{\Delta T_a(s)}{P(s)} = \frac{1}{C_H ms + hA} \tag{4.5}$$

The bending torque of bimorph structure largely depends on the temperature change by a constant $k_{E\alpha}$, which is related to the Young's modulus and coefficient of thermal expansion of the materials in the bimorph structure:

$$\frac{M(s)}{\Delta T_a(s)} = k_{E\alpha} \tag{4.6}$$

With a certain temperature-induced actuation torque M, the dynamic model of the actuator's angular displacement can be described by the rotational mass spring damper system:

$$M = J\ddot{\theta} + C_r\dot{\theta} + K_r\theta \tag{4.7}$$

where J is moment of inertia, θ is rotation in radian, C_r is rotational damping coefficient and K_r is rotational spring constant. The transfer function from the torque to the resulting bending displacement of the actuator is:

$$\frac{\theta(s)}{M(s)} = \frac{1}{Js^2 + C_r s + K_r} \tag{4.8}$$

The bending profile of the actuator is approximated to be an arc (i.e., uniform curvature through the length). The bending curvature is proportional to the angular displacement of the actuator, as $\kappa = \theta / L$, where L is the length of the actuator. Accordingly, we are able to obtain the transfer function from the torque to the bending curvature of the actuator:

$$G_2(s) = \frac{\mathrm{K}(s)}{M(s)} = \frac{1}{L(Js^2 + C_r s + K_r)} \tag{4.9}$$

After modeling the coupled electrothermal and thermal-mechanical behavior of the actuator, the overall dynamic model of the actuator can be derived as:

$$G(s) = k_{E\alpha}G_1(s)G_2(s) = \frac{k_{E\alpha}}{L\left(Js^2 + C_r s + K_r\right)\left(C_H ms + hA\right)} \tag{4.10}$$

The above model includes both thermal and mechanical responses of the actuator. These responses have quite different time constants. The time constant of the thermal response can be roughly estimated from Figure 4.1 (a), which is about 15 s in the heating stage and 18 s in the cooling stage. With respect to the mechanical response of the soft actuator, the natural frequency of the bimorph structure can be estimated by the natural frequency of one monolithic substrate layer of PDMS, f_s, and the ratio of modulus, thickness and density between the PI/heater composite film (i.e. E_f , t_f , ρ_f) and PDMS film (i.e. E_s , t_s , ρ_s) with $E_r = E_f / E_s$ = 3750 MPa / 2.6 MPa = 1442, $t_r = t_f / t_s$ = 0.03 mm / 0.288 mm = 0.1, $\rho_r = \rho_f / \rho_s$ = 1712 kg·m^{-3}/ 965 kg·m^{-3} = 1.77 [181], as

$$f_{bi} = f_s \sqrt{\frac{(E_r t_r^3 + 1)(E_r t_r + 1) + 3E_r t_r (t_r + 1)^2}{(\rho_r t_r + 1)(E_r t_r + 1)}} \tag{4.11}$$

in which f_s of PDMS layer can be calculated by

$$f_s = \frac{(1.875)^2}{2\pi L^2} \sqrt{\frac{EI}{\rho A}} \tag{4.12}$$

where L = 40 mm is the length of the actuator, E = 2.6 MPa is the Young's modulus of PDMS, I

Mode 1: 3.5 Hz Mode 2: 21.8 Hz

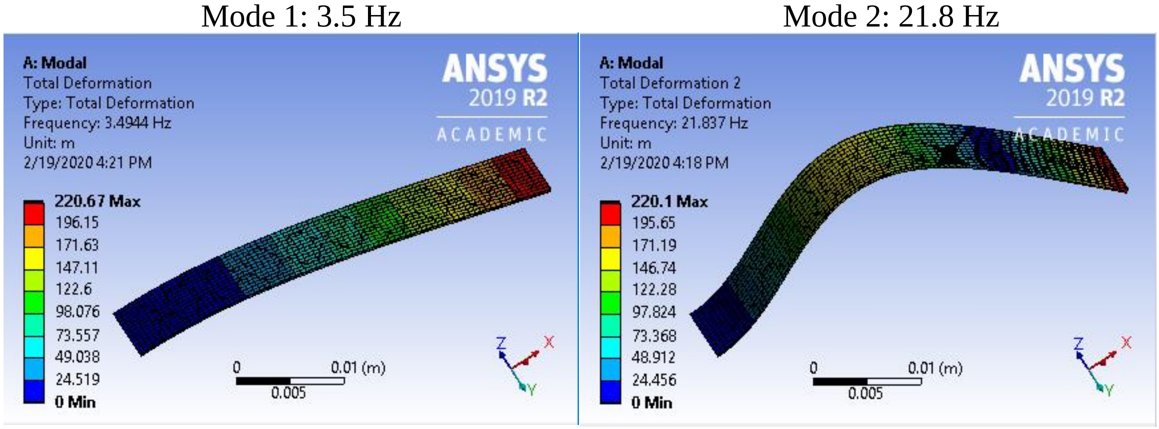

Figure 4.3 First two vibrational modes and their corresponding frequencies for the mechanical structure of the electrothermal actuator.

$= 13.9\times10^{-15}\ \mathrm{m}^4$ is the area moment of inertia, $\rho = 965\ \mathrm{kg\cdot m^{-3}}$ is PDMS's density and $A = 2.016\times10^{-6}\ \mathrm{m}^2$ is the cross-sectional area. Using the above device parameters in Equations (4.11) and (4.12), we can estimate the natural frequency of the actuator to be about 3.4 Hz, which is also verified by the finite element analysis (FEA) simulation results shown in Figure 4.3. The dominant mode from FEA is 3.5 Hz, which is very similar to that from theoretical calculation. This natural frequency indicates a time constant of the mechanical response less than 0.1 s and is much shorter than that of the thermal process. In other words, compared with the thermal response, the mechanical response of the actuator is much faster (two orders of magnitude). Therefore, it is reasonable to ignore the mechanical dynamics, and the actuator's dynamic model can be simplified to a first-order thermal dynamics model for the same reason.

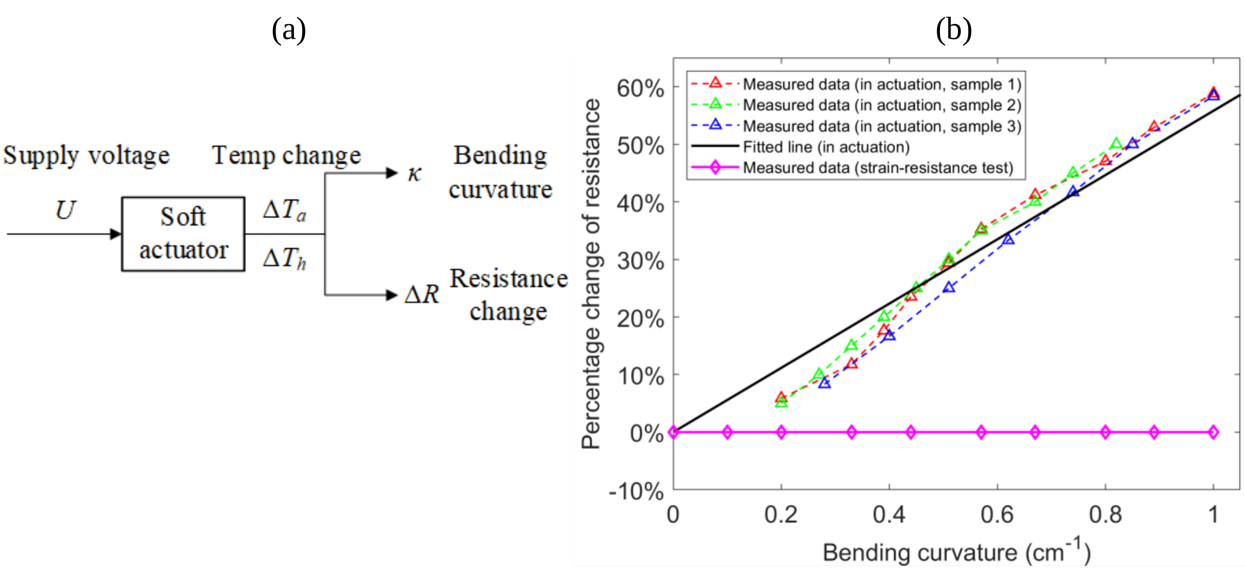

Figure 4.4 (a) Self-sensing mechanism. (b) Relationship between percentage of resistance change and bending curvature.

4.3 Self-Sensing Mechanism for Closed-Loop Control Design

To precisely control the operation of the soft actuator, a proper sensing signal is required to measure the bending of the actuator under different actuation voltages. In this study, we developed a self-sensing mechanism based on temperature-incurred resistance change of the soft electrothermal actuator. As the changed temperature acts as the actuation effect to bend the actuator, the temperature and the resulting displacement of the actuator can be detected by the resistance change of the metal filament (i.e. heater) from the linearly related temperature-resistance relationship. As shown in Figure 4.4 (a), when supplied with electricity, the heater filament heats up the bimorph structure. We assume that the temperature change of the heater, denoted as ΔT_h, and the change of the average temperature of the actuator, denoted as ΔT_a, are linearly related:

$$\Delta T_a = k \Delta T_h \tag{4.13}$$

From previously reported study [182] and our experimental observation, the electrical resistance of Bi58/Sn42 generally varies linearly with temperature change:

$$\Delta R = \alpha R_0 \Delta T_h \tag{4.14}$$

where ΔR is the resistance change, R_0 is the original resistance of the heater filament at room temperature, α is temperature coefficient of resistance for the metal filament.

As has been discussed in Section 3.3 (Equation 3.1), the bending curvature of the actuator is linearly related to its temperature change: $\kappa \propto \Delta T_a$. From these equations, it can be found that the resistance of the heater changes proportionally with the bending curvature of the actuator $\kappa \propto \Delta R$ or $\kappa \propto \Delta R / R_0$. This relationship is also verified by the experimental results as shown in Figure 4.4 (b), which shows the average of multi-measurements of curvature against resistance change in percentage at both the heating and cooling stages for three different actuators. Although there are some deviations at small curvatures possibly due to imprecise measurements, since small curvatures are hard to be measured precisely, they generally follow a proportional trend with linearity error about 10%, and based on the fitted line, $\kappa = 1.775 \times (\Delta R / R_0)$. Moreover, to use the resistance change as the sensing signal to measure the bending of the actuator, we need to make sure other factors, such as the bending and the resulting strain on the heater have neglectable effect on the resistance reading, which was also verified by experiment, as shown in Figure 4.4 (b). The actuator was manually bent to the maximum bending curvature without actuation, with no detectable resistance change being observed. Therefore, the resistance change of the heater filament can be used as the sensing signal to indicate the bending displacement of the actuator. By controlling the real-time resistance of the heater, we are capable of controlling the temperature and the bending curvature of the actuator.

A sensing and control experimental setup was developed for the soft actuator, as shown in Figure 4.5 (a). In the circuit, a shunt resistor is connected in series with the electrothermal actuator. The shunt resistor has a 1 Ω resistance, 1% tolerance and 0.25 W rated power. The electrical resistance of the shunt resistor has been tested independently at different current levels. At 0.3 A and 0.5 A, it only showed 0.6% and 2% resistance increases, respectively. Given the fact that the actuation current is within 0.3 A (0.09 W on the shunt resistor) most of the time, we treat the shunt

(a)

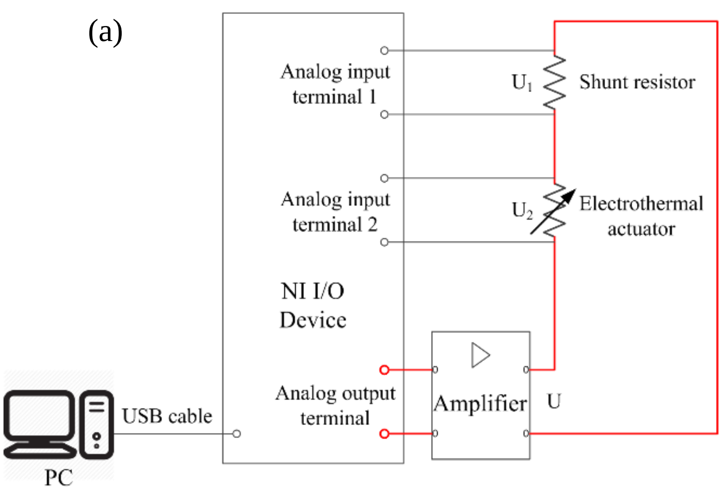

(b)

Figure 4.5 (a) The sensing and control experimental setup. (b) The data acquisition equipment NI USB-6259.

resistor as a constant unit resistor. An NI I/O device (USB-6259 with 16-bit channels and voltage I/O resolution ~ 0.3 mV, shown in Figure 4.5 (b)) is used for data acquisition and to provide control signal. Voltage signals across the shunt resistor and the electrothermal actuator are acquired via two analog input channels on the I/O device using a 1K Hz sampling frequency. U_1 denotes the real-time voltage across the shunt resistor, and U_2 denotes the real-time voltage across the electrothermal actuator. From U_1, the current through the circuit can be calculated as the shunt resistor has a unit resistance. Then, we are able to calculate the real-time resistance of the electrothermal actuator by measuring U_2. The voltage command signal from the analog output terminal on the I/O device is amplified through a voltage amplifier (DSM VF-500, gain = 20.5) to drive the actuator. The I/O device communicates with LabVIEW control program on PC via a USB cable. The control program determines the output voltage through a feedback control algorithm by a 1 ms loop-cycle time. The experimental setup is located in an air-conditioned lab with the temperature around 22 °C.

4.4 Feedback Control of the Electrothermal Actuator

Using the resistive self-sensing signal, a feedback controller was designed and implemented to improve the performance of the soft actuator. Due to the different control capabilities during the heating stage and cooling stage of the actuator, it is difficult for a single controller to provide good response for both the heating and cooling stages, as shown in Figure 4.6. Note that in this work, to allow for effective control during the cooling stage, the initial state (zero point) is defined that the heater maintains a certain resistance at a small actuation voltage (~1.5 V). The bending/unbending tests were conducted as the input (the resistance change ΔR) switched between 0 and 1 Ω.

In Figure 4.6, a single PID controller $C(s) = K_p (1 + 1 / T_i s + T_d s)$ was tuned to control the soft actuator. Nevertheless, it was difficult to tune the controller to simultaneously provide good response for heating and cooling the actuator. For example, for the step response, if the controller was tuned to optimize the response of the positive step (heating of the actuator), the response of the negative step (i.e. cooling of the actuator) showed evident oscillations (Figure 4.6 (a)). On the other hand, if the controller was tuned to provide good response for the negative step, a large overshoot and prolonged settling time were observed for the positive step response, as shown in Figure 4.6 (b). The main reason of such a phenomenon comes from the unbalanced control capabilities during the heating and cooling stages. When the actuator is commanded to bend more at the heating process, the embedded heater can actively heat up the actuator with an excessively high voltage. This ephemerally excessive voltage generally brings no damage to the actuator. In the cooling process, however, the actuator lacks an active and efficient cooling mechanism and mainly relies on reducing the heating power and the natural heat dissipation to cool down the actuator. When the actuator needs to be unbent (i.e. cooled) for some degree, the control voltage

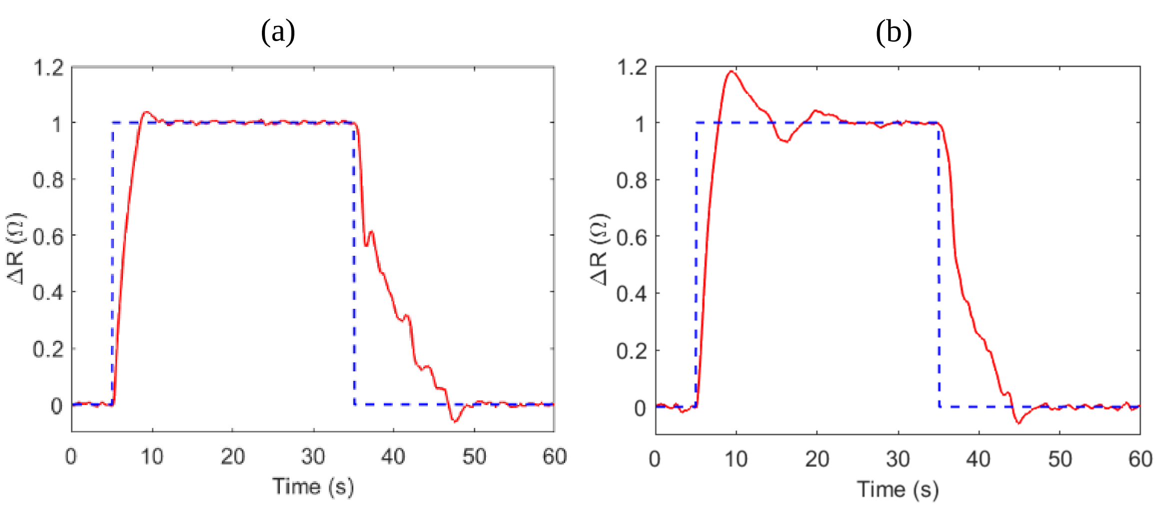

Figure 4.6 (a) A PID controller provided optimized response of positive step, while the negative step response showed evident oscillations. (b) The other PID controller provided stable response of negative step, while the positive step response had large overshoot and prolonged settling time.

needs to be temporarily dropped to a voltage lower than the voltage needed to maintain the target bending, so as to speed up the cooling process. However, such lower voltage command is constrained by the zero-input power. As a result, theoretically unlimited heating power can be achieved by applying a large actuation voltage, while the cooling capability of the actuator is limited and saturated at the zero-input power.

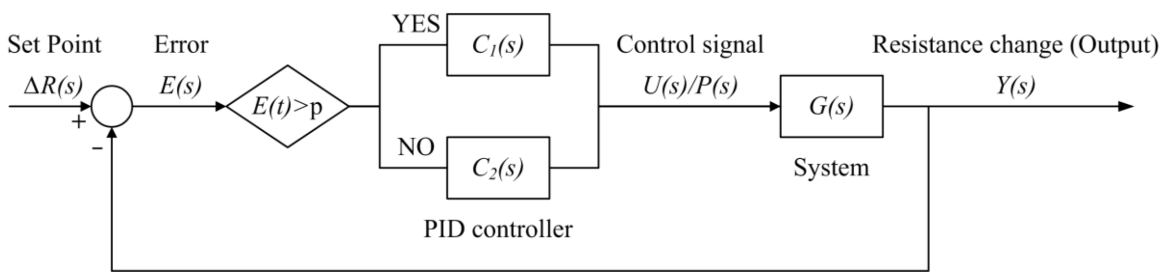

Figure 4.7 The switching PID control algorithm for the soft actuator.

Considering the unbalanced heating and cooling behavior of the soft actuator, a switching PID control algorithm was designed to achieve good control performance in both heating and cooling stages. As shown in Figure 4.7, two PID controllers with different proportional, integral and derivative gains were tuned separately for the positive and negative driving directions (i.e. heating and cooling of the actuator). In the figure, $\Delta R(s)$ represents the reference signal, $Y(s)$ represents the measured system output, $E(s)$ is the error signal as the difference between the reference signal and measured output, $U(s)$ or $P(s)$ represents the control signal, and $G(s)$ is the system transfer function. The switching logic between these two controllers is based on the sign of the error signal $E(t)$ that is measured in real time. To avoid frequent switching at the steady state condition, a threshold value p was selected to enable the switch of the two controllers. If the error signal $E(t)$ is larger than the small threshold value, indicating the requirement of additional heating or bending, the controller tuned for the positive response C_1 will be used. Otherwise, the other

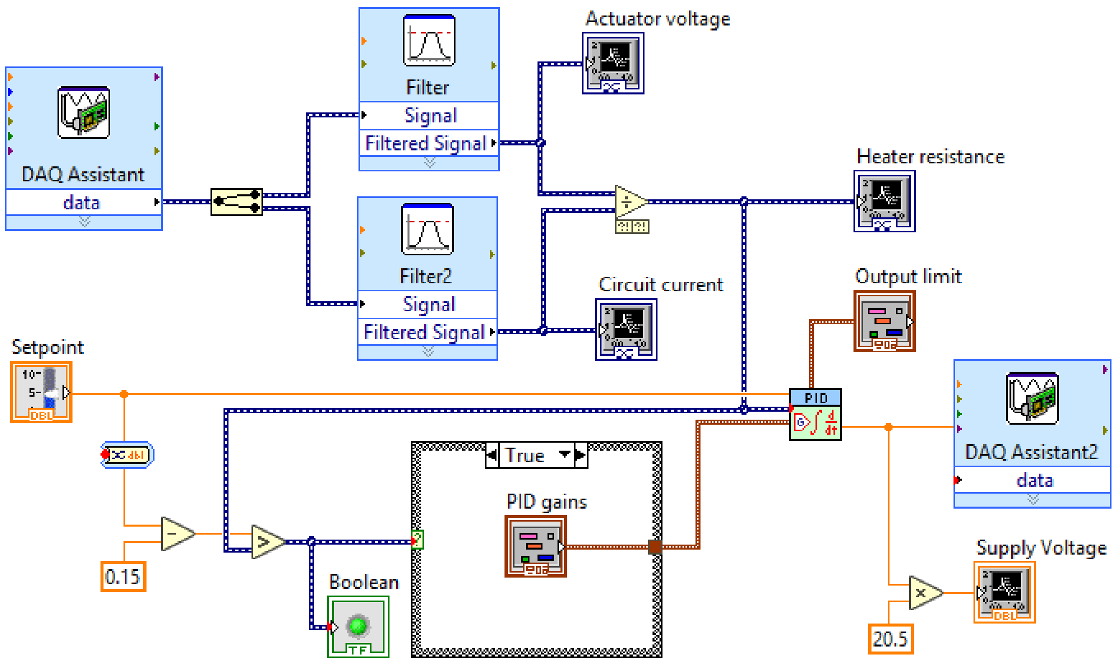

Figure 4.8 The block diagram of the LabVIEW control program.

controller C_2 will be used to obtain good performance for the negative and steady-state responses.

In this study, the PID controller parameters were tuned manually by experiments. Proportional gain K_p, integral time T_i, and derivative time T_d were adjusted one by one until the response results were satisfactory, considering the resulting rising time, settling time, overshoot, steady-state error, and oscillations. For C_1, K_p = 0.5, T_i = 0.6 s, T_d = 0.3 s; For C_2, K_p = 0.1, T_i = 0.6 s, T_d = 0.3 s. It was observed that the integral term is essential to eliminate the steady-state error and enhance the response speed. A small derivative term is also useful for reducing the peak overshoot. The controller was implemented in LabVIEW. Figure 4.8 shows the block diagram of the LabVIEW control program (non-core instruments and components are deleted).

4.5 Experimental Results

The performance of the soft actuator with self-sensing feedback control was evaluated in its static and dynamic responses. Setpoint tracking and resolution is an important performance for an actuator. In this soft actuator, steady state performance and the resolution are primarily restricted by noise, such as environmental disturbance and electronic noise, which degrade the operation accuracy and resolution of the actuator. Figure 4.9 compares the steady state responses of the actuator with feedback control and open loop control. For both cases, the actuator was commanded to bend at a given angle with ΔR of 1 Ω and the corresponding bending curvature of 0.2 cm^{-1} (i.e., bending angle of 0.8 radian or 45.8 ^{o} given the length of the actuator of 40 mm). Clearly, the PID controlled setpoint tracking provided much more stable response with much

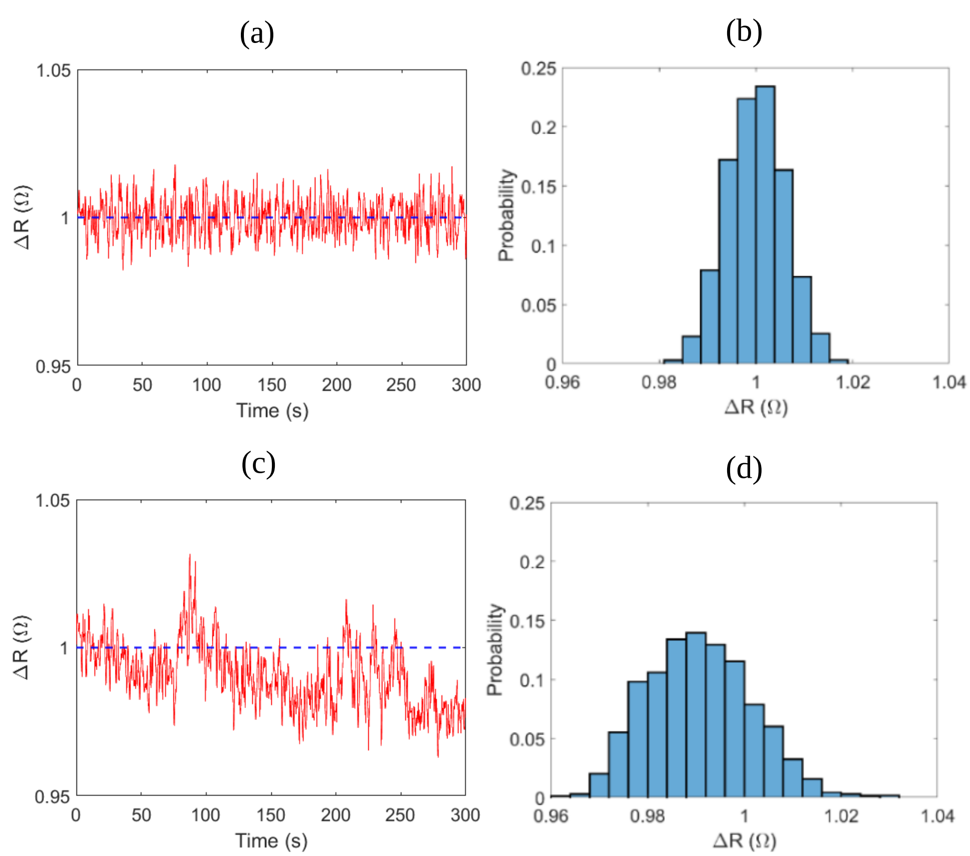

Figure 4.9 (a, b) PID controlled and (c, d) Open loop setpoint tracking and noise histogram of steady state signal.

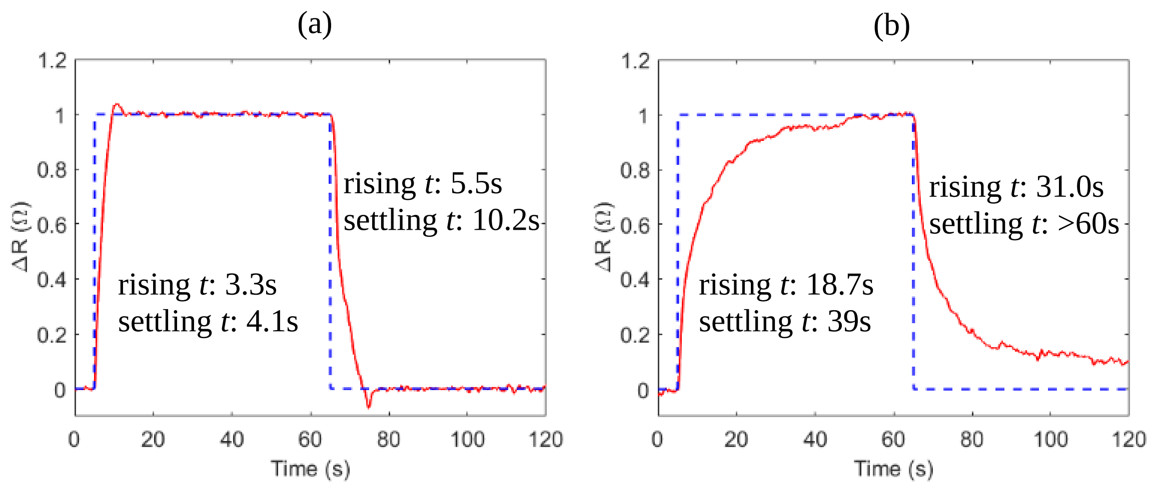

Figure 4.10 (a) Closed-loop and (b) Open-loop step response. Feedback control reduces rising time and settling time over 80%.

smaller derivation from the setpoint value than open loop control. Figure 4.9 also demonstrates a noise histogram of the steady state output from the self-sensing controlled actuator. The standard deviation of the output signal under feedback control is about 0.006 **Ω**, which indicates a bending resolution of 0.0012 cm^{-1} (i.e. angular resolution of bending of 0.275 ^{o}), while the open loop system has a standard deviation of 0.011 **Ω** (i.e. 0.0022 cm^{-1} or 0.504 ^{o}) and also has large steady-state error.

Figure 4.10 demonstrates the step response of the soft actuator in both positive and negative bending directions. The closed loop response provides much shorter rising time and settling time than the open loop step response. The rising time (time between 10% and 90% of unit step) is about 3.3 s (roughly indicates a closed-loop bandwidth of 0.11 Hz) with a 4% overshoot for the positive step, and is about 5.5 s for the negative step. For the open loop system, the rising time is about 18.7 s and 31.0 s respectively for the positive step and negative step. For the settling time, it takes 4.1 s and 10.2 s for the closed-loop system to reach the steady state for the positive and

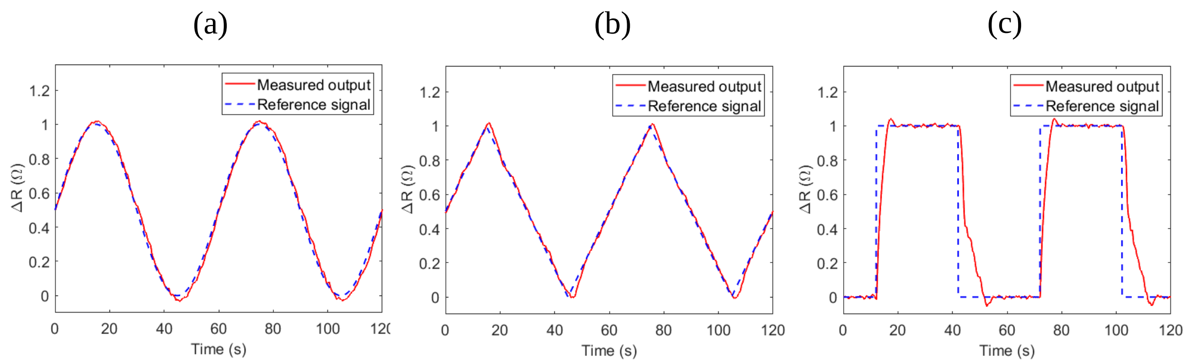

Figure 4.11 Tracking response of (a) Sinusoidal wave, (b) Triangle wave, (c) Square wave.

negative steps respectively, while it takes 39.0 s for the open loop system in the positive step and no settlement was observed for the negative step. Clearly, both rising time and settling time were reduced more than 80% with feedback control using self-sensing feedback signal. To evaluate the dynamics tracking capabilities of the soft actuator, the actuator was commanded with different waveforms, including sinusoidal wave, triangle wave, and square wave. All these waves have a period of 60 s. From Figure 4.11, the output of the actuator follows these reference signals very well, except the sharp command change of triangle wave and square wave.

Disturbance rejection is another critical requirement for high precision reliable operation of the soft actuator, as the miniature devices and soft actuators are susceptible to environmental variations. With self-sensed signal and closed-loop control, the actuator is capable to automatically compensate for these fluctuations of environmental temperature and increase the reliability and robustness. We experimentally demonstrated the disturbance rejection capability of the actuator. As shown in Figure 4.12, the actuator was controlled to bend with ΔR of 1 Ω. Then 0.5 ml iced water (temperature about 0 °C) was flowed onto the actuator by a pipette, as an example of environmental variation. With the help of self-sensing feedback control, the operation of the actuator was only disturbed slightly, and came back to normal condition in about 10 s. As a comparison, the open-loop operated actuator was disturbed significantly with huge change in the bending angle (sensed by resistance), and it took extremely long time to recover from the disturbance. There was still about 25% steady-state error even after 3 minutes. These experimental results clearly demonstrated the effectiveness of resistive self-sensing and feedback control in providing good performance of the soft actuator.

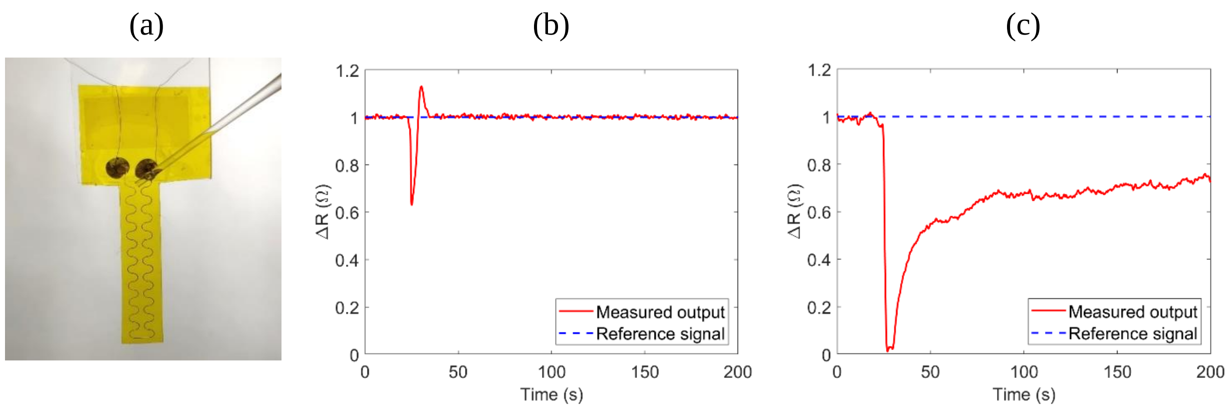

Figure 4.12 Disturbance rejection. (a) Experimental setup. (b) PID controlled response. (c) Open-loop operation.

4.6 Chapter Summary

This chapter discusses the self-sensing control of the soft electrothermal actuator. An introduction is presented for the closed-loop control of soft actuators. Two types of self-sensing approach (resistive self-sensing and capacitive self-sensing) are explained. Then the dynamic model of the soft electrothermal actuator is built, and the self-sensing mechanism is illustrated. A switching PID control algorithm is designed to accommodate the different response characteristics of the actuator in the heating and cooling stages. Lastly, the self-sensing mechanism and the control algorithm are tested on setpoint tracking, step response, wave tracking, and disturbance rejection.

CHAPTER 5: TWISTING DEFORMATION OF THE ELECTROTHERMAL ACTUATOR

5.1 Introduction to Twisting Deformation of Soft Actuators

Twisting deformation represents another degree-of-freedom for soft actuators. When integrated as soft robotics, multi degree-of-freedom motion can largely enhance their versatility and functionality. Generally, twisting deformation can be transformed from a skewed bending deformation, which can be achieved in several different ways.

The easiest way is changing the stiffness anisotropy. Bending deformation tends to occur along the direction with the lowest bending stiffness. If the actuator has reinforcement structures (reinforcing stripes, fibers, or wires) that change its stiffness anisotropy so that the lowest stiffness direction switches to a direction misaligning the transverse axis, the actuator will tend to bend along this skewed direction, and hence a coupled bending and twisting deformation can be obtained. Song et al. [183] developed a shape memory alloy actuator that can achieve coupled bending-twisting actuation. A layered reinforcement structure was embedded in the matrix to vary the mechanical properties of the actuator. When the reinforcement structure has a [0/90/0] orientation, a pure bending deformation is obtained. When the layered reinforcement structure ply configuration is changed to [30/45/30], a bend-twist motion can be achieved.

Another commonly used method to create twisting deformation is changing the actuation direction. For soft pneumatic network actuators, this can be done by orienting the air chambers by an angle from the transverse direction. Wang et al. [184] reported a soft pneu-net actuator that can generate coupled bending and twisting motion, which was achieved by creating oblique air chambers. Through finite element analysis and experimental verification, variation trends of bending and twisting motions with respect to the chamber angle were investigated. Besides, a pure twisting deformation can be achieved by combining two bending actuators that have opposite bending directions as reported in article [185]. Some photo responsive materials exhibit uniaxial deformation or have a dominant deformation direction. Wang et al. [186] developed a dual-layer liquid crystal soft actuator that can bend under ultraviolet irradiation and twist under near-infrared irradiation. The top layer possesses a uniaxially aligned liquid crystalline elastomer matrix incorporated with azobenzene chromophores and a near-infrared absorbing dye, so it bends

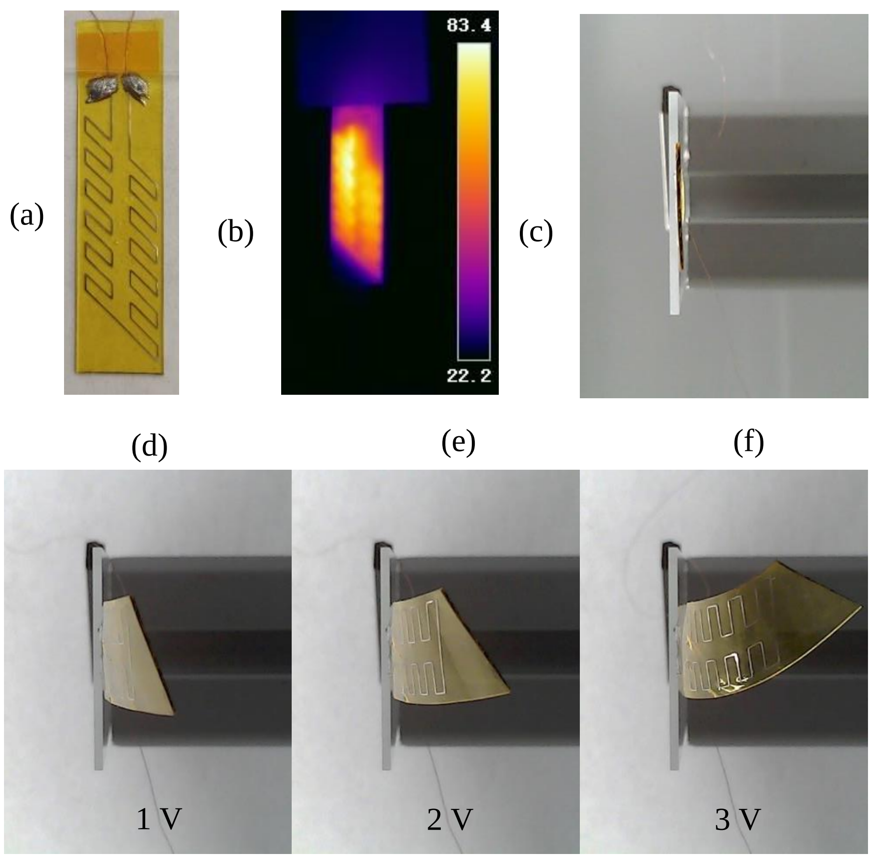

Figure 5.1 (a) The fabricated twisting actuator. (b) Thermography of an actuated actuator. (c) Initial position of the actuator when unactuated. (d) Deformation at 1 V voltage. (e) Deformation at 2 V voltage. (f) Deformation at 3 V voltage.

under ultraviolet stimulus and shrinks under near-infrared stimulus. The bottom layer has only near-infrared dye, and only responds to near-infrared stimulus. Because the shrinkage directions of the top and bottom layer are tilted to each other, the actuator executes twisting deformation under near-infrared irradiation. Haan et al. [187] reported humidity responsive actuators based on a single sheet of a hydrogen-bonded, uniaxially aligned liquid crystal polymer network. The asymmetry in the molecular trigger in the anisotropic polymer film plays a dominant role leading to programmed deformations including bending, folding, and twisting. Similarly, for piezoelectric actuators, twisting deformation can be achieved by either changing the polarization direction [188] or adding inclined piezoelectric segments [189].

5.2 Twisting of the Electrothermal Actuator

Twisting deformation of the electrothermal actuator can be realized by printing a skewed heater pattern as shown in Figure 5.1 (a). This oblique heater can not only generate a parallelogram high-temperature zone as shown in Figure 5.1 (b), but also changes the stiffness anisotropy of the

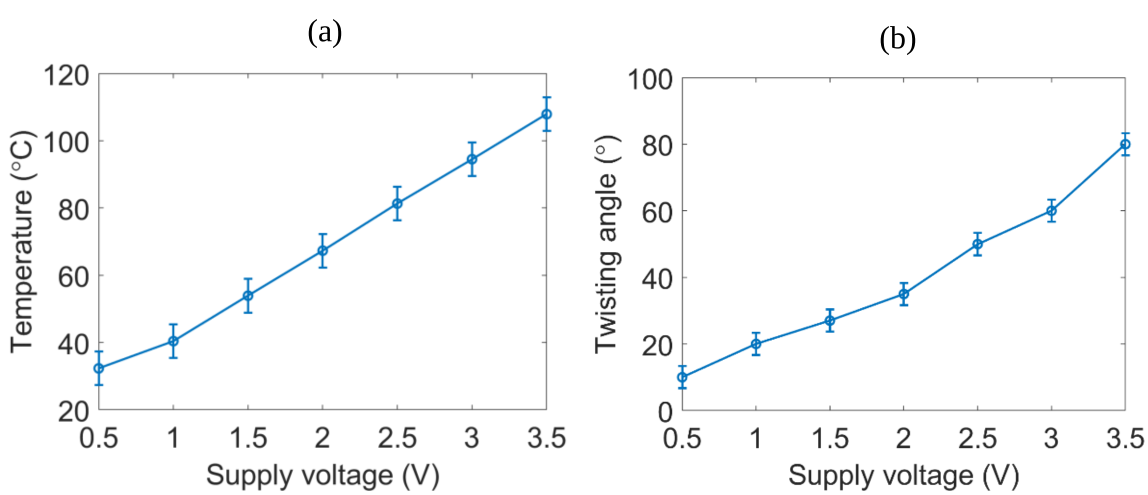

Figure 5.2 (a) The measured average temperature at different voltages. (b) The twisting angle at different voltages.

actuator. For the uniform bending, the transverse direction has the lowest bending stiffness. While for the skewed heater pattern, the heating area and the direction with the lowest bending stiffness shifts to be parallel to the skewed heater filaments. The actuator tends to bend along this oblique direction, resulting in a coupled bending and twisting deformation. Figure 5.1 (c) shows the actuator's initial position before actuation, and Figure 5.1 (d)-(f) show its deformation when the supply voltage is 1 V, 2 V, and 3 V.

We have also measured the actuator's stable average temperature and the twisting angle at different actuation voltages, as shown in Figure 5.2 (a) and (b), respectively. Linear relationship is observed between the actuation voltage and the resulting twisting angle from the actuator. Note that both clockwise and counterclockwise twisting deformation can be obtained by changing the orientation of the heater filaments (as shown in Figure 5.3). A heater pattern inclined to right exhibits a counterclockwise twisting motion (Figure 5.3 (a)), while a heater

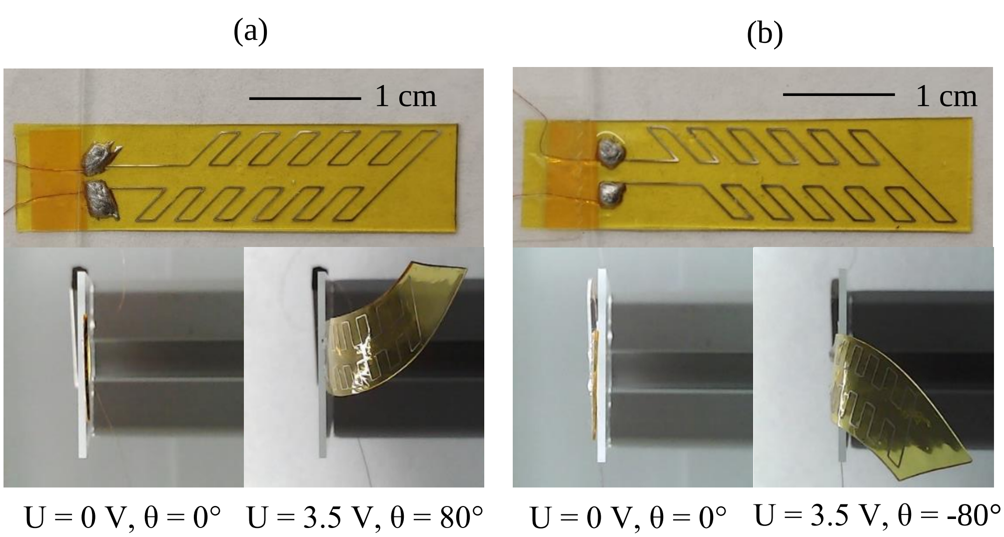

Figure 5.3 (a) A right skewed heater pattern and counterclockwise twisting. (b) A left skewed heater pattern and clockwise twisting.

pattern inclined to left exhibits a clockwise twisting motion (Figure 5.3 (b)). Both actuators can achieve an 80 ° twisting angle when the supply voltage is 3.5 V.

5.3 Modeling of Twisting Deformation

Due to the temperature distribution and stiffness anisotropy, actuators with a skewed heater pattern exhibit coupled bending and twisting deformation when supplied with electricity. This coupled bending and twisting deformation is resulted from a bending deformation that misaligns the longitudinal direction. As shown in Figure 5.4 (a), the actuator can be divided into three segments, a parallelogram segment and two triangle segments. The parallelogram segment undergoes skewed bending deformation, while the two triangle segments mostly remain tangent to the parallelogram segment since their temperature does not increase significantly during the actuation. Figure 5.4 (a) shows the actuator in the original rectangular coordinate system, but this coordinate system is not suitable for theoretical modeling and calculation. Therefore, it has been transferred to

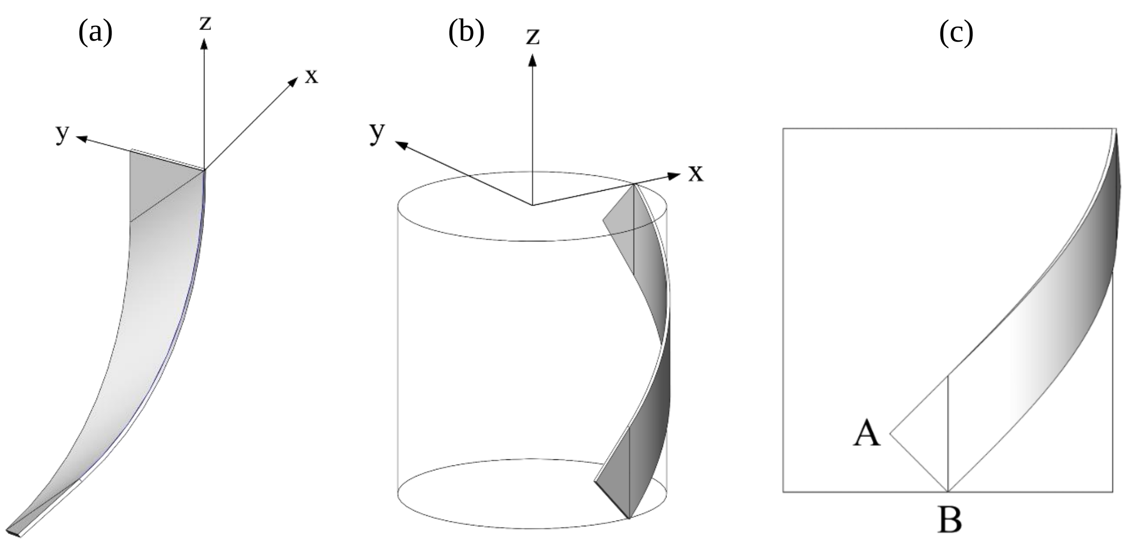

Figure 5.4 (a) The original coordinate system. (b) The calculation coordinate system. (c) Points on the free edge.

another cylindrical coordinate system as shown in Figure 5.4 (b). In the cylindrical coordinate system, Z-axis is the reference axis and X-axis is the reference direction. Assume that the top edge of the actuator is fixed, and the bottom edge is free to deform. In order to find the bottom edge's position and twisting angle, we need to calculate the coordinates of points A and B (as shown in Figure 5.4 (c)), which can be obtained according to the geometrical relationship:

$$A(\rho,\varphi,z)=(\sqrt{R^2+W^2\cos^2\theta},-\frac{\sin\theta(L-W\cot\theta)}{R}-\tan^{-1}\frac{W\cos\theta}{R},-L\cos\theta) \tag{5.1}$$

$$B(\rho,\varphi,z)=(R,-\frac{\sin\theta(L-W\cot\theta)}{R},-L\cos\theta-W\sin\theta) \tag{5.2}$$

in which R is radius of the cylinder, W and L are width and length of the actuator, θ is the heater inclination angle with respect to the longitudinal direction. Cylindrical coordinates then can be transformed into rectangular coordinates in the calculation coordinate system:

$$x=\rho\cos\varphi \tag{5.3}$$

$$y=\rho\sin\varphi \tag{5.4}$$

$$z=z \tag{5.5}$$

The rectangular coordinates in the calculation coordinate system can be converted into the original rectangular coordinate system by transformation of the coordinate system. This can be done by two steps: translate along X-axis by length of R, and rotate around X-axis by -θ (negative sign means a clockwise direction). Afterwards, we are able to find the coordinates of A and B in the original coordinate system using the following equation:

$$\begin{bmatrix} x' \\ y' \\ z' \end{bmatrix}=\begin{bmatrix} 1 & 0 & 0 \\ 0 & \cos(-\theta) & \sin(-\theta) \\ 0 & -\sin(-\theta) & \cos(-\theta) \end{bmatrix}\begin{bmatrix} x \\ y \\ z \end{bmatrix}-\begin{bmatrix} R \\ 0 \\ 0 \end{bmatrix} \tag{5.6}$$

Twisting angle of the free edge can be obtained by calculating the angle between line AB's projection on X-Y plane and Y-axis:

$$TA = \tan^{-1}\left(\frac{x'(B) - x'(A)}{y'(B) - y'(A)}\right) \tag{5.7}$$

5.4 Influence of Design Parameters on the Twisting Angle

Based on the model constructed in Section 5.3, design parameters including actuator length (L), width (W), bending curvature (C), and heater pattern inclination angle (θ) all have an impact

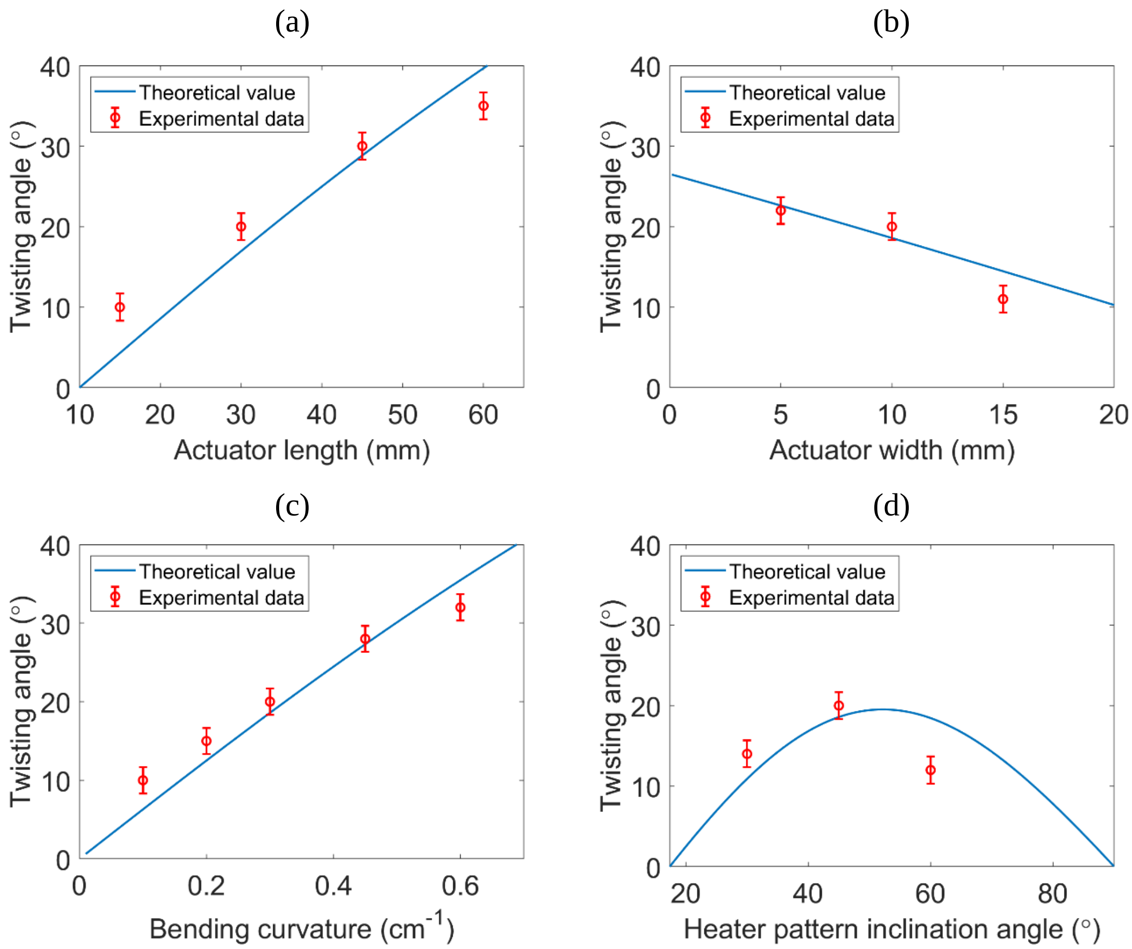

Figure 5.5 (a) The relationship between twisting angle and actuator length. (b) The relationship between twisting angle and actuator width. (c) The relationship between twisting angle and bending curvature. (d) The relationship between twisting angle and inclination angle of the heater pattern.

on the twisting angle. Figure 5.5 (a) shows the relationship between twisting angle and actuator length when other parameters are set as $W = 10$ mm and $\theta = 45$ °. Theoretically, twisting angle is proportional to the actuator length. We have fabricated four actuators whose length ranges from 17 to 62 mm, and measured their twisting angles when the bending curvature was approximately 0.3 cm^{-1}. As we can see from Figure 5.5 (a), the experimental results generally agree with the theoretical trend. Twisting angle is inversely proportional to the actuator width as shown in Figure 5.5 (b), in which actuator length is set to 32 mm and heater pattern inclination angle is 45 °. We have fabricated three actuators whose widths are 5, 10, and 15 mm, and have measured their twisting angles when the bending curvature was approximately 0.3 cm^{-1}. The twisting angle generally decreases as the actuator width increases, following the theoretical trend. When the actuator length is fixed to 32 mm and actuator width is fixed to 10 mm, twisting angle is proportional to the bending curvature as shown in Figure 5.5 (c). Twisting angle at different bending curvatures was measured, which agrees with the theoretical trend. We only measured the twisting angle when the curvature was within 0.6 cm^{-1} as the actuator deformation became largely distorted when the temperature or bending curvature further increased. Lastly, the relationship between twisting angle and the inclination angle of the heater pattern is also presented in Figure 5.5 (d), in which actuator length $L = 32$ mm and actuator width $W = 10$ mm. Note that on the horizontal axis in Figure 5.5 (d), the heater pattern inclination angle starts from 17.35 °, which is the smallest heater inclination angle when the actuator length is 32 mm and actuator width is 10 mm. We have fabricated three actuators whose heater pattern inclination angles are 30, 45, and 60 °, and measured their twisting angles when the bending curvature was approximately 0.3 cm^{-1}. When other fabrication parameters are fixed, the largest twisting angle will be achieved when the heater inclination angle is around 45 °. This is obvious as when the inclination angle gets close to

0 or 90 °, the deformation will mostly be pure bending deformation.

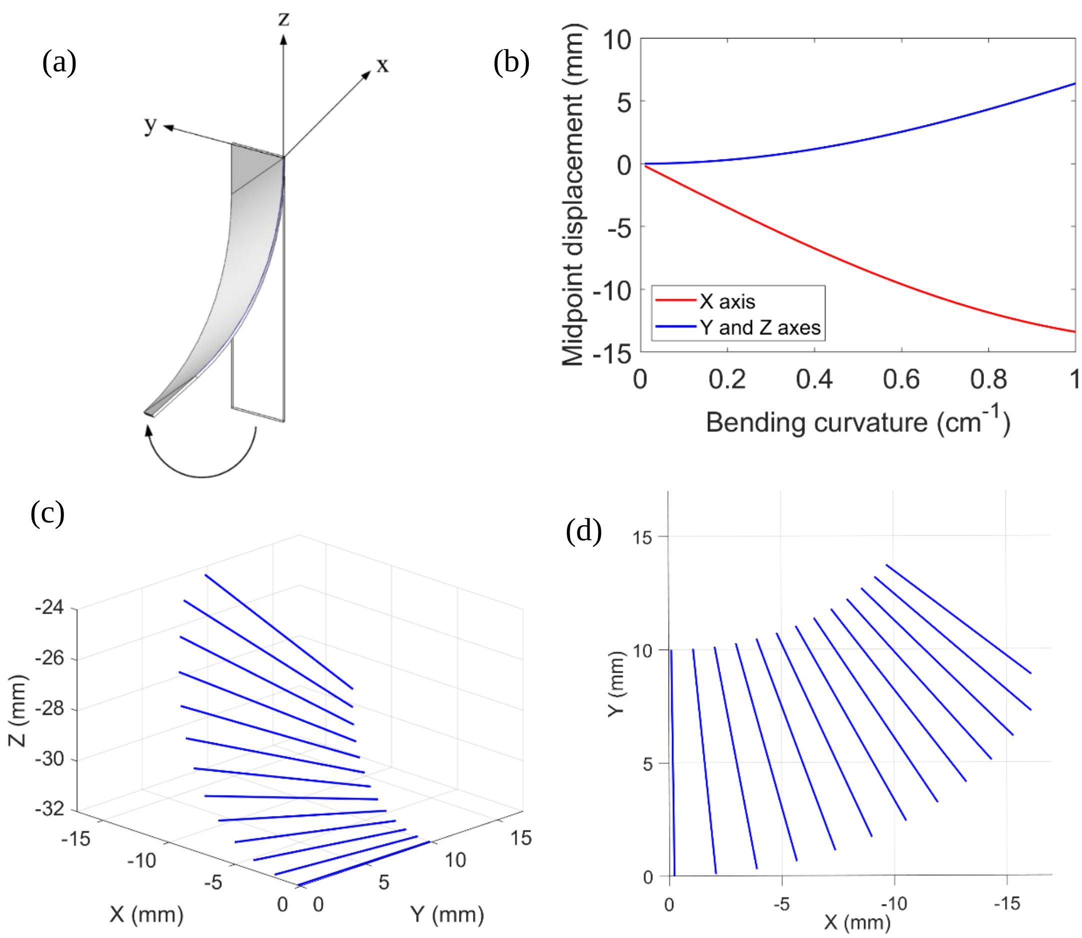

Figure 5.6 (a) Displacement of the free edge. (b) Displacements of the midpoint on the free edge in X, Y, and Z directions. (c) Motion trajectory of the free edge. (d) Bottom view of the motion trajectory of the free edge.

5.5 Motion Trajectory of the Free Edge

We have already obtained the coordinates of the two points on the free edge of the actuator, by which we are able to calculate the position of the free edge (shown in Figure 5.6 (a)). Firstly, we can calculate the displacement of the midpoint on the free edge. This can be done by calculating its coordinate change with respect to its original position (0, W/2, -L). Then its displacements in X, Y, and Z directions are:

$$\Delta x = \frac{x^{'}(A) + x^{'}(B)}{2} \tag{5.8}$$

$$\Delta y = \frac{y^{'}(A) + y^{'}(B)}{2} - \frac{W}{2} \tag{5.9}$$

$$\Delta z = \frac{z^{'}(A) + z^{'}(B)}{2} + L \tag{5.10}$$

The theoretical displacement trend of the midpoint on the free edge in X, Y, and Z directions is shown in Figure 5.6 (b). The actuator length is 32 mm and width is 10 mm, heater pattern inclination angle is 45 °. Figure 5.6 (c) shows the motion trajectory of the free edge when the actuator bending curvature increases from 0 to 1 cm^{-1}. Figure 5.6 (d) shows its bottom view, which indicates a trend similar to the sequential images provided in Figure 5.1.

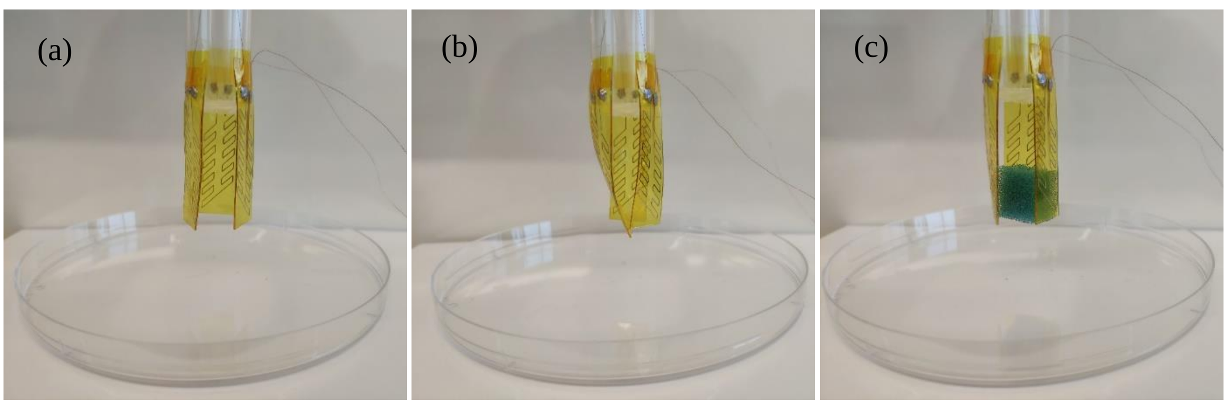

Figure 5.7 Demonstration as a soft gripper. (a) Initial state; (b) Actuated without load; (c) Gripping an object.

5.6 Demonstration as a Gripper

Twisting actuators can be integrated into a gripper to pick-and-place delicate objects. Compared with grippers made of bending actuators, grippers made of twisting actuators have higher adaptability, and can grasp objects more securely with less gripper fingers. Figure 5.7 shows a soft gripper made of three twisting actuators. The three twisting actuators were connected in a series circuit. When the actuators were unactuated, the gripper fingers remained flat (shown in Figure 5.7 (a)). After applying a voltage, the actuators twisted and their tips got closer to each other (shown in Figure 5.7 (b)). We used a foam block as the gripping sample to mimic a delicate object. As shown in Figure 5.7 (c), the soft gripper securely grasped the sample.

5.7 Chapter Summary

This chapter focuses on the twisting deformation of the electrothermal actuator. The design concept and heater pattern for twisting deformation are discussed. The twisting deformation at different supply voltages is characterized. Then, a theoretical model is built for the twisting deformation. Based on that model, influence of the design parameters on the twisting angle is analyzed both theoretically and experimentally. Finally, motion trajectory of the actuator's free edge is studied, and a soft gripper made of three twisting actuators is demonstrated.

CHAPTER 6: FINITE ELEMENT ANALYSIS OF THE ELECTROTHERMAL ACTUATOR

6.1 Modeling of the Electric-Thermal-Mechanical System

Finite element analysis or FEA is the simulation of physical phenomena using a numerical mathematic technique. FEA works by breaking down a real object into a large number (thousands to hundreds of thousands) of finite elements. Mathematical equations help predict the behavior of each element. A computer then adds up all the individual behaviors to predict the behavior of the actual object. This process is at the core of mechanical engineering, as well as a variety of other disciplines, to predict how a product reacts to real-world forces, vibration, heat, fluid flow, and other physical effects. Our electrothermal actuator is an electric-thermal-mechanical coupled multiphysical system. FEA is a powerful tool to simulate and analyze the actuation process and the relationship between supply voltage, temperature distribution, and deformation.

FEA is comprised of pre-processing, processing, and post-processing phases. The goals of pre-processing are to develop an appropriate finite element mesh, assign suitable material properties, and apply boundary conditions in the form of restraints and loads. In the processing phase, the governing equations are assembled into matrix form and are solved numerically. After the model has been solved, the results can be visualized and evaluated, which is known as the post-processing phase of FEA.

The first step of FEA is to create a reasonable geometry or CAD model that reflects the actuator as close as possible. The 3D model of the electrothermal actuator was built using SolidWorks as shown in Figure 6.1. The model consists of three components, a 0.25 mm thickness PDMS layer, a 0.025 mm thickness PI layer, and a Bi58/Sn42 heater filament layer whose profile is a 0.1 mm-diameter semicircle. The cross-section view of the CAD model is shown in Figure 6.1

(a)

(b)

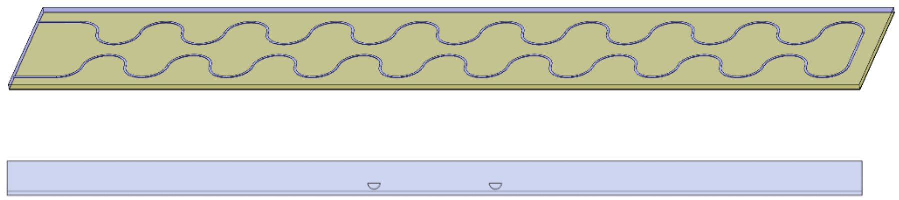

Figure 6.1 (a) CAD model of the actuator in SolidWorks. (b) Cross-section view.

(b), in which the heater filaments are embedded in the PDMS layer. Then, SolidWorks part files were converted to Parasolid files that can be imported into FEA software ANSYS.

The simulation work consists of two analysis systems: a thermal-electric system and a static structural system as shown in Figure 6.2. The two analysis systems share the same engineering data and geometry information, and the solution results of thermal-electric system is used as input load for the static structural system. All engineering data used is listed in Table 6.1, which come from technical data sheet or scientific papers. Note that we assume the Young's modulus for Bi58/Sn42 decreases linearly from 39 GPa to 0 as the temperature increases from 20 °C to 138 °C (its melting point).

Table 6.1 Engineering data used in the FEA simulation.

Properties	Bi58/Sn42	PDMS	PI
Density (kg/m^3)	8720	965	1420
Young's modulus (MPa)	39000-0*	2.6	2500
Poisson's ratio	0.35	0.495	0.34
CTE (ppm/C°)	16.7	320	20
Thermal conductivity (W/mK)	21.6	0.27	0.12
Specific heat (J/g)	46	1.46	1.09
Electrical conductivity (μohm·cm)	34.5	N/A	N/A

* Note: decreases linearly as temperature increases.

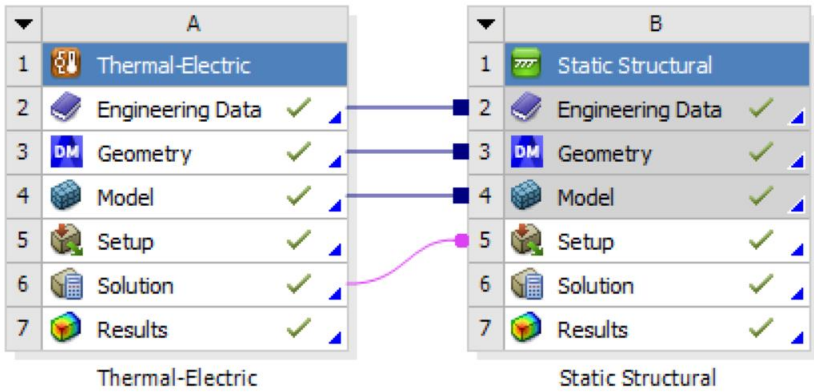

Figure 6.2 The coupled thermal-electric and static structural analysis system.

6.2 Meshing and Simulation Environment Configurations

Once the CAD model is created, it needs to be discretized into elements or be meshed. In the meshing process, the element size is set to about 0.3 to 0.5 mm. Three meshing methods are

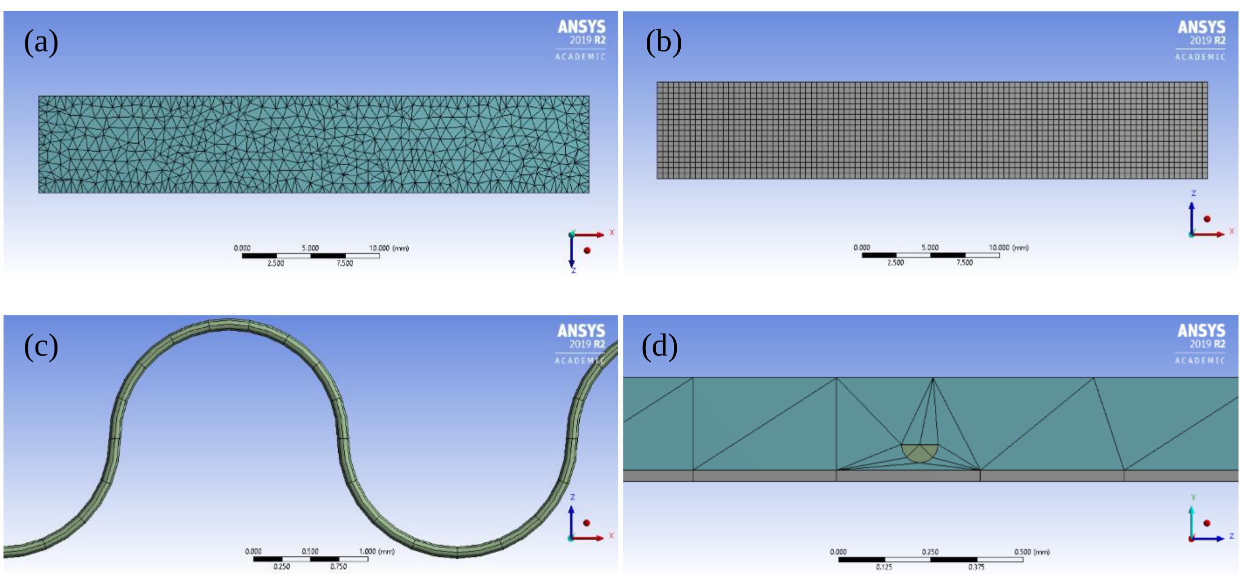

Figure 6.3 The meshing process. (a) Tetrahedron meshing for the PDMS layer; (b) Hexahedron meshing for the PI layer; (c) Sweep meshing for the Bi58/Sn42 filament heater; (d) Shared topology between meshing boundaries.

used. Tetrahedron meshing is used for the PDMS layer (shown in Figure 6.3 (a)), hexahedron meshing is used for the PI layer (shown in Figure 6.3 (b)), and sweep meshing is used for the Bi58/Sn42 filament heater (shown in Figure 6.3 (c)). Meshing methods are selected mainly based on the geometrical features of the object. The PI film has a uniform thickness, so it can be meshed using the hexahedron meshing method. The heater filament has a semi-circular cross-section, and hence a sweep meshing is appropriate. Since the heater filament is embedded inside the PDMS layer, a tetrahedron meshing method is applied to the PDMS layer. Our electrothermal actuator is generally made of elastic materials, and can generate large deformation when being actuated. Due to its high nonlinearity, simulation of elastic materials is much difficult than the conventional rigid

(a)

(b)

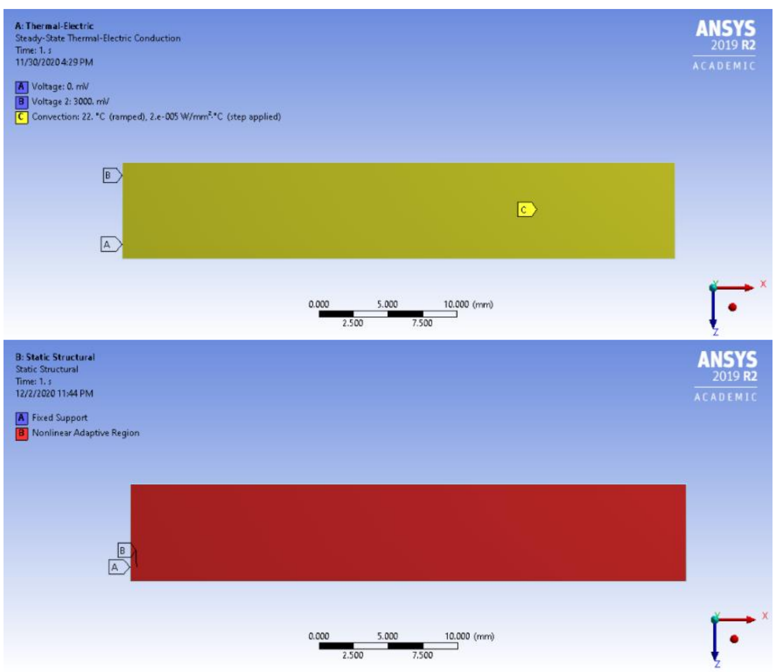

Figure 6.4 (a) Environment configurations in the thermal-electric analysis system. (b) Environment configurations in the static structural analysis system.

structures. To ensure reasonable simulation results and to prevent the three layers from separating each other, topology is shared on the meshing boundaries (shown in Figure 6.3 (d)).

In the thermal-electric system, the environment configurations are set as shown in Figure 6.4 (a). Voltages are applied on the two ends of the heater filament. Voltages can also be changed to electric currents when needed. A constant air convection coefficient 2×10^{-5} W/mm$^2\cdot$°C is applied on the outside surface of the actuator. The environment configurations in the static structural system are set as shown in Figure 6.4 (b). The left edge of the actuator is fixed, while the other parts are free to deform. Nonlinear adaptive region is applied on the whole actuator (discussed below). The complete project hierarchy is shown in Figure 6.5.

To solve this nonlinear simulation project, the large deflection switch should be turned on. In our simulation work, the elements initially became so distorted that the solver could not continue.

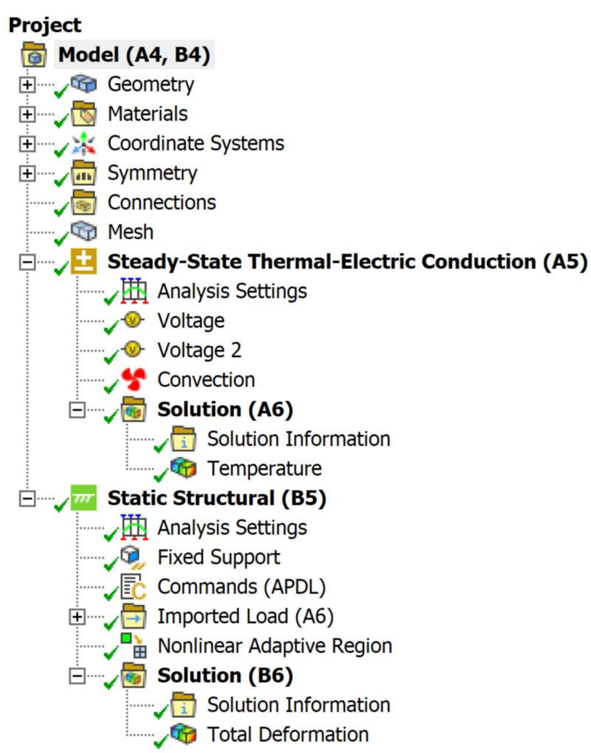

Figure 6.5 The project hierarchy of the simulation work.

We used two techniques to overcome the convergence difficulties. The first technique is nonlinear adaptive region, which commands ANSYS to automatically remesh the model or a portion of the model when elements become excessively distorted. The second technique is semi-implicit method, which enables ANSYS to switch to the semi-implicit solving scheme if the default implicit solver is having trouble. Like a traditional explicit solver, the semi-implicit method can better handle very large deformation. By adopting these two techniques, the force and displacement are able to converge even under large deformation.

6.3 Simulation Results

Based on the CAD model and simulation environment configurations, we have obtained the thermal analysis and deformation analysis of an actuator at 1 V, 2 V, and 3 V as shown in

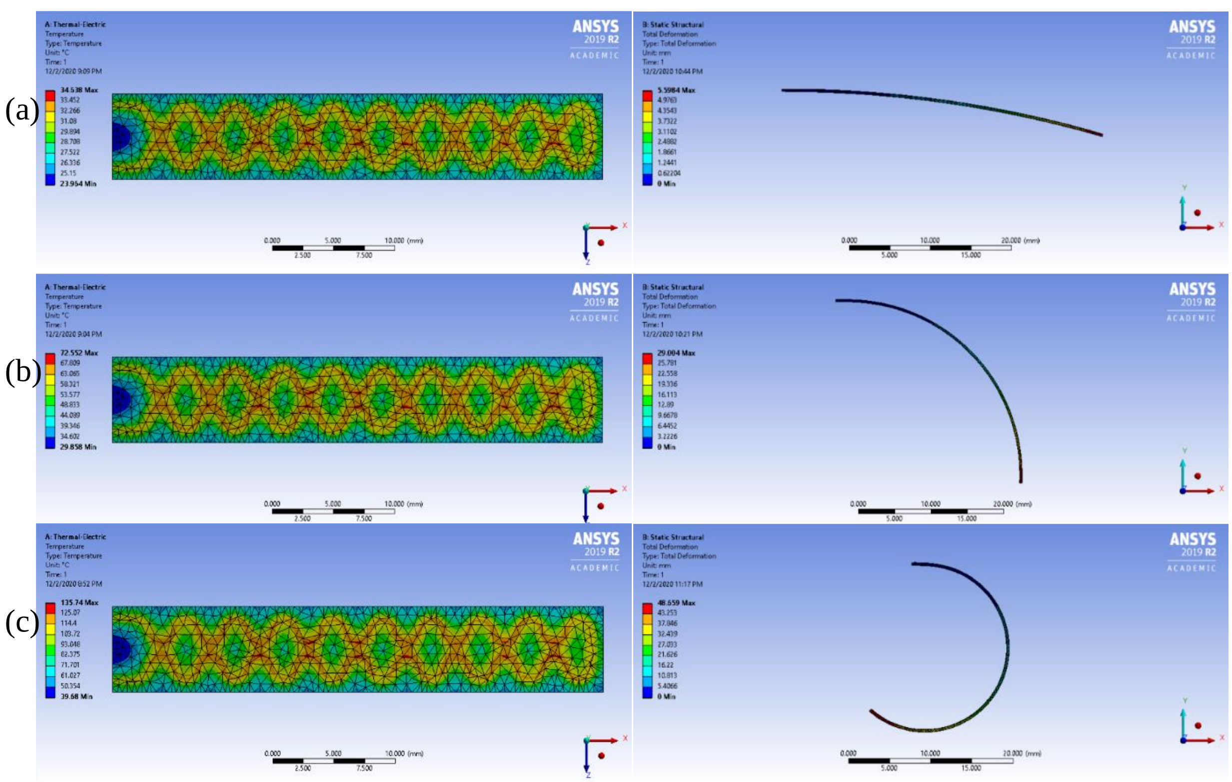

Figure 6.6 The thermal analysis and deformation analysis results when the supply voltage is (a) 1 V; (b) 2 V; and (c) 3 V.

Figure 6.6. As it can be seen from the temperature distribution diagrams, the heater filaments have an evidently higher temperature, but the rest of the actuator generally has a uniform temperature distribution. As the supply voltage increases, the actuator exhibits a larger but uniform bending curvature. In Chapter 7, FEA simulation of thermal analysis and deformation analysis are compared with experimental results in different deformation modes.

6.4 Chapter Summary

This chapter presents the procedure to conduct FEA simulation for the soft electrothermal actuator. The CAD model and engineering data are provided. The meshing process and environment configurations are explained. To overcome convergence difficulties, nonlinear adaptive region and semi-implicit solving techniques are used. Finally, the thermal analysis and deformation analysis results at different supply voltages are obtained.

CHAPTER 7: PROGRAMMABLE DEFORMATIONS OF THE ELECTROTHERMAL ACTUATOR

7.1 Introduction to Programmable Deformations of Soft Actuators

In recent years, there has been an increasing interest in the research of soft actuators that exhibit complex programmable deformations. Programmable deformations of soft actuators can be realized in various ways. The first method is through gradient or patterned actuation. Instead of applying a uniform actuation, a gradient of the actuation effect is created on the actuator. For example, the heat absorption ability of photothermal actuators can be regulated by the amount of light-absorbing materials. Chen et al. [190] fabricated a photothermal actuator whose light absorbing layer was toner-coated paper. The amount of black toner (grayscale) printed on the paper can control the absorption ability of light, leading to different temperature and bending curvature of the actuator. Similarly, for chemically responsive actuators that base on the swelling difference between the two structural layers, programmed deformation can be obtained by distributing the relative amount of those two materials. Jeong et al. [191] reported a chemically responsive soft actuator that is triggered by the unbalanced expansion between the two structural layers when immersed in hexane solvent. While a traditional cantilever structure results in bending deformation, an asymmetrical arrangement of two materials on the cross-section of the cantilever results in twisting deformation. Lahikainen et al. [192] realized the patterned deformation of a photo actuator through synergistic use of photochemical and photothermal effects. The photochemical effect is used for patterning the actuator, and the photothermal effect is used for triggering actuation. With mask patterned ultraviolet exposure, the azobenzene crosslinks in the actuator undergo trans-cis isomerization, which leads to patterned bending deformation under red light irradiation. Ma et al. [193] fabricated a moisture-responsive graphene actuator that has programmable shape-changing capability by patterning its SU-8 layer through ultraviolet lithography. By controlling the geometries and orientations of the SU-8 micropattern arrays, the actuator can achieve complex deformations, including bending, twisting, coiling, etc.

Another way for soft actuators to realize complex programmable deformations is by controlling their deformation direction. This is especially true for twisting deformation, as twisting deformation can be obtained from a bending that is misaligned to the long axis of the actuator. For soft pneumatic network actuators, this can be done by orienting the air chambers by an angle from the longitudinal direction [184]. Some photo responsive materials exhibit uniaxial deformation or have a dominant deformation direction. For example, Hu et al. [194] reported a photo actuator which was fabricated by compositing a photo-liquefiable azobenzene derivative with polyethylene film. Guided rubbing and annealing treatments were subsequently applied to the composite film. Actuators obtained by cutting along the rubbing direction exhibited only bending deformation, while actuators obtained by cutting at an angle with the rubbing direction exhibited helical twisting. Wang et al. [186] developed a dual-layer liquid crystal soft actuator that can bend under ultraviolet irradiation and twist under near-infrared irradiation. The top layer possesses a uniaxially aligned liquid crystalline elastomer matrix incorporated with azobenzene chromophores and a near-infrared absorbing dye, so it bends under ultraviolet stimulus and shrinks under near-infrared stimulus. The bottom layer has only near-infrared dye, and only responds to near-infrared stimulus. Because the shrinkage directions of the top and bottom layer are tilted to each other, the actuator executes twisting deformation under near-infrared irradiation. For magnetic soft actuators, programmable deformation can be achieved by rearranging the magnetization patterns and directions. Song et al. [195] fabricated a soft magnetic actuator that was composed of spatially separated magnetic microspheres encapsulated in oligomeric polyethylene glycol. Solid-to-liquid phase transition of this encapsulating oligomer allows rearrangement of the magnetization directions in the magnetic microspheres. At a lower temperature, the magnetization directions of the magnetic microspheres are fixed, while at a higher temperature, the magnetization directions can be rearranged to any desired form under external magnetic fields. Besides, humidity responsive actuators based on uniaxially aligned liquid crystal polymer network [187] and thermal responsive hydrogel fibrous membranes showing directionally controlled movements [196] were also reported.

Programmable deformation of soft actuators can also be achieved by mechanical anisotropy. For an actuator strip, its bending deformation tends to occur along the direction that has the lowest bending stiffness. If that direction is misaligned with the transverse direction, a twisting deformation will be produced in addition to the bending deformation. Bending stiffness patterns are commonly altered by reinforcements like reinforcing stripes, fibers, and wires. For example, Schaffner et al. [197] reported a 3D printed pneumatic soft actuator that can bend, contract, twist, and grab by designing the tube shape and configuring its reinforcing stripes. Wang et al. [198] designed a thermal responsive soft actuator that exhibits coupled bending and twisting deformation, which comes from its structure anisotropy induced by the embedded shape memory polymer fibers in a homogeneous elastic matrix. Similarly, Song et al. [183] developed a shape memory alloy actuator that can achieve coupled bending-twisting actuation by embedding an anisotropic layered reinforcement structure.

Programmable deformation of soft electrothermal actuators is challenging, mainly restricted by the free-form fabrication capabilities of the resistive heater. Most soft electrothermal actuators reported so far utilize the deposition (e.g., spin-coating [199], casting [200], filtration [201], spray [10]) of nanomaterial-based solution to form a thin conductive heater layer with only uniform heating capability, which is difficult to provide customized actuation and temperature distributions. Unlike these previously reported soft electrothermal actuators, in this work, the custom programmed heater is fabricated in the actuator, which is directly printed with pre-designed patterns using the EHD printing technology. The direct fabrication capabilities from EHD printing enables free-form design of the embedded heater, which can easily control the heated area and the temperature distribution, leading to complex programmable deformations like uniform bending, customized bending, folding, and twisting. To the best of our knowledge, this is the first soft electrothermal actuator reported to have achieved programmable bending and twisting deformations.

7.2 Design Concept of the Programmable Electrothermal Actuator

Figure 7.1 shows the design concept of the programmable electrothermal actuator, which can realize four different modes of deformation: uniform bending, customized bending, folding, and twisting, by customizing the heater design and the resulting temperature distribution. In Figure 7.1 (a), the heater is printed to cover the actuator uniformly by a zigzag pattern with equal line spacing. When a voltage is applied, it generates an evenly heated area that leads to uniform bending. Figure 7.1 (b) shows a heater pattern whose line spacing is reduced from left to right. This heater design generates a gradient heating area, and the resulting temperature field gradually increases from left to right, which results in bending deformation with customized curvature. By localized heating, folding deformation as in the traditional rotary joint can be obtained, as shown in Figure 7.1 (c), since the polymeric structural materials are not good heat conductors. Furthermore, the heater filaments can also be custom printed along a direction that has an angle with the transverse direction as shown in Figure 7.1 (d). This oblique heater design not only creates a skewed parallelogram high temperature zone, but also changes the stiffness anisotropy of the heater. The actuator tends to bend along the direction of the temperature field with lower bending stiffness, which is now parallel to the oblique heater filaments. This skewed bending is actually a coupled bending and twisting deformation.

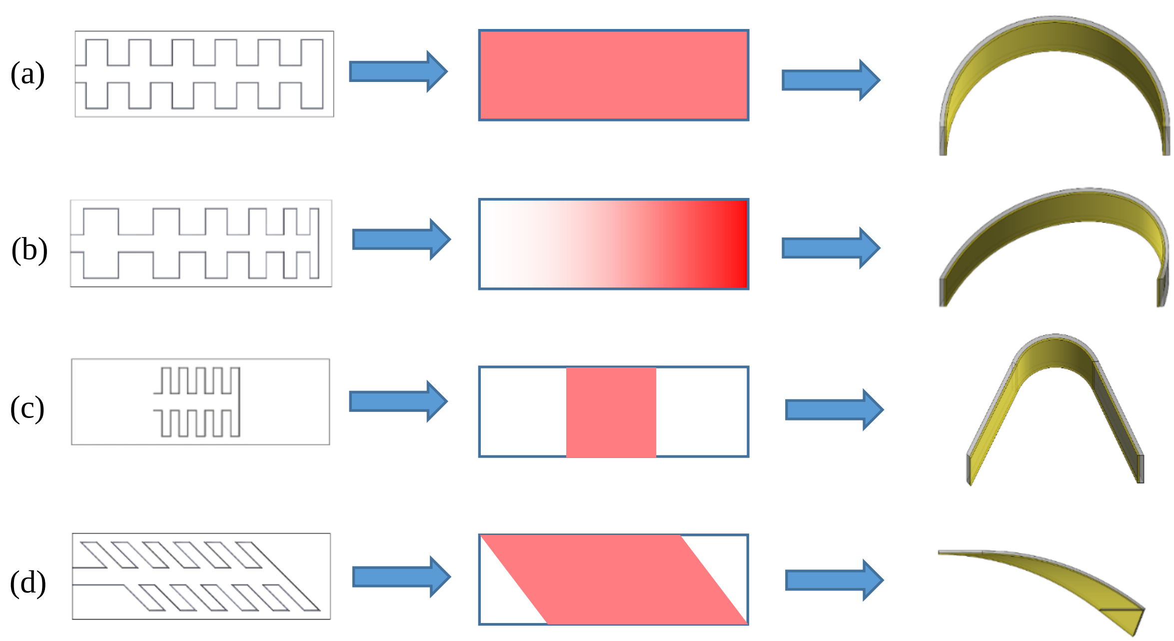

Figure 7.1 Schematic design of programable actuators with different heater patterns, temperature distribution on the actuator when supplied with voltage, and the corresponding deformation for (a) uniform bending, (b) customized bending, (c) folding, and (d) twisting.

7.3 Uniform Bending

Uniform bending of the actuator can be achieved when the embedded heater is uniformly patterned on the actuator, as shown in Figure 7.2 (a). When an actuation voltage is applied, a roughly uniform temperature distribution is obtained for the actuator as shown in the thermography of Figure 7.2 (b). Since for the electrothermal actuator, the bending curvature is proportional to the temperature increasement, uniform temperature distribution results in a constant bending curvature and bending radius. Figure 7.2 (c) shows the

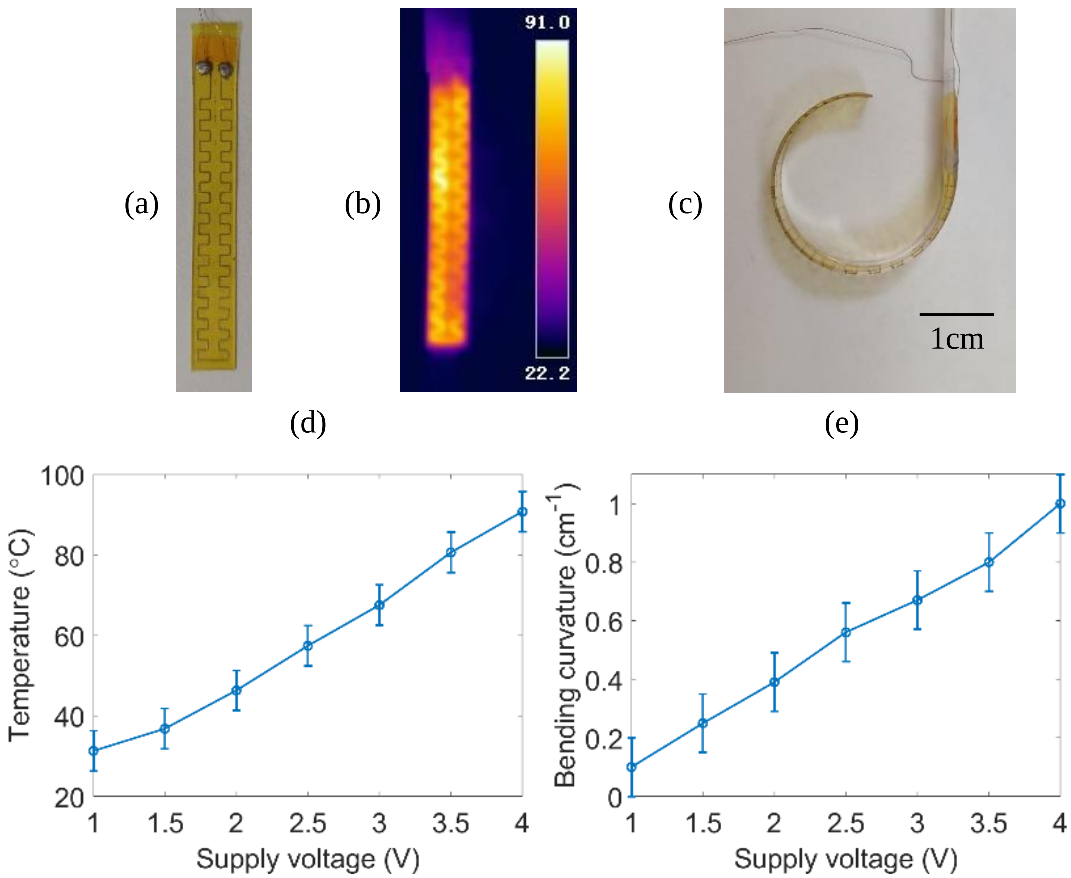

Figure 7.2 Uniform bending. (a) The fabricated actuator and heater pattern; (b) Thermography of an actuated actuator; (c) Uniform bending deformation of an actuator; (d) The stable average temperature achieved at different actuation voltages; (e) The bending curvature at different voltages.

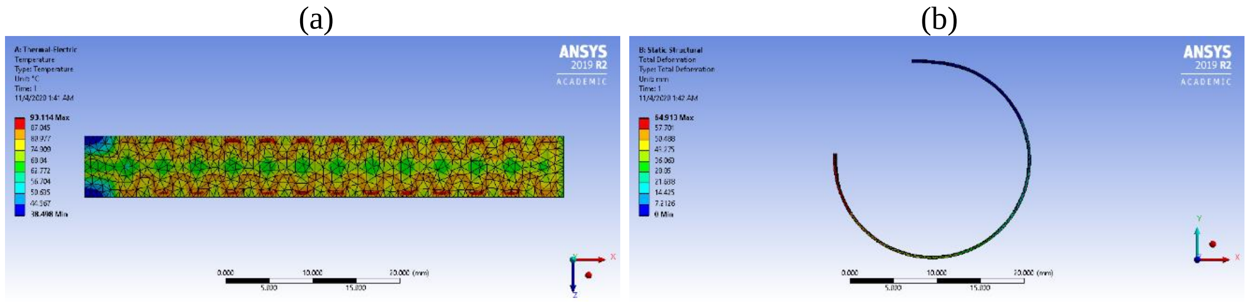

Figure 7.3 FEA simulation of uniform bending. (a) FEA simulation of the temperature distribution by thermal analysis; (b) Deformation of the actuator from FEA analysis.

actuator's bending profile when the supply voltage is 3.5 V, in which a circular bending deformation is achieved with a constant radius. The bending curvature of the actuator can be easily controlled by the actuation voltage and the resulting heating temperature, and the bending curvature generally follows a linear relationship with the temperature change from the Equation 3.1 and was demonstrated in Chapter 3. Figure 7.2 (d) and (e) show the actuator's stable average temperature and bending curvature at different voltages, respectively. In both diagrams, a linear trend can be clearly observed. Moreover, an electric-thermal-mechanical finite element model was developed to study the temperature distribution and the deformation of the actuator and to verify each specific heater design. The FEA simulation results from the corresponding thermal analysis and deformation analysis, as shown in Figure 7.3 (a) and (b), agree well with the experimental results.

7.4 Customized Bending

The direct fabrication capabilities of EHD printing enables the free-form customized design of the embedded heater, which makes it possible to program the temperature distribution on the actuator, such as a temperature gradient. Since the electric current is equal along the heater filament, in a unit area on the actuator, the heater filament length directly determines the heating power in that area, which in turn affects its temperature. Theoretically, the temperature in an area can be controlled by designating the heater filament length in it. This is the idea to realize customized bending, which is shown in Figure 7.4 (a). On an L length actuator strip (indicated by each dashed red box), it is possible to place different numbers of paired tooth shape heater filament fractions. In Figure 7.4 (a), they are 0, 1, 2 and 3, from left to right. All the toothed heater fractions have the same height H, but different widths. Their widths are determined by evenly distributing them within the designated area. We use P_d to denote the heating power on an L length actuator strip:

$$P = I^2 R = (2L + 4nH)\rho I^2 \tag{7.1}$$

in which P is the Joule heating power in that area, I is the electric current, R is electrical resistance of the heater filament fractions, ρ is the coefficient of electrical resistivity per unit length, n is the number of paired heater tooth fractions.

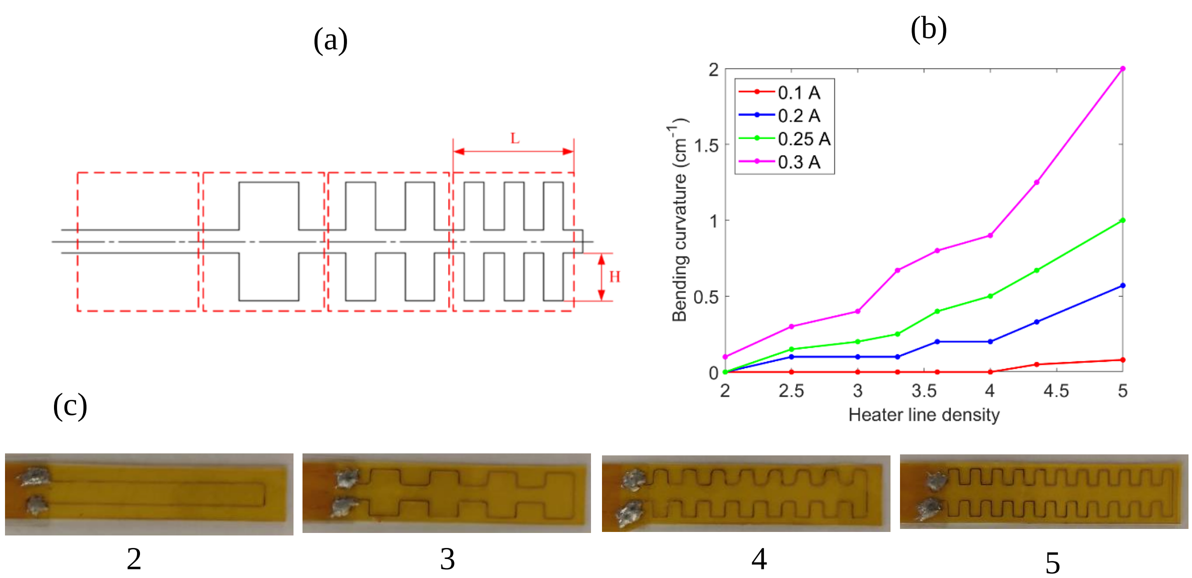

Figure 7.4 (a) Design idea of customized bending. (b) The relationship between heater line density and bending curvature at different electric currents. (c) Heater patterns with different heater line density.

At a certain electric current, ρI^2 is considered to be the same anywhere along the whole heater. The heating power in an area is directly related to the term $2L+4nH$, i.e. the heater filament length. The area with longer heater filament has a higher heating power, can reach a higher temperature, and bends to a larger bending curvature. Here we define a term heater line density D_L to measure the length of the heater filament in a unit area.

$$D_L = \frac{2L+4nH}{L} = 2+4n\frac{H}{L} \tag{7.2}$$

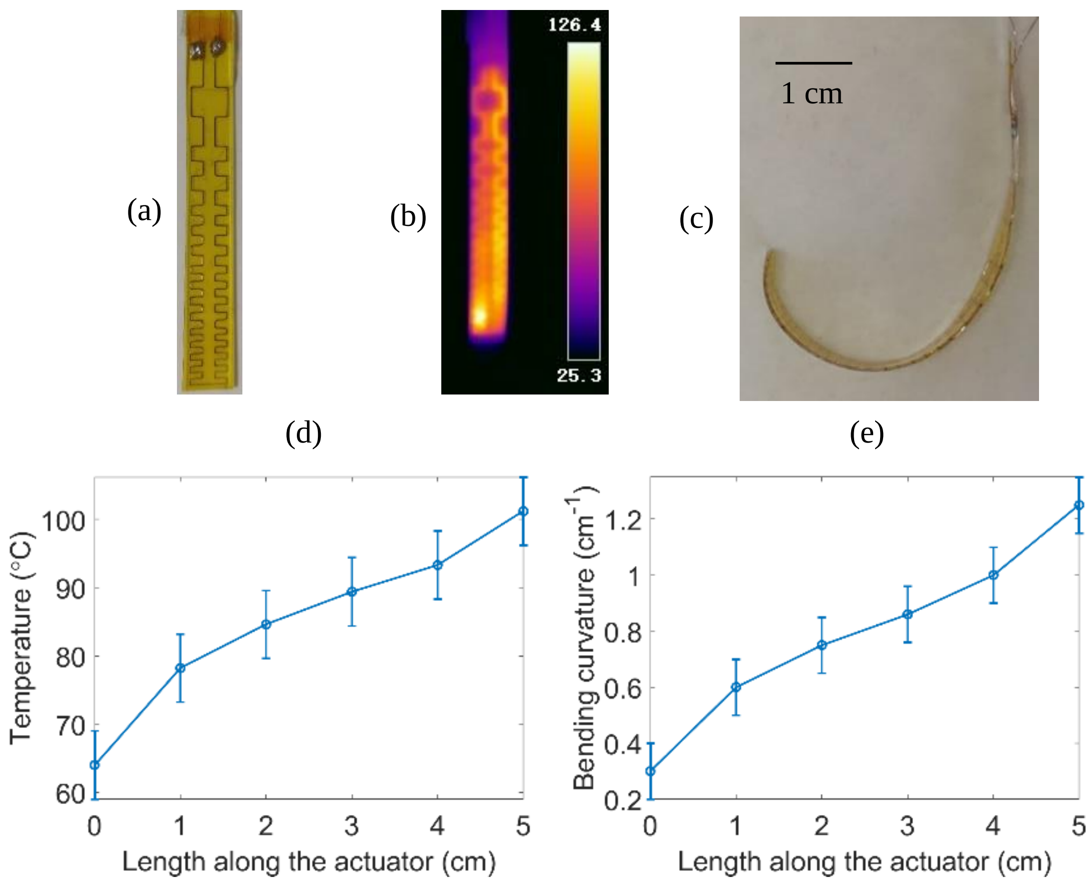

Figure 7.5 Customized bending. (a) The fabricated actuator and heater pattern; (b) Thermography of an actuated actuator; (c) Customized bending deformation; (d) The average temperature at different locations along the actuator; (e) The bending curvature at different locations along the actuator.

In fact, H and L are fixed in our study, so D_L can be varied by changing n. We fabricated a series of actuators whose heater line densities range from 2 to 5 as shown in Figure 7.4 (c). Their bending curvatures at different electric currents were measured. As shown in Figure 7.4 (b), at 0.2 A, 0.25 A and 0.3 A, their bending curvatures can vary from 0 to 0.57 cm^{-1}, 0 to 1 cm^{-1}, and 0.1 to 2 cm^{-1}.

In Figure 7.5, a soft actuator with a continuous change of the temperature field and the resulting programmed bending curvature was fabricated and tested. The line spacing of the heater filaments decreases and the heater filament density increases from top to bottom. Because of the equal electric current flowing through the heater filament and the almost uniform diameter of the heater filament, the area density of the heating power is determined by the area density of the heater filament. Due to the changing line spacing, the area on the actuator with narrower line spacing has a denser heater filament distribution, and naturally a higher average temperature (as shown in Figure 7.5 (b)) and a larger bending curvature. Figure 7.5 (c) shows the actuator's profile when a 4 V voltage is applied. The average temperature and bending curvature at different locations along the actuator from top to bottom were measured and shown in Figure 7.5 (d) and Figure 7.5 (e), respectively. Clearly

(a) (b)

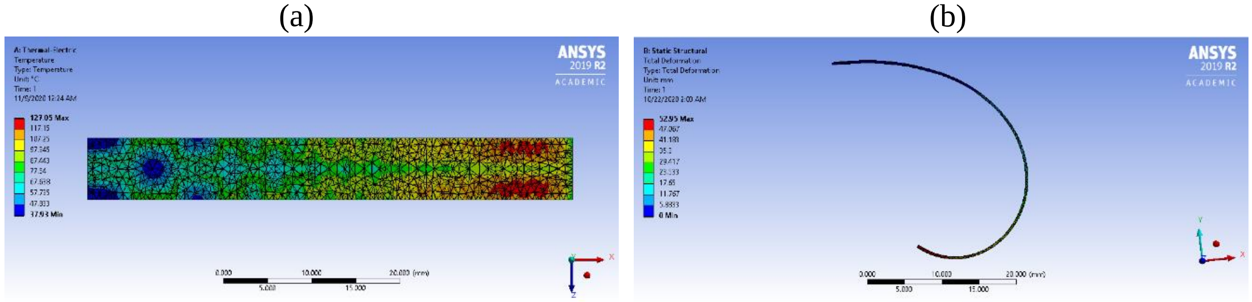

Figure 7.6 FEA simulation of customized bending. (a) FEA simulation of the temperature distribution by thermal analysis; (b) Deformation of the actuator from FEA analysis.

a temperature gradient can be observed on the actuator because of the different density in the heating filament. A gradually changing bending curvature can also be observed, which follows the same trend with the temperature gradient on the actuator. With the assistance of the FEA model and the experimental data, it is possible to design and fabricate an actuator that can bend to a customized bending profile. The FEA simulation results on the temperature distribution on the actuator and the corresponding actuator deformation are shown in Figure 7.6 (a) and (b). The deformation profile of the actuator from FEA is very close to that from the experimental result in Figure 7.5 (c).

7.5 Folding

Folding provides localized bending that is similar to the traditional rotary joint. Folding enables kinematically precise rotary degree-of-freedom for mechanism design in soft robotics. Another widely studied application of soft actuators is their abilities to form customized structures by folding of 2D sheets. The folding can be realized by locally heating the actuator to an enough extent. As shown in Figure 7.7 (a), on an actuator strip, only the middle area is printed with heater filaments. As shown in Figure 7.7 (b), when the middle area is heated to a certain bending curvature, the folding angle can be calculated by the following formula:

$$\theta = \frac{L}{R} = L\kappa \tag{7.3}$$

in which θ is the folding angle, L is length of the localized heating area, R and κ are the bending radius and curvature, respectively. Therefore, the folding angle can be controlled by either the actuator length or the bending curvature which can be regulated by the supplied actuation voltage.

Figure 7.7 (c) shows its thermography of the actuator at a voltage of 3 V. As it can be observed from the thermal image, the actuator has a locally heated area, since the structural materials both have relatively low thermal conductivity. Figure 7.7 (d) shows the

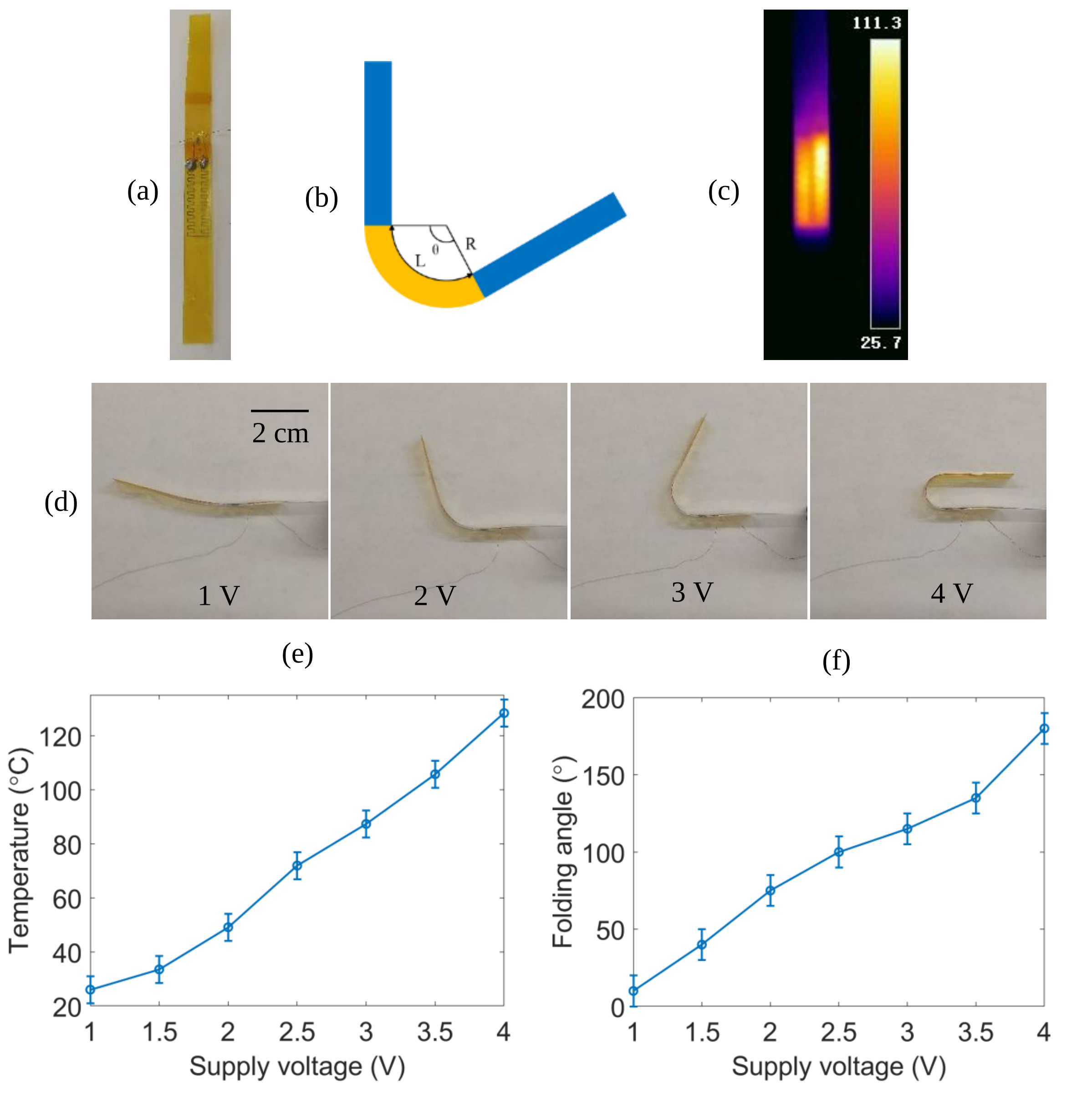

Figure 7.7 Folding. (a) The fabricated actuator and heater pattern; (b) Schematic of the folding structure; (c) Thermography of an actuated actuator; (d) Folding deformation of the actuator under different voltages; (e) The average temperature on the folding joint at different voltages; (f) The folding angle achieved at different voltages.

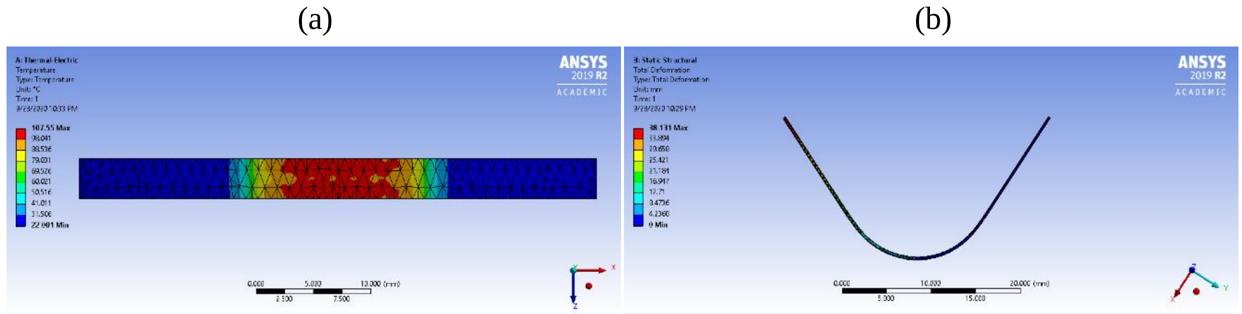

Figure 7.8 FEA simulation of folding. (a) Temperature distribution by FEA thermal analysis; (b) Deformation of the actuator from FEA analysis.

folding deformation of the actuator at different voltages. The relationship of the stable average temperature on the folding joint and the folding angle with respect to different actuation voltages are shown in Figure 7.7 (e) and (f), which indicate a rough linear relationship. The folding deformation was also analyzed using FEA tool, as shown in Figure 7.8 (a) and (b), corresponding to the thermal analysis and deformation analysis, which resemble the experimental results.

By configurating multiple actuators together, different structures can be formed in a controlled way by selecting folding joints with different rotary directions. Two folding structures were obtained as shown in Figure 7.9 (a) and (b) from a straight strip under actuation. The folding actuators can be used as folding joints with their folding angles being controlled by the actuation voltage. The actuators are jointed together using connection materials (PI tape and polyethylene terephthalate or PET sheets). In Figure 7.9 (a), both actuators have their PI side faced up. By controlling both folding angles to 120 °, a triangle structure can be obtained. In Figure 7.9 (b), one folding actuator has PDMS side up, and the other has PI side up, thus giving them inverse rotational directions. By controlling both folding angles to 90 ° using the actuation voltage, a Z shape structure can be achieved.

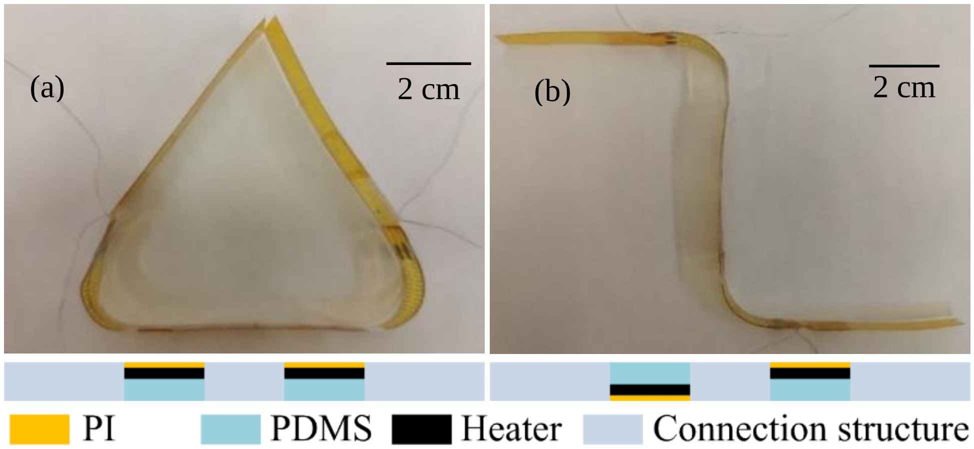

Figure 7.9 Controlled structure formation from actuator strips. (a) A triangle structure; (b) A Z-shape structure.

7.6 Twisting

Twisting deformation of the electrothermal actuator can be realized by printing a skewed heater pattern as shown in Figure 7.10 (a). This oblique heater can not only generate a parallelogram high-temperature zone as shown in Figure 7.10 (b), but also changes the stiffness anisotropy of the actuator. For the uniform bending, the transverse direction has the lowest bending stiffness. While for the skewed heater pattern, the heating area and the direction with the lowest bending stiffness shifts to be parallel to the skewed heater filaments. The actuator tends to bend along this oblique direction, resulting in a coupled bending and twisting deformation as shown in Figure 7.10 (c) with the voltage applied of 2.5 V. We have measured the stable average temperature on the actuator and the twisting angle at different actuation voltages, as shown in Figure 7.10 (d) and Figure 7.10 (e), respectively. Linear relationship is observed between the actuation voltage and the resulting twisting angle from the actuator. Figure 7.11 (a) and (b) show the FEA simulation results for thermal analysis and deformation analysis, which agree very well with the experimental results.

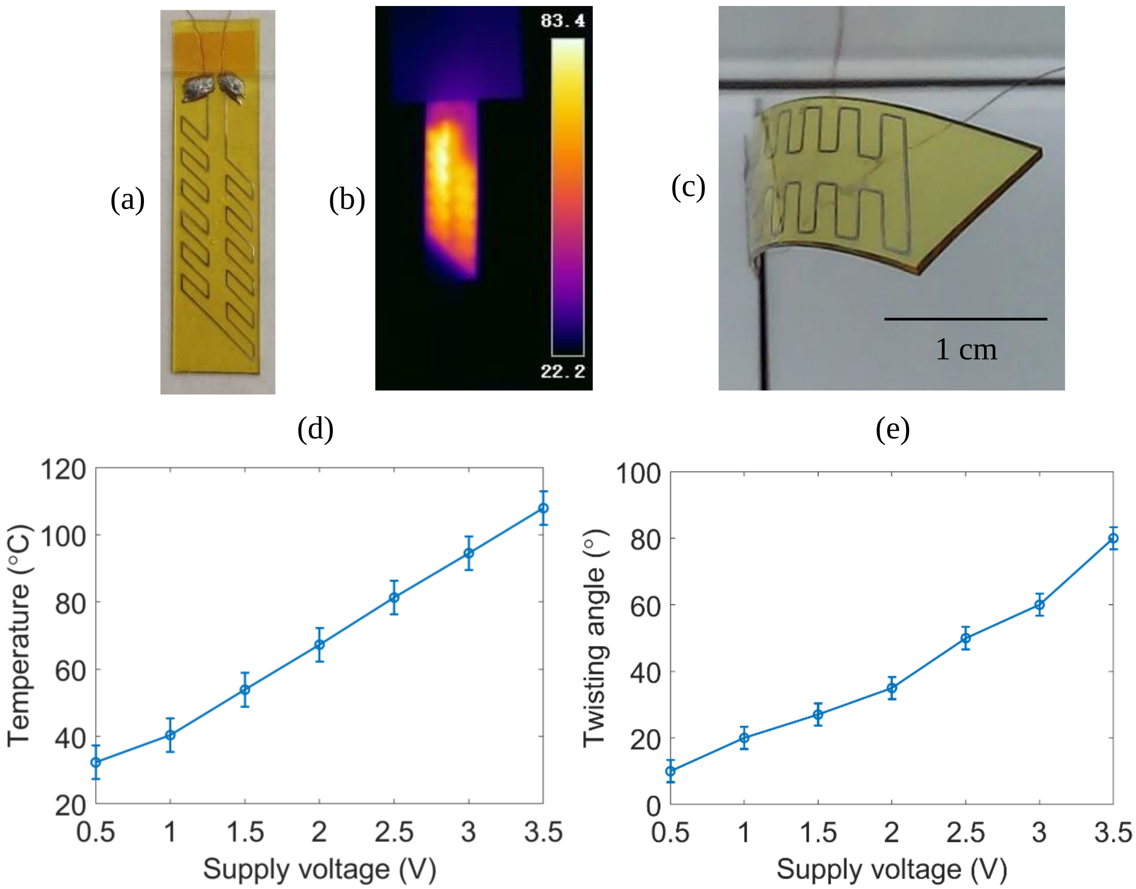

Figure 7.10 Twisting. (a) The fabricated actuator and heater pattern; (b) Thermography of an actuated actuator; (c) Twisting deformation form the actuator; (d) The average temperature achieved at different voltages; (e) The twisting angle at different voltages.

7.7 Chapter Summary

This chapter presents the idea and design concept to realize complex programmable deformations of the soft electrothermal actuators. By changing the design pattern of the embedded heater, different temperature distributions can be created, which lead to various programmable deformations, including uniform bending, customized bending, folding, and twisting. These deformation modes are characterized on their heating and deformation performance at different supply voltages. Finally, FEA simulation results of thermal analysis and deformation analysis are provided to validate the design concept.

(a) (b)

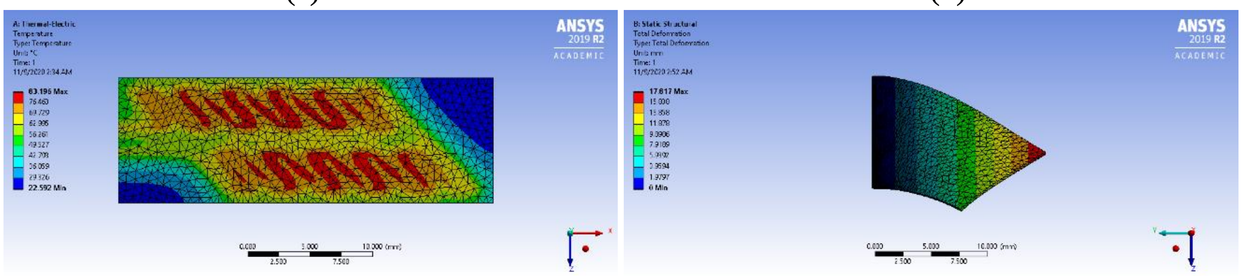

Figure 7.11 FEA simulation of twisting. (a) Temperature distribution by FEA thermal analysis; (b) Deformation of the actuator from FEA analysis.

CHAPTER 8: APPLICATIONS OF THE ELECTROTHERMAL ACTUATOR

8.1 Application as a Soft Lifter

The soft actuators have many potential applications such as in soft robotics and micro assembly. In this work, we studied four typical applications of the soft actuator, as a soft lifter, soft gripper, soft robot arm, and walking robots. To evaluate the actuation force from the soft electrothermal actuator, we tested the soft actuator in the lifting tasks. When being used as a lifter, the soft actuators generally can lift samples that are much heavier than the actuator itself. To test the lifting capability of the actuator, the fabricated soft actuator was placed horizontally, with one end fixed and the other end free (as shown in Figure 8.1 (a)). At the unactuated state, the actuator bent downwards slightly due to the gravity force from its own weight (about 0.1 g). After loading a few staples as the sample, the free end of the actuator bent down further because of the extra weight from the loaded sample, as shown in Figure 8.1 (b). Then when the actuator was actuated by supplying a 0.3 A current (voltage is about 3 V), the actuator bent upwards rapidly, and eventually lifted the samples back to the actuator's original position (Figure 8.1 (c)). The actuation

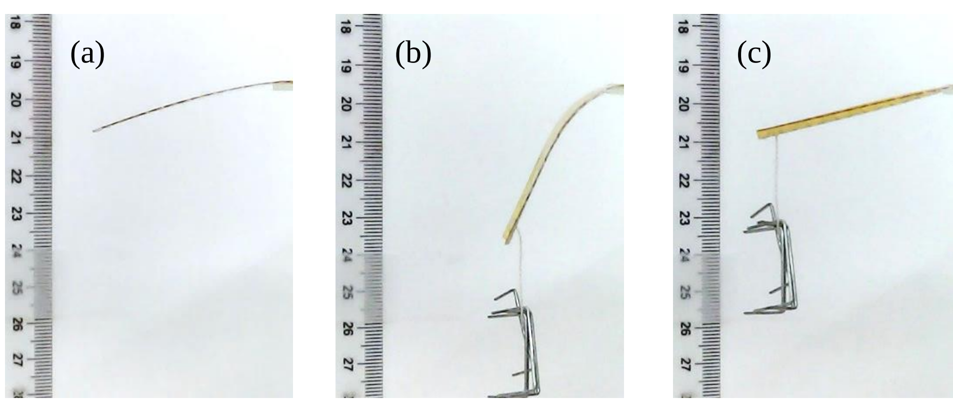

Figure 8.1 Demonstration of the soft actuator as a soft lifter. (a) Unactuated lifter without load. (b) Loading samples further deforms the soft lifter. (c) Actuated lifter lifts the sample back to the initial location.

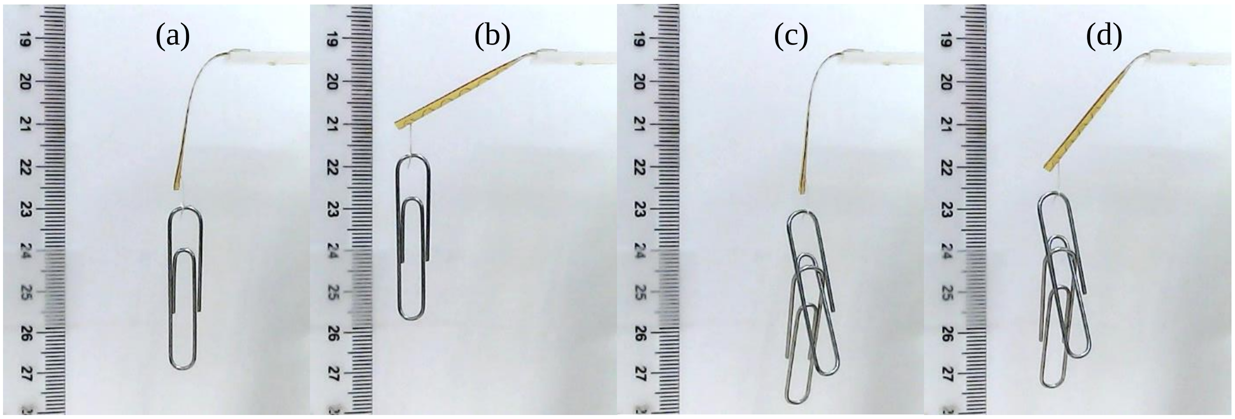

Figure 8.2 Demonstration of the soft lifter with heavier loads. (a) 0.4 g load unactuated. (b) 0.4 g load actuated. (c) 0.8 g load unactuated. (d) 0.8 g load actuated.

force from the electrothermal actuator fully compensated the gravity force from the loaded samples. In this work, the samples we used were office staples with a unit weight of 0.033 g. The actuator can lift up to six staples with a total weight of 0.2 g back to its initial position, which indicates the maximum actuation force roughly about 2 mN. The soft actuator has full capability to lift weight twice of its own weight, with a lifting height about 30 mm.

We have also tested the actuator's lifting capability using heavier loads. Under a 4 V supply voltage, the actuator can lift 0.4 g paper clip up for more than 15 mm (as shown in Figure 8.2 (a) and (b)). For a 0.8g load, the actuator can lift it up for 5 mm (Figure 8.2 (c) and (d)). The loading capability (i.e. output force) of the soft actuator can be improved by designing the bimorph structure with larger stiffness, such as increasing the thickness and width of the actuator, and/or by increasing the actuation power and actuator temperature.

8.2 Application as a Soft Gripper

Soft actuators have been explored as soft grippers, due to their large deformation and gentle interaction with the objects. A four-finger soft gripper was designed and fabricated by arranging four electrothermal actuators together and connecting them in a series circuit (shown in Figure 8.3). When the power was applied to the actuators, each actuator/finger bent inside towards each other and the four fingers moved closer for picking objects. When the actuation current was turned off, the four fingers moved apart from each other and effectively released the grabbed object. The grabbing and releasing or pick-and-place operation of the soft gripper imitated the operation of a human hand. The soft gripper was mounted on a motion stage, which has three moving axes to implement the automated pick-and-place operations of the gripper. A foam block was used as the gripping sample to mimic a delicate object, and two Petri dishes served as the pick and place stations. Figure 8.3 shows the gripper manipulated a delicate object (a green foam block) in the pick-and-place process. At the beginning, the gripper was moved above the object and then approached to the object by the stage motion (Figure 8.3 (a, b)). Then an actuation current was supplied to the gripper, and the four fingers started to close and were able to grasp the object securely (Figure 8.3 (c)). The gripper was then lifted up by the stage (Figure 8.3 (d)) and moved from the picking station to the place station (Figure 8.3 (e)). When the gripper reached the center

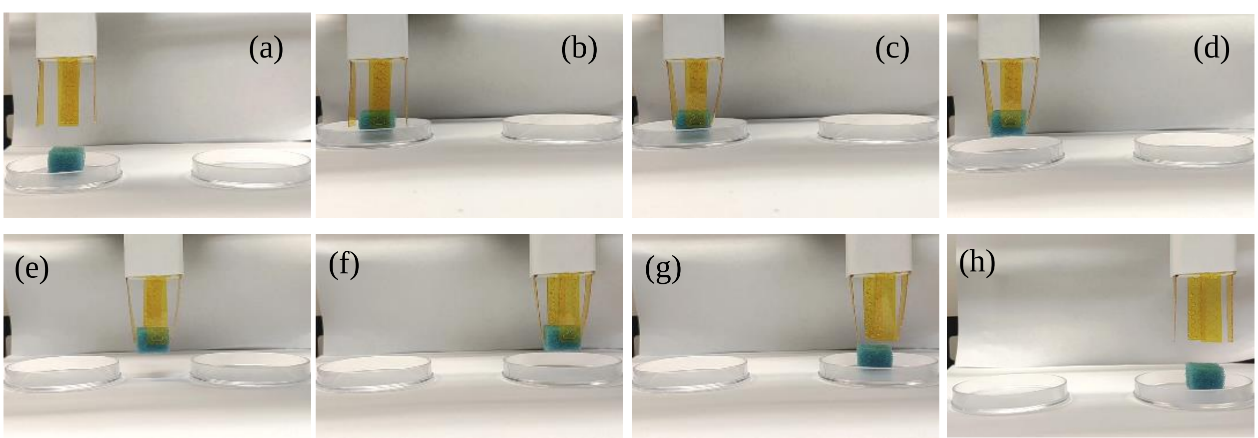

Figure 8.3 Four soft actuators were integrated as a four-finger soft gripper and consecutively captured images showing the pick-and-place operation. (a, b) approaching, (c) grasping, (d) lifting, (e, f) transferring, and (g, h) releasing.

of the place station (Figure 8.3 (f)), the actuation current was turned off. The fingers began to open, and the object was released from the fingers and placed down (Figure 8.3 (g, h)). As demonstrated, this gripper can realize humanoid motion without any additional mechanical components. It can be used as robotic "hand" to transport fragile or delicate objects that cannot be handled by the conventional rigid manipulators.

8.3 Application as a Soft Robot Arm

Our programmable actuators have been realized to achieve different types of motion. Actuators can be put together and utilized to realize a multi-degree-of-freedom soft robot arm as shown in Figure 8.4. Two actuators (one bending actuator and one twisting actuator) were connected to mimic a soft robot arm, which has two degree-of-freedom: lifting motion and twisting motion. When the bending actuator is powered on, it lifts the structure up (as shown from Figure 8.4 (a) to (b)). When the twisting actuator is powered on, the arm tip twists (as shown from Figure 8.4 (b) to (c)). These two motions can be controlled independently or collaboratively with lifting distance and twisting angle being controlled separately.

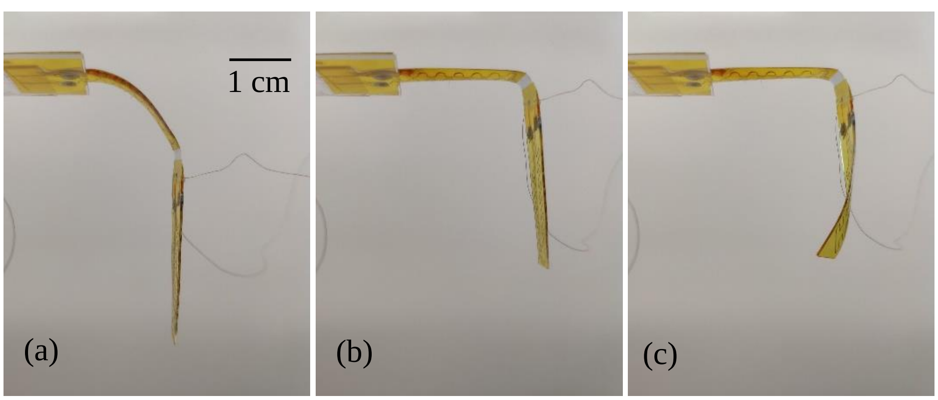

Figure 8.4 A two-degree-of-freedom soft robot arm. (a) At unactuated state, (b) Lifting applied, (c) Twisting applied.

8.4 Application as Soft Walking Robots

Self-walking is the basic motions of robots. Unlike the complex electromechanical system in conventional rigid walking robots, soft actuators can walk using the biomimetic worm-like crawling motion. We developed a prototype soft walking robot using a single electrothermal actuator, as shown in Figure 8.5. A relatively rigid copper tape was attached to the middle of the actuator strip to form a local curve, which facilitates the contraction and relaxation motions of the actuator. A ratchet walking surface was prepared by stacking a pile of paper cards. This asymmetrical ratchet structure allows the soft robot to proceed one-directional walking motion when supplied with periodic pulses of voltage signal. We used a 40 s periodic voltage signal (20 s ON and 20 s OFF, shown in Figure 8.5 (e)) to drive the soft walking robot. Figure 8.5 (a-d) show the profile and position of the soft walker at different time moments. In the contraction stage (voltage was ON), the rear leg slid forward, while the front leg was mostly restricted from sliding backward by the ratchet structure

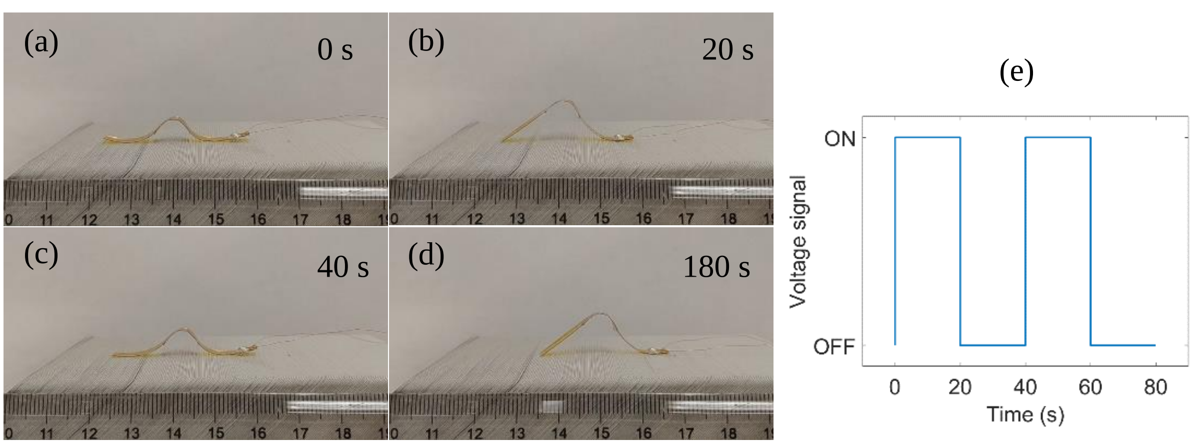

Figure 8.5 Demonstration of the electrothermal actuator as a soft walker on a ratchet surface. (a-d) Successive profiles of the soft walker crawling on the ratchet surface. (e) Voltage signal of the soft walker.

(from 0 to 20 s). Similarly, in the relaxation stage (voltage was OFF), the front leg slid forward while the rear leg was kept at the same position by the ratchet face (from 20 to 40 s). The repeated contraction and relaxation motions of the actuator can be converted into forward walking. In 3 minutes, it moved forward to right by 15 mm (shown in 180 s), indicating a walking velocity about 5 mm/min.

The soft walker on the ratchet surface only provides one-directional walking motion. Integrating flexibly fabricated programable actuators, we further developed a soft walker that can walk both forward and backward directions on a flat surface. As shown in Figure 8.6, instead of using a single actuator, this soft walker is consisted of two actuators linked

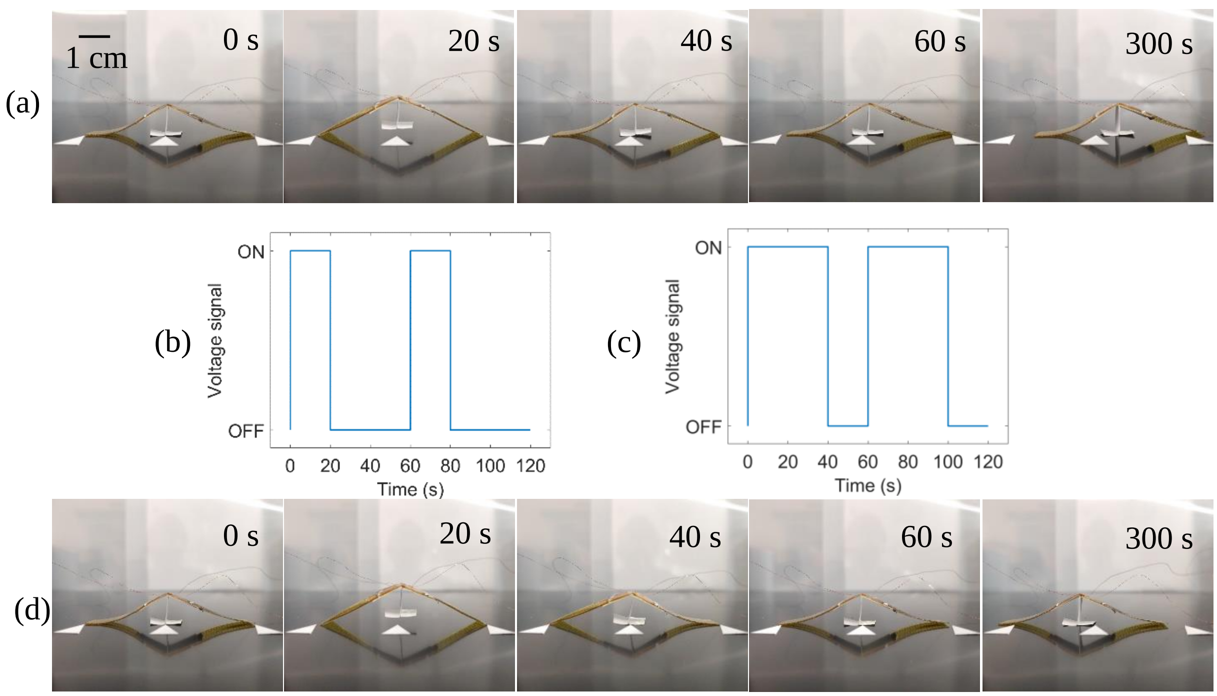

Figure 8.6 Demonstration of the electrothermal actuator as a bidirectional soft walker. (a) Successive profiles of the bidirectional soft walker proceeding to right; (b) Voltage signal of the bidirectional soft walker – left actuator; (c) Voltage signal of the bidirectional soft walker – right actuator; (d) Successive profiles of the bidirectional soft walker proceeding to left.

together but functioning independently. Moreover, a foot in the middle of the soft walker was used as a support. The soft walker was placed on a table surface and three markers were used to denote the initial positions of the two actuator tips as well as the middle foot. By controlling the commands on the two actuators, bi-directional walking motion can be achieved. For one walk cycle, at the beginning, when both actuators were actuated, the two actuators contracted inward and lifted the middle foot up (from 0 to 20 s). At the next step, the voltage for the left actuator was first cut off. The left actuator bent downward and pushed the middle foot rightward slightly (from 20 to 40 s). Then, the voltage for the right actuator was cut off, and the whole structure moved a step toward right (from 40 to 60 s). This gait pattern can be repeated using a periodic pulse. A one-minute cyclic signal (both actuators ON for 20 s, left OFF for 20 s and right OFF for 20 s) was used to control the walking motion. The voltage signals for the left actuator and the right actuator are shown in Figure 8.6 (b) and (c), respectively. After executing 5 full cycles, the soft walker moved to the right about 10 mm, indicating a walking speed about 2 mm/min. By changing the control signals on the two actuators, motion in the other direction can also be achieved. When the voltage signals are changed to that the right actuator is turned off first and then the left actuator is turned off, the soft walker can also walk toward left direction in a similar gait mode (shown in Figure 8.6 (d)).

8.5 Chapter Summary

In this chapter, the soft electrothermal actuators are demonstrated for various biomimetic applications, including a soft lifter, a soft gripper, a soft robot arm, and soft walkers.

CHAPTER 9: RESEARCH SUMMARY AND FUTURE WORK

9.1 Research Summary

In this dissertation, my work has mainly focused on the fabrication, control, and applications of soft electrothermal actuators. A new cost-effective approach is reported to fabricate soft electrothermal actuators using EHD printing. We have studied the self-sensing feedback control of soft electrothermal actuators and designed an innovative control algorithm to compensate the non-linearity of the control system. Assisted by the direct patterning capabilities of EHD printing, we were able to realize programmable deformations of the soft electrothermal actuator. In addition, FEA software ANSYS was successfully implemented for the electrothermal analysis and thermomechanical analysis of the actuator. Lastly, the soft electrothermal actuators were successfully demonstrated for various biomimetic applications.

A new cost-effective method to fabricate soft electrothermal actuators is reported. The structural materials used are PI and PDMS, due to their large difference in CTE. Unlike most other soft electrothermal actuators that use nanomaterial-based solution to deposit a thin conductive film for the heater, our electrothermal actuators have an embedded heater that is directly printed by EHD printing using a very cheap solder Bi58/Sn42. We have studied the printing parameters for Bi58/Sn42, and explored the fabrication process for the electrothermal actuator. The soft electrothermal actuator was modeled as a bimorph structure. Based on that, the heater design and film thickness were optimized for improved bending performance. Lastly, the actuator was characterized by its heating performance and bending performance.

High precision operation of soft actuators is critical while challenging due to the nonlinear and complex relationship between the actuation voltage and the resulting bending curvature. Moreover, open-loop operation of soft electrothermal actuators usually has a long transient time and is susceptible to external environment variations. We have studied the dynamic model of the soft electrothermal actuator, and developed a self-sensing mechanism for the closed-loop control of the electrothermal actuator. Due to the different control characteristics in the heating and cooling stages, a switching PID control algorithm was designed, in which two sets of control parameters are used separately for the heating and cooling processes. The performance of the designed control algorithm was evaluated in setpoint tracking, step response, wave tracking, and disturbance rejection.

Twisting deformation represents another degree-of-freedom for soft actuators, which can be achieved by creating an oblique bending deformation. Assisted by the direct patterning capabilities of EHD printing, we designed a kind of electrothermal actuator that has a skewed heater pattern. This oblique heater can not only generate a parallelogram high-temperature zone, but also changes the stiffness anisotropy of the actuator. For the skewed heater pattern, the heating area and the direction with the lowest bending stiffness shifts to be parallel to the skewed heater filaments. The actuator tends to bend along this oblique direction, resulting in a coupled bending and twisting deformation. We have characterized the actuator's twisting performance at different supply voltages. We also built the theoretical model of the twisting actuator, and studied the influence of design parameters on the twisting angle. Lastly, we studied the displacement and motion trajectory of the actuator's free edge when the temperature or curvature increases.

The direct patterning capabilities of EHD printing enable free-form design of the embedded heater of the actuator. Following a systematic approach to change the heater pattern and the corresponding temperature distribution, we are able to fabricate actuators that exhibit uniform bending, customized bending, folding, and twisting. An evenly printed zigzag heater pattern can create a homogeneously heated area, hence a uniform bending profile. A heater pattern with changing line spacing can create a temperature gradient, thus leading to customized bending. A locally heated area causes regional high temperature zone, which leads to folding deformation. If the heater pattern is printed in a skewed manner, then a twisting deformation can be obtained.

FEA is a powerful tool for multiphysical simulation. Our actuator is a coupled electric-thermal-mechanical system. We used FEA software ANSYS for the simulation work of the electrothermal actuator. The 3D model of the actuator was built in SolidWorks. Two coupled systems, a thermal-electric analysis system and a static structural analysis system, are used for the simulation work. Nonlinear adaptive region and semi-implicit solving techniques are used to overcome the convergence difficulties for the nonlinear large deformation problem. FEA thermal analysis and deformation analysis results are used to validate the design concept in uniform bending, customized bending, folding, and twisting.

Finally, our soft electrothermal actuators are demonstrated for several biomimetic applications. When used a soft lifter, soft actuators are able to lift loads that are much heavier than their own weights. When used a soft gripper, soft actuators can pick-and-place delicate objects. Multiple soft actuators can also be integrated together to realize the function of a soft robot arm. Finally, our soft electrothermal actuators are demonstrated as a soft walker in a ratchet surface, as well as a bidirectional soft walker that can walk on a flat surface.

9.2 Research Contributions

The main contributions of this dissertation to the research of soft electrothermal actuators include:

- A new cost-effective approach to fabricate soft electrothermal actuators. Most soft electrothermal actuators reported so far use nanomaterial-based solution to deposit the conductive heater. We used a very cheap material Bi58/Sn42, whose price is only $0.03/g, while nanomaterials are generally over $100 per gram.

- Studied the feedback control of soft electrothermal actuators. Operation of soft electrothermal actuators is generally slow and inaccurate due to the nonlinear relationship between the bending curvature and supply voltage. We designed an innovative switching PID control algorithm to compensate the nonlinearity in the heating and cooling stages. This switching PID control algorithm can also be used for other nonlinear control systems which have different response characteristics in the position and negative control directions.
- Realized the programmable deformations of the soft electrothermal actuator. The direct patterning capabilities of EHD printing enable free-form design of the embedded heater, and lead to different temperature distributions and hence various modes of deformations, including uniform bending, customized bending, folding, and twisting. To the best of our knowledge, this is the first soft electrothermal actuator reported to exhibit programmable bending and twisting deformations.
- FEA software was successfully utilized for the thermal and deformation analysis of soft electrothermal actuators. Due to its extremely distorted elements and large nonlinearity, the simulation of soft electrothermal actuators is difficult, and has rarely been studied. We successfully used FEA software for the electrothermal and thermomechanical analysis for the soft electrothermal actuators.
- Applied the soft actuators for various biomimetic applications, including a soft lifter, soft grippers, a soft robot arm, and soft walkers.

The research achievements in this dissertation have been published in the following journal papers and conference proceedings:

- Yang Cao, Jingyan Dong. High-performance low-voltage soft electrothermal actuator with directly printed micro-heater. *Sensors and Actuators A: Physical*, 297:111546, 2019.
- Yang Cao, Jingyan Dong. Fabrication and self-sensing control of soft electrothermal actuator. *Procedia Manufacturing*, 48 (2020): 43–48, 2020.
- Yang Cao, Jingyan Dong. Self-sensing and control of soft electrothermal actuator. *IEEE/ASME Transactions on Mechatronics*, doi: 10.1109/TMECH.2020.3009237, 2020.
- Yang Cao, Jingyan Dong. Programmable soft electrothermal actuators based on free-form printing of the embedded heater. *Soft Matter*, 2020 (in revision).

9.3 Future Work

In my future research, I plan to continue focusing on micro-scale manufacturing and high-resolution additive manufacturing, with an emphasis on the fabrication of flexible and stretchable electronics, and soft robotics. Flexible and stretchable electronics are widely used in wearable health devices, human-machine interaction, and other biomedical applications. The biggest challenge is that each component must endure bending and stretching while maintaining conductivity and performance. It demands higher requirements and innovations in both material processing and fabrication methods. My future research will utilize EHD printing and other micro manufacturing technologies to fabricate innovative sensors and energy conversion and storage devices.

Soft robotics are generally a broad area. They can be driven by electricity, magnetic field, heat, chemical, light, or pneumatic pressure. Due to their unique characteristics, soft robotics can be used in biomimetic area (e.g. artificial muscles, flexible grippers) and biomedical area (e.g. surgical assist devices, drug delivery, hand rehabilitation). Different soft robotics are distinctive in scale, deformation range, actuation force, speed, and method, which suggest diverse application potentials. In my doctoral study, I have gained extensive knowledge in this area regarding materials, fabrication methods, and application directions. My future research will focus on soft robotics that have higher versatility, such as more degree-of-freedom and steering capabilities; as well as soft robotics that fulfill demanding requirements, such as fast actuation speed, programmed deformation, large force, aerial/underwater environments, and aim at practical biomedical and biomimetic applications.

REFERENCES

[1] W. J. Zheng, N. An, J. H. Yang, J. X. Zhou, and Y. M. Chen, Tough Al-alginate/poly (N-isopropylacrylamide) hydrogel with tunable LCST for soft robotics, ACS Appl. Mater. Interfaces, vol. 7, no. 3, pp. 1758–1764, 2015.

[2] S. Mura, J. Nicolas, and P. Couvreur, Stimuli-responsive nanocarriers for drug delivery, Nat. Mater., vol. 12, no. 11, pp. 991–1003, 2013.

[3] A. W. Feinberg, A. Feigel, S. S. Shevkoplyas, S. Sheehy, G. M. Whitesides, and K. K. Parker, Muscular thin films for building actuators and powering devices, Science, vol. 317, no. 5843, pp. 1366–1370, 2007.

[4] A. E. Aliev, J. Y. Oh, M. E. Kozlov, A. A. Kuznetsov, S. L. Fang, A. F. Fonseca, R. Ovalle, M. D. Lima, M. H. Haque, Y. N. Gartstein, M. Zhang, A. A. Zakhidov, and R. H. Baughman, Giant-stroke, superelastic carbon nanotube aerogel muscles, Science, vol. 323, no. 5921, pp. 1575–1578, 2009.

[5] L. Hines, K. Petersen, G. Z. Lum, and M. Sitti, Soft actuators for small-scale robotics, Adv. Mater., vol. 29, no. 13, Art. no. 1603483, 2016.

[6] Z. H. Zeng, H. Jin, L. P. Zhang, H. Zhang, Z. Chen, F. Gao, and Z. Zhang, Low-voltage and high-performance electrothermal actuator based on multi-walled carbon nanotube/polymer composites, Carbon, vol. 84, pp. 327–334, 2015.

[7] K. Shirasu, G. Yamamoto, Y. Inoue, T. Ogasawara, Y. Shimamura, and T. Hashida, Development of large-movements and high-force electrothermal bimorph actuators based on aligned carbon nanotube reinforced epoxy composites, Sens. Actuator A-Phys., vol. 267, pp. 455–463, 2017.

[8] L. Z. Chen, C. H. Liu, K. Liu, C. Z. Meng, C. H. Hu, J. P. Wang, and S. S. Fan, High-performance, low-voltage, and easy-operable bending actuator based on aligned carbon nanotube/polymer composites, ACS Nano, vol. 5, no. 3, pp. 1588–1593, 2011.

[9] S. S. Yao, J. X. Cui, Z. Cui, and Y. Zhu, Soft electrothermal actuators using silver nanowire heaters, Nanoscale, vol. 9, no. 11, pp. 3797–3805, 2017.

[10] J. Ahn, Y. Jeong, Z. J. Zhao, S. Hwang, K. Kim, J. Ko, S. Jeon, J. Park, H. Kang, J. H. Jeong, and I. Park, Heterogeneous conductance-based locally shape-morphable soft electrothermal actuator, Adv. Mater. Technol., vol. 5, no. 2, Art. no. 1900997, 2020.

[11] H. W. Fan, K. R. Li, Q. Li, C. Y. Hou, Q. H. Zhang, Y. G. Li, W. S. Jin, and H. Z. Wang, Prepolymerization-assisted fabrication of an ultrathin immobilized layer to realize a semi-embedded wrinkled AgNW network for a smart electrothermal chromatic display and actuator, J. Mater. Chem. C, vol. 5, no. 37, pp. 9778–9785, 2017.

[12] S. E. Zhu, R. Shabani, J. Rho, Y. Kim, B. H. Hong, J. H. Ahn, and H. J. Cho, Graphene-based bimorph microactuators, Nano Lett., vol. 11, no. 3, pp. 977–981, 2011.

[13] Y. L. Zhou, H. C. Bi, X. Xie, and L. T. Sun, Fabrication of graphene based electrothermal cantilever actuator, The 8th Annual IEEE International Conference on Nano/Micro Engineered and Molecular Systems, pp. 911–914, 2013.

[14] Y. Hu, T. Lan, G. Wu, Z. C. Zhu, and W. Chen, A spongy graphene based bimorph actuator with ultra-large displacement towards biomimetic application, Nanoscale, vol. 6, no. 21, pp. 12703–12709, 2014.

[15] L. F. Chang, M. J. Huang, K. Qi, Z. Jing, L. L. Yang, P. Lu, Y. Hu, and Y. C. Wu, Graphene-based bimorph actuators with dual-response and large-deformation by a simple method, Macromol. Mater. Eng., vol. 304, no. 4, Art. no. 1800688, 2019.

[16] H. Kawai, The Piezoelectricity of Poly (vinylidene Fluoride), Jpn. J. Appl. Phys., vol. 8, no. 7, pp. 975–976, 1969.

[17] Y. Fang, X. O. Tan, Y. T. Shen, N. Xi, and G. Alici, A scalable model for trilayer conjugated polymer actuators and its experimental validation, Mater. Sci. Eng. C-Biomimetic Supramol. Syst., vol. 28, no. 3, pp. 421–428, 2008.

[18] R. Perez, M. Kral, H. Bleuler, and R. Clavel, A polyvinylidene fluoride (PVDF) based bimorph actuator for high speed laser beam manipulation, Smart Sensors, Actuators, and MEMS V, vol. 8066, Art. no. 80660R, 2011.

[19] Y. C. Wu, K. Y. Ho, K. Kariya, R. X. Xu, W. H. Cai, J. W. Zhong, Y. Ma, M. Zhang, X. H. Wang, and L. W. Lin, Pre-curved PVDF/PI unimorph structures for biomimic soft crawling actuators, 2018 IEEE Micro Electro Mechanical Systems (MEMS), pp. 581–584, 2018.

[20] R. Y. Ting, and Q. M. Zhang, New electrostrictive PVDF copolymers for large-strain actuator application, Fifth European Conference on Smart Structures and Materials, vol. 4073, pp. 48–58, 2000.

[21] G. Gutierrez-Sanchez, J. Hernando-Garcia, V. Ruiz-Diez, O. J. Dura, M. A. Lopez De La Torre, and J. L. Sanchez-Rojas, Comparative assessment of PVDF and PVDF-TrFE piezoelectric polymers for flexible actuators applications, Smart Sensors, Actuators, and MEMS VIII, vol. 10246, Art. no. 102460N, 2017.

[22] L. Engel, K. R. Van Volkinburg, M. Ben-David, G. N. Washington, S. Krylov, and Y. Shacham-Diamand, Fabrication of a self-sensing electroactive polymer bimorph actuator based on polyvinylidene fluoride and its electrostrictive terpolymer, Electroactive Polymer Actuators and Devices (EAPAD) 2016, vol. 9798, Art. no. 97980M, 2016.

[23] J. Shklovsky, A. Reuveny, Y. Sverdlov, S. Krylov, and Y. Shacham-Diamand, Towards fully polymeric electroactive micro actuators with conductive polymer electrodes, Microelectron. Eng., vol. 199, pp. 58–62, 2018.

[24] H. Shigemune, S. Sugano, J. Nishitani, M. Yamauchi, N. Hosoya, S. Hashimoto, and S. Maeda, Dielectric elastomer actuators with carbon nanotube electrodes painted with a soft brush, Actuators, vol. 7, no. 3, Art. no. 51, 2018.

[25] F. Carpi, R. Kornbluh, P. Sommer-Larsen, and G. Alici, Electroactive polymer actuators as artificial muscles: are they ready for bioinspired applications?, Bioinspir. Biomim., vol. 6, no. 4, Art. no. 045006, 2011.

[26] K. Jun, J. Kim, and I. K. Oh, An electroactive and transparent haptic interface utilizing soft elastomer actuators with silver nanowire electrodes, Small, vol. 14, no. 35, Art. no. 1801603, 2018.

[27] A. Nicolau-Kuklinska, P. Latko-Durałek, P. Nakonieczna, K. Dydek, A. Boczkowska, and J. Grygorczuk, A new electroactive polymer based on carbon nanotubes and carbon grease as compliant electrodes for electroactive actuators, J. Intell. Mater. Syst. Struct., vol. 29, no. 7, pp. 1520–1530, 2017.

[28] G. K. Lau, T. G. La, E. S. W. Foong, and M. Shrestha, Stronger multilayer acrylic dielectric elastomer actuators with silicone gel coatings, Smart Mater. Struct., vol. 25, no. 12, Art. no. 125006, 2016.

[29] D. Gonzalez, J. Garcia, and B. Newell, Electromechanical characterization of a 3D printed dielectric material for dielectric electroactive polymer actuators, Sens. Actuator A-Phys., vol. 297, Art. no. 111565, 2019.

[30] Y. Bar-Cohen, and Q. M. Zhang, Electroactive polymer actuators and sensors, MRS Bull., vol. 33, no. 3, pp. 173–181, 2008.

[31] M. Y. Hao, Y. J. Wang, Z. C. Zhu, Q. S. He, D. L. Zhu, and M. Z. Luo, A compact review of IPMC as soft actuator and sensor: current trends, challenges, and potential solutions from our recent work, Front. Robot. AI, vol. 6, Art. no. 129, 2019.

[32] M. Annabestani and N. Naghavi, Nonlinear identification of IPMC actuators based on ANFIS–NARX paradigm, Sens. Actuator A-Phys., vol. 209, pp. 140–148, 2014.

[33] S. S. Nakshatharan, A. Punning, U. Johanson, and A. Aabloo, Modelling and control of self-sensing ionic electroactive polymer actuator, Electroactive Polymer Actuators and Devices (EAPAD) XXI, vol. 10966, Art. no. 109661C, 2019.

[34] C. Heitner-Wirguin, Recent advances in perfluorinated ionomer membranes: structure, properties and applications, J. Membr. Sci., vol. 120, no. 1, pp. 1–33, 1996.

[35] K. A. Mauritz and R. B. Moore, State of understanding of Nafion, Chem. Rev., vol. 104, no. 10, pp. 4535–4586, 2004.

[36] J. Ru, C. S. Bian, Z. C. Zhu, Y. J. Wang, J. S. Zhang, T. Horiuchi, T. Sugino, X. F. Liu, H. L. Chen, and K. Asaka, Controllable and durable ionic electroactive polymer actuator based on nanoporous carbon nanotube film electrode, Smart Mater. Struct., vol. 28, no. 8, Art. no. 085032, 2019.

[37] V. Palmre, E. Lust, A. Jänes, M. Koel, A. L. Peikolainen, J. Torop, U. Johanson, and A. Aabloo, Electroactive polymer actuators with carbon aerogel electrodes, J. Mater. Chem.,

vol. 21, no. 8, pp. 2577–2583, 2011.

[38] G. J. H. Melvin, Q. Q. Ni, and T. Natsuki, Behavior of polymer-based electroactive actuator incorporated with mild hydrothermally treated CNTs, Appl. Phys. A-Mater. Sci. Process., vol. 117, no. 4, pp. 2043–2050, 2014.

[39] G. J. H. Melvin, Q. Q. Ni, and T. Natsuki, Fabrication and characterization of polymer-based electroactive nanocomposite actuator, Microelectron. Eng., vol. 126, pp. 9–12, 2014.

[40] A. Mazzoldi, M. Tesconi, A. Tognetti, W. Rocchia, G. Vozzi, G. Pioggia, A. Ahluwalia, and D. De Rossi, Electroactive carbon nanotube actuators: Soft-lithographic fabrication and electro-chemical modelling, Mater. Sci. Eng. C-Biomimetic Supramol. Syst., vol. 28, no. 7, pp. 1057–1064, 2008.

[41] Y. S. Yan, T. Santaniello, L. G. Bettini, C. Minnai, A. Bellacicca, R. Porotti, I. Denti, G. Faraone, M. Merlini, C. Lenardi, and P. Milani, Electroactive ionic soft actuators with monolithically integrated gold nanocomposite electrodes, Adv. Mater., vol. 29, no. 23, Art. no. 1606109, 2017.

[42] S. V. Ebadi, D. Semnani, H. Fashandi, and B. Rezaei, Synthesis and characterization of a novel polyurethane/polypyrrole-p-toluenesulfonate (PU/PPy-pTS) electroactive nanofibrous bending actuator, Polym. Adv. Technol., vol. 30, no. 9, pp. 2261–2274, 2019.

[43] P. Garstecki, P. Tierno, D. B. Weibel, F. Sagues, and G. M. Whitesides, Propulsion of flexible polymer structures in a rotating magnetic field, J. Phys.-Condes. Matter, vol. 21, no. 20, Art. no. 204110, 2009.

[44] M. Khoo and C. Liu, Micro magnetic silicone elastomer membrane actuator, Sens. Actuator A-Phys., vol. 89, no. 3, pp. 259–266, 2001.

[45] E. Diller, J. Zhuang, G. Z. Lum, M. R. Edwards, and M. Sitti, Continuously distributed magnetization profile for millimeter-scale elastomeric undulatory swimming, Appl. Phys. Lett., vol. 104, no. 17, Art. no. 174101, 2014.

[46] L. V. Nikitin, D. G. Korolev, G. V. Stepanov, and L. S. Mironova, Experimental study of magnetoelastics, J. Magn. Magn. Mater., vol. 300, no. 1, pp. E234–E238, 2006.

[47] E. Diller and M. Sitti, Three-dimensional programmable assembly by untethered magnetic robotic micro-grippers, Adv. Funct. Mater., vol. 24, no. 28, pp. 4397–4404, 2014.

[48] H. Zhou and G. Alici, Modeling and experimental characterization of magnetic membranes as soft smart actuators for medical robotics, 2017 IEEE International Conference on Advanced Intelligent Mechatronics (AIM), pp. 797–802, 2017.

[49] S. Fusco, H. W. Huang, K. E. Peyer, C. Peters, M. Haberli, A. Ulbers, A. Spyrogianni, E. Pellicer, J. Sort, S. E. Pratsinis, B. J. Nelson, M. S. Sakar, and S. Pane, Shape-switching microrobots for medical applications: the influence of shape in drug delivery and locomotion, ACS Appl. Mater. Interfaces, vol. 7, no. 12, pp. 6803–6811, 2015.

[50] M. M. Schmauch, S. R. Mishra, B. A. Evans, O. D. Velev, and J. B. Tracy, Chained iron microparticles for directionally controlled actuation of soft robots, ACS Appl. Mater. Interfaces, vol. 9, no. 13, pp. 11895–11901, 2017.

[51] R. Fuhrer, E. K. Athanassiou, N. A. Luechinger, and W. J. Stark, Crosslinking metal nanoparticles into the polymer backbone of hydrogels enables preparation of soft, magnetic field-driven actuators with muscle-like flexibility, Small, vol. 5, no. 3, pp. 383–388, 2009.

[52] Y. Yamanishi, S. Sakuma, and F. Arai, Magnetically modified soft micro actuators for oocyte manipulation, 2007 International Symposium on Micro-NanoMechatronics and Human Science, pp. 442–447, 2007.

[53] H. Taniguchi, M. Miyake, and K. Suzumori, Development of new soft actuator using magnetic intelligent fluids for flexible walking robot, International Conference on Control, Automation and Systems (ICCAS 2010), pp. 1797–1801, 2010.

[54] Z. Y. Ji, C. Y. Yan, B. Yu, X. L. Wang, and F. Zhou, Multimaterials 3D printing for free assembly manufacturing of magnetic driving soft actuator, Adv. Mater. Interfaces, vol. 4, no. 22, Art. no. 1700629, 2017.

[55] Z. Q. Dong, Y. Cao, Q. J. Yuan, Y. F. Wang, J. H. Li, B. J. Li, and S. Zhang, Redox- and glucose-induced shape-memory polymers, Macromol. Rapid Commun., vol. 34, no. 10, pp. 867–872, 2013.

[56] A. Yasin, H. Z. Li, Z. Lu, S. U. Rehman, M. Siddiq, and H. Y. Yang, A shape memory hydrogel induced by the interactions between metal ions and phosphate, Soft Matter, vol. 10, no. 7, pp. 972–977, 2014.

[57] Q. Zhao, J. W. C. Dunlop, X. L. Qiu, F. H. Huang, Z. B. Zhang, J. Heyda, J. Dzubiella, M. Antonietti, and J. Y. Yuan, An instant multi-responsive porous polymer actuator driven by solvent molecule sorption, Nat. Commun., vol. 5, Art. no. 4293, 2014.

[58] H. Lee, C. G. Xia, and N. X. Fang, First jump of microgel; actuation speed enhancement by elastic instability, Soft Matter, vol. 6, no. 18, pp. 4342–4345, 2010.

[59] R. Yoshida, Self-oscillating gels driven by the Belousov-Zhabotinsky reaction as novel smart materials, Adv. Mater., vol. 22, no. 31, pp. 3463–3483, 2010.

[60] S. Maeda, Y. Hara, T. Sakai, R. Yoshida, and S. Hashimoto, Self-walking gel, Adv. Mater., vol. 19, no. 21, pp. 3480–3484, 2007.

[61] D. Suzuki, T. Kobayashi, R. Yoshida, and T. Hirai, Soft actuators of organized self-oscillating microgels, Soft Matter, vol. 8, no. 45, pp. 11447–11449, 2012.

[62] X. J. Han, Z. Q. Dong, M. M. Fan, Y. Liu, J. H. Li, Y. F. Wang, Q. J. Yuan, B. J. Li, and S. Zhang, pH-induced shape-memory polymers, Macromol. Rapid Commun., vol. 33, no.12, pp. 1055–1060, 2012.

[63] H. Meng, J. Zheng, X. F. Wen, Z. Q. Cai, J. W. Zhang, and T. Chen, pH- and sugar-induced shape memory hydrogel based on reversible phenylboronic acid-diol ester bonds, Macromol. Rapid Commun., vol. 36, no. 6, pp. 533–537, 2015.

[64] S. J. Lee, D. Y. Lee, Y. S. Song, and N. I. Cho, Chemically driven polyacrylonitrile fibers as a linear actuator, Solid State Phenomena, vol. 124-126, pp. 1197–1200, 2007.

[65] K. Choe, K. J. Kim, D. Kim, C. Manford, S. Heo, and M. Shahinpoor, Performance characteristics of electro–chemically driven polyacrylonitrile fiber bundle actuators, J. Intell. Mater. Syst. Struct., vol. 17, no. 7, pp. 563–576, 2006.

[66] J. Y. Park, H. J. Oh, D. J. Kim, J. Y. Baek, and S. H. Lee, A polymeric microfluidic valve employing a pH-responsive hydrogel microsphere as an actuating source, J. Micromech. Microeng., vol. 16, no. 3, pp. 656–663, 2006.

[67] L. Dong, A. K. Agarwal, D. J. Beebe, and H. R. Jiang, Adaptive liquid microlenses activated by stimuli-responsive hydrogels, Nature, vol. 442, no. 7102, pp. 551–554, 2006.

[68] H. M. Chen, Y. Li, Y. Liu, T. Gong, L. Wang, and S. B. Zhou, Highly pH-sensitive polyurethane exhibiting shape memory and drug release, Polym. Chem., vol. 5, no. 17, pp. 5168–5174, 2014.

[69] C. H. Ye, S. V. Nikolov, R. Calabrese, A. Dindar, A. Alexeev, B. Kippelen, D. L. Kaplan, and V. V. Tsukruk, Self-(un)rolling biopolymer microstructures: rings, tubules, and helical tubules from the same material, Angew. Chem. Int. Edit., vol. 54, no. 29, pp. 8490–8493, 2015.

[70] L. Ionov, Biomimetic hydrogel-based actuating systems, Adv. Funct. Mater., vol. 23, no. 36, pp. 4555–4570, 2013.

[71] L. Ionov, Hydrogel-based actuators: possibilities and limitations, Mater. Today, vol. 17, no. 10, pp. 494–503, 2014.

[72] M. M. Ma, L. Guo, D. G. Anderson, and R. Langer, Bio-inspired polymer composite actuator and generator driven by water gradients, Science, vol. 339, no. 6116, pp. 186–189, 2013.

[73] M. Dai, O. T. Picot, J. M. N. Verjans, L. T. de Haan, A. P. H. J. Schenning, T. Peijs, and C. W. M. Bastiaansen, Humidity-responsive bilayer actuators based on a liquid-crystalline polymer network, ACS Appl. Mater. Interfaces, vol. 5, no. 11, pp. 4945–4950, 2013.

[74] L. T. de Haan, J. M. N. Verjans, D. J. Broer, C. W. M. Bastiaansen, and A. P. H. J. Schenning, Humidity-responsive liquid crystalline polymer actuators with an asymmetry in the molecular trigger that bend, fold, and curl, J. Am. Chem. Soc., vol. 136, no. 30, pp. 10585–10588, 2014.

[75] Y. Ma, Y. Y. Zhang, B. S. Wu, W. P. Sun, Z. G. Li, and J. Q. Sun, Polyelectrolyte multilayer films for building energetic walking devices, Angew. Chem. Int. Edit., vol. 50, no. 28, pp. 6254–6257, 2011.

[76] X. Chen, D. Goodnight, Z. H. Gao, A. H. Cavusoglu, N. Sabharwal, M. Delay, A. Driks, and O. Sahin, Scaling up nanoscale water-driven energy conversion into evaporation-driven engines and generators, Nat. Commun., vol. 6, Art. no. 7346, 2015.

[77] T. H. Kim, J. G. Choi, J. Y. Byun, Y. Jang, S. M. Kim, G. M. Spinks, and S. J. Kim, Biomimetic thermal-sensitive multi-transform actuator, Sci. Rep., vol. 9, Art. no. 7905, 2019.

[78] S. Z. Zhou, B. Y. Wu, Q. Zhou, Y. K. Jian, X. X. Le, H. H. Lu, D. C. Zhang, J. W. Zhang, Z. H. Zhang, and T. Chen, Ionic strength and thermal dual-responsive bilayer hollow spherical hydrogel actuator, Macromol. Rapid Commun., vol. 41, no. 8, Art. no. 1900543, 2020.

[79] Y. H. Wu, Y. Yang, X. J. Qian, Q. M. Chen, Y. Wei, and Y. Ji, Liquid crystalline soft actuators with switchable thermal reprogrammability, Angew. Chem. Int. Edit., vol. 59, no. 12, pp. 4778–4784, 2020.

[80] H. Y. Jeong, E. Lee, S. Ha, N. Kim, and Y. C. Jun, Multistable thermal actuators via multimaterial 4D printing, Adv. Mater. Technol., vol. 4, no. 3, Art. no. 1800495, 2018.

[81] H. Xie, L. Li, C. Y. Cheng, K. K. Yang, and Y. Z. Wang, Poly(ethylene-co-vinyl acetate)/graphene shape-memory actuator with a cyclic thermal/light dual-sensitive capacity, Compos. Sci. Technol., vol. 173, pp. 41–46, 2019.

[82] M. C. LeMieux, M. E. McConney, Y. H. Lin, S. Singamaneni, H. Jiang, T. J. Bunning, and V. V. Tsukruk, Polymeric nanolayers as actuators for ultrasensitive thermal bimorphs, Nano Lett., vol. 6, no. 4, pp. 730–734, 2006.

[83] B. E. Schubert, and D. Floreano, Variable stiffness material based on rigid low-melting-point-alloy microstructures embedded in soft poly (dimethylsiloxane) (PDMS), RSC Adv., vol. 3, no. 46, pp. 24671–24679, 2013.

[84] D. Yoon, Y. W. Son, and H. Cheong, Negative thermal expansion coefficient of graphene measured by Raman spectroscopy, Nano Lett., vol. 11, no. 8, pp. 3227–3231, 2011.

[85] P. S. Xiao, N. B. Yi, T. F. Zhang, Y. Huang, H. C. Chang, Y. Yang, Y. Zhou, and Y. S. Chen, Construction of a fish-like robot based on high performance graphene/PVDF bimorph actuation materials, Adv. Sci., vol. 3, no. 6, Art. no. 1500438, 2016.

[86] H. Kim, H. Lee, I. Ha, J. Jung, P. Won, H. Cho, J. Yeo, S. Hong, S. Han, J. Kwon, K. J. Cho, and S. H. Ko, Biomimetic color changing anisotropic soft actuators with integrated metal nanowire percolation network transparent heaters for soft robotics, Adv. Funct. Mater., vol. 28, no. 32, Art. no. 1801847, 2018.

[87] Z. Cui, Y. W. Han, Q. J. Huang, J. Y. Dong, and Y. Zhu, Electrohydrodynamic printing of silver nanowires for flexible and stretchable electronics, Nanoscale, vol. 10, no. 15, pp. 6806–6811, 2018.

[88] J. A. Song, and Y. Zhang, From two-dimensional to three-dimensional structures: A superior thermal-driven actuator with switchable deformation behavior, Chem. Eng. J., vol. 360, pp.

680–685, 2019.

[89] S. J. Liu, N. Masurkar, S. Varma, I. Avrutsky, and L. M. R. Arava, Experimental studies and numerical simulation of polypyrrole trilayer actuators, ACS Omega, vol. 4, no. 4, pp. 6436–6442, 2019.

[90] Y. Hu, A. F. Xu, J. Q. Liu, L. L. Yang, L. F. Chang, M. J. Huang, W. B. Gu, G. Wu, P. Lu, W. Chen, and Y. C. Wu, Multifunctional soft actuators based on anisotropic paper/polymer bilayer toward bioinspired applications, Adv. Mater. Technol., vol. 4, no. 3, Art. no. 1800674, 2019.

[91] Leeladhar, P. Raturi, A. Kumar, and J. P. Singh, Graphene-polydimethylsiloxane/chromium bilayer-based flexible, reversible, and large bendable photomechanical actuators, Smart Mater. Struct., vol. 26, no. 9, Art. no. 095030, 2017.

[92] D. Niu, W. T. Jiang, H. Z. Liu, T. T. Zhao, B. A. Lei, Y. H. Li, L. Yin, Y. S. Shi, B. D. Chen, and B. H. Lu, Reversible bending behaviors of photomechanical soft actuators based on graphene nanocomposites, Sci. Rep., vol. 6, Art. no. 27366, 2016.

[93] Leeladhar, P. Raturi, and J. P. Singh, Sunlight-driven eco-friendly smart curtain based on infrared responsive graphene oxide-polymer photoactuators, Sci. Rep., vol. 8, Art. no. 3687, 2018.

[94] R. Tang, W. Sang, Y. P. Wu, C. H. Zhu, and J. Liu, Multi-wavelength light drivable oscillatory actuator on graphene-based bilayer film, Macromol. Mater. Eng., vol. 302, no. 2, Art. no. 1600384, 2017.

[95] M. Y. Ji, N. Jiang, J. Chang, and J. Q. Sun, Near-infrared light-driven, highly efficient bilayer actuators based on polydopamine-modified reduced graphene oxide, Adv. Funct. Mater., vol. 24, no. 34, pp. 5412–5419, 2014.

[96] Z. H. Tang, Z. W. Gao, S. H. Jia, F. Wang, and Y. L. Wang, Graphene-based polymer bilayers with superior light-driven properties for remote construction of 3D structures, Adv. Sci., vol. 4, no. 5, Art. no. 1600437, 2017.

[97] C. L. Huang, J. A. Lv, X. J. Tian, Y. C. Wang, Y. L. Yu, and J. Liu, Miniaturized swimming soft robot with complex movement actuated and controlled by remote light signals, Sci. Rep., vol. 5, Art. no. 17414, 2015.

[98] J. Lee, S. Oh, J. Pyo, J. M. Kim, and J. H. Je, A light-driven supramolecular nanowire actuator, Nanoscale, vol. 7, no. 15, pp. 6457–6461, 2015.

[99] M. Irie, T. Fukaminato, K. Matsuda, and S. Kobatake, Photochromism of diarylethene molecules and crystals: memories, switches, and actuators, Chem. Rev., vol. 114, no. 24, pp. 12174–12277, 2014.

[100] A. Julia-Lopez, J. Hernando, D. Ruiz-Molina, P. Gonzalez-Monje, J. Sedo, and C. Roscini, Temperature-controlled switchable photochromism in solid materials, Angew. Chem. Int.

Edit., vol. 55, no. 48, pp. 15044–15048, 2016.

[101] Z. C. Jiang, Y. Y. Xiao, and Y. Zhao, Shining light on liquid crystal polymer networks: preparing, reconfiguring, and driving soft actuators, Adv. Opt. Mater., vol. 7, no. 16, Art. no. 1900262, 2019.

[102] J. A. Lv, W. Wang, W. Wu, and Y. L. Yu, A reactive azobenzene liquid-crystalline block copolymer as a promising material for practical application of light-driven soft actuators, J. Mater. Chem. C, vol. 3, no. 26, pp. 6621–6626, 2015.

[103] C. Q. Qin, Y. Y. Feng, W. Luo, C. Cao, W. P. Hu, and W. Feng, A supramolecular assembly of cross-linked azobenzene/polymers for a high-performance light-driven actuator, J. Mater. Chem. A, vol. 3, no. 32, pp. 16453–16460, 2015.

[104] J. Hu, X. Li, Y. Ni, S. D. Ma, and H. F. Yu, A programmable and biomimetic photo-actuator: a composite of a photo-liquefiable azobenzene derivative and commercial plastic film, J. Mater. Chem. C, vol. 6, no. 40, pp. 10815–10821, 2018.

[105] K. D. Harris, R. Cuypers, P. Scheibe, C. L. van Oosten, C. W. M. Bastiaansen, J. Lub, and D. J. Broer, Large amplitude light-induced motion in high elastic modulus polymer actuators, J. Mater. Chem., vol. 15, no. 47, pp. 5043–5048, 2005.

[106] A. Ryabchun, A. Bobrovsky, J. Stumpe, and V. Shibaev, Novel generation of liquid crystalline photo-actuators based on stretched porous polyethylene films, Macromol. Rapid Commun., vol. 33, no. 11, pp. 991–997, 2012.

[107] C. L. van Oosten, C. W. M. Bastiaansen, and D. J. Broer, Printed artificial cilia from liquid-crystal network actuators modularly driven by light, Nat. Mater., vol. 8, no. 8, pp. 677–682, 2009.

[108] Z. Jiang, M. Xu, F. Y. Li, and Y. L. Yu, Red-light-controllable liquid-crystal soft actuators via low-power excited upconversion based on triplet–triplet annihilation, J. Am. Chem. Soc., vol. 135, no. 44, pp. 16446–16453, 2013.

[109] S. Z. Li, G. Han, and W. Q. Zhang, Concise synthesis of photoresponsive polyureas containing bridged azobenzenes as visible-light-driven actuators and reversible photopatterning, Macromolecules, vol. 51, no. 11, pp. 4290–4297, 2018.

[110] A. H. Gelebart, D. J. Mulder, G. Vantomme, A. P. H. J. Schenning, and D. J. Broer, A rewritable, reprogrammable, dual light-responsive polymer actuator, Angew. Chem. Int. Edit., vol. 56, no. 43, pp. 13436–13439, 2017.

[111] D. Kitagawa, H. Nishi, and S. Kobatake, Photoinduced twisting of a photochromic diarylethene crystal, Angew. Chem. Int. Edit., vol. 52, no. 35, pp. 9320–9322, 2013.

[112] M. Mauro, Gel-based soft actuators driven by light, J. Mat. Chem. B, vol. 7, no. 27, pp. 4234–4242, 2019.

[113] X. F. Ma, X. Y. Lan, L. L. Wu, L. Wang, Q. Gu, Y. J. Shi, X. L. Gu, and Z. Y. Luo, Photo-induced actuator using temperature and light dual responsive azobenzene containing ion gel in ionic liquid, Eur. Polym. J., vol. 123, Art. no. 109446, 2020.

[114] W. Francis, A. Dunne, C. Delaney, L. Florea, and D. Diamond, Spiropyran based hydrogels actuators—Walking in the light, Sens. Actuator B-Chem., vol. 250, pp. 608–616, 2017.

[115] H. K. Yap, J. H. Lim, F. Nasrallah, J. C. H. Goh, and R. C. H. Yeow, A soft exoskeleton for hand assistive and rehabilitation application using pneumatic actuators with variable stiffness, 2015 IEEE International Conference on Robotics and Automation (ICRA), pp. 4967–4972, 2015.

[116] A. Firouzeh, M. Salerno, and J. Paik, Soft pneumatic actuator with adjustable stiffness layers for multi-DoF actuation, 2015 IEEE/RSJ International Conference on Intelligent Robots and Systems (IROS), pp. 1117–1124, 2015.

[117] Y. Sun, Y. S. Song, and J. Paik, Characterization of silicone rubber based soft pneumatic actuators, 2013 IEEE/RSJ International Conference on Intelligent Robots and Systems, pp. 4446–4453, 2013.

[118] N. Farrow and N. Correll, A soft pneumatic actuator that can sense grasp and touch, 2015 IEEE/RSJ International Conference on Intelligent Robots and Systems (IROS), pp. 2317–2323, 2015.

[119] J. Y. Nagase, S. Wakimoto, T. Satoh, N. Saga, and K. Suzumori, Design of a variable-stiffness robotic hand using pneumatic soft rubber actuators, Smart Mater. Struct., vol. 20, no. 10, Art. no. 105015, 2011.

[120] Y. F. Zhang, C. J. X. Ng, Z. Chen, W. Zhang, S. Panjwani, K. Kowsari, H. Y. Yang, and Q. Ge, Soft robotics: miniature pneumatic actuators for soft robots by high-resolution multimaterial 3D printing, Adv. Mater. Technol., vol. 4, no. 10, Art. no. 1900427, 2019.

[121] Q. P. Xu and J. Y. Liu, Effective enhanced model for a large deformable soft pneumatic actuator, Acta Mech. Sin., vol. 36, no. 1, pp. 245–255, 2019.

[122] S. Wakimoto, K. Ogura, K. Suzumori, and Y. Nishioka, Miniature soft hand with curling rubber pneumatic actuators, 2009 IEEE International Conference on Robotics and Automation, pp. 513–518, 2009.

[123] T. Sun, Y. L. Chen, T. Y. Han, C. L. Jiao, B. B. Lian, and Y. M. Song, A soft gripper with variable stiffness inspired by pangolin scales, toothed pneumatic actuator and autonomous controller, Robot. Comput.-Integr. Manuf., vol. 61, Art. no. 101848, 2020.

[124] J. B. Wang, Y. Q. Fei, and W. Pang, Design, modeling, and testing of a soft pneumatic glove with segmented pneuNets bending actuators, IEEE-ASME Trans. Mechatron., vol. 24, no. 3, pp. 990–1001, 2019.

[125] G. Udupa, P. Sreedharan, P. S. Dinesh, and D. Kim, Asymmetric bellow flexible pneumatic

actuator for miniature robotic soft gripper, J. Robot., vol. 2014, Art. no. 902625, 2014.

[126] K. Suzumori, S. Endo, T. Kanda, N. Kato, and H. Suzuki, A bending pneumatic rubber actuator realizing soft-bodied manta swimming robot, Proceedings of the 2007 IEEE International Conference on Robotics and Automation, pp. 4975–4980, 2007.

[127] L. S. Ge, L. T. Dong, D. Wang, Q. Ge, and G. Y. Gu, A digital light processing 3D printer for fast and high-precision fabrication of soft pneumatic actuators, Sens. Actuator A-Phys., vol. 273, pp. 285–292, 2018.

[128] Herianto, I. Wira, R. A. Syahirul, and P. Aishah, Design and fabrication in the loop of soft pneumatic actuators using fused deposition modelling, Sens. Actuator A-Phys., vol. 298, Art. no. 111556, 2019.

[129] J. Schneider, P. Rohner, D. Thureja, M. Schmid, P. Galliker, and D. Poulikakos, Electrohydrodynamic nanodrip printing of high aspect ratio metal grid transparent electrodes, Adv. Funct. Mater., vol. 26, no. 6, pp. 833–840, 2015.

[130] M. S. Onses, C. Song, L. Williamson, E. Sutanto, P. M. Ferreira, A. G. Alleyne, P. F. Nealey, H. Ahn, and J. A. Rogers, Hierarchical patterns of three-dimensional block-copolymer films formed by electrohydrodynamic jet printing and self-assembly, Nat. Nanotechnol., vol. 8, no. 9, pp. 667–675, 2013.

[131] B. W. An, K. Kim, H. Lee, S. Y. Kim, Y. Shim, D. Y. Lee, J. Y. Song, and J. U. Park, High-resolution printing of 3D structures using an electrohydrodynamic inkjet with multiple functional inks, Adv. Mater., vol. 27, no. 29, pp. 4322–4328, 2015.

[132] A. Khan, K. Rahman, D. S. Kim, and K. H. Choi, Direct printing of copper conductive micro-tracks by multi-nozzle electrohydrodynamic inkjet printing process, J. Mater. Process. Technol., vol. 212, no. 3, pp. 700–706, 2012.

[133] J. U. Park, M. Hardy, S. J. Kang, K. Barton, K. Adair, D. K. Mukhopadhyay, C. Y. Lee, M. S. Strano, A. G. Alleyne, J. G. Georgiadis, P. M. Ferreira, and J. A. Rogers, High-resolution electrohydrodynamic jet printing, Nat. Mater., vol. 6, no. 10, pp. 782–789, 2007.

[134] S. Mishra, K. L. Barton, A. G. Alleyne, P. M. Ferreira, and J. A. Rogers, High-speed and drop-on-demand printing with a pulsed electrohydrodynamic jet, J. Micromech. Microeng., vol. 20, no. 9, Art. no. 095026, 2010.

[135] K. Barton, S. Mishra, K. A. Shorter, A. Alleyne, P. Ferreira, and J. Rogers, A desktop electrohydrodynamic jet printing system, Mechatronics, vol. 20, no. 5, pp. 611–616, 2010.

[136] A. Khan, K. Rahman, M. T. Hyun, D. S. Kim, and K. H. Choi, Multi-nozzle electrohydrodynamic inkjet printing of silver colloidal solution for the fabrication of electrically functional microstructures, Appl. Phys. A-Mater. Sci. Process., vol. 104, no. 4, pp. 1113–1120, 2011.

[137] E. Sutanto, K. Shigeta, Y. K. Kim, P. G. Graf, D. J. Hoelzle, K. L. Barton, A. G. Alleyne, P.

M. Ferreira, and J. A. Rogers, A multimaterial electrohydrodynamic jet (E-jet) printing system, J. Micromech. Microeng., vol. 22, no. 4, Art. no. 045008, 2012.

[138] B. Zhang, J. K. He, X. Li, F. Y. Xu, and D. C. Li, Micro/nanoscale electrohydrodynamic printing: from 2D to 3D, Nanoscale, vol. 8, no. 34, pp. 15376–15388, 2016.

[139] Y. W. Han, and J. Y. Dong, Electrohydrodynamic (EHD) printing of molten metal ink for flexible and stretchable conductor with self-healing capability, Adv. Mater. Technol. vol. 3, no. 3, Art. no. 1700268, 2018.

[140] Y. Cao and J. Y. Dong, High-performance low-voltage soft electrothermal actuator with directly printed micro-heater, Sens. Actuator A-Phys., vol. 297, Art. no. 111546, 2019.

[141] D. Y. Lee, Y. S. Shin, S. E. Park, T. U. Yu, and J. Hwang, Electrohydrodynamic printing of silver nanoparticles by using a focused nanocolloid jet, Appl. Phys. Lett., vol. 90, no. 8, Art. no. 081905, 2007.

[142] P. L. Zhou, H. B. Yu, W. H. Zou, Z. D. Wang, and L. Q. Liu, High-resolution and controllable nanodeposition pattern of Ag nanoparticles by electrohydrodynamic jet printing combined with coffee ring effect, Adv. Mater. Interfaces, vol. 6, no. 20, Art. no. 1900912, 2019.

[143] Y. J. Jeong, X. Lee, J. Bae, J. Jang, S. W. Joo, S. Lim, S. H. Kim, and C. E. Park, Direct patterning of conductive carbon nanotube/polystyrene sulfonate composites via electrohydrodynamic jet printing for use in organic field-effect transistors, J. Mater. Chem. C, vol. 4, no. 22, pp. 4912–4919, 2016.

[144] D. Z. Wang, W. Zha, L. Feng, Q. Ma, X. M. Liu, N. Yang, Z. Xu, X. J. Zhao, J. S. Liang, T. Q. Ren, and X. D. Wang, Electrohydrodynamic jet printing and a preliminary electrochemistry test of graphene micro-scale electrodes, J. Micromech. Microeng., vol. 26, no. 4, Art. no. 045010, 2016.

[145] B. Zhang, J. Lee, M. Kim, N. Lee, H. Lee, and D. Byun, Direct patterning and spontaneous self-assembly of graphene oxide via electrohydrodynamic jet printing for energy storage and sensing, Micromachines, vol. 11, no. 1, Art. no. 13, 2019.

[146] B. W. An, K. Kim, M. Kim, S. Y. Kim, S. H. Hur, and J. U. Park, Direct printing of reduced graphene oxide on planar or highly curved surfaces with high resolutions using electrohydrodynamics, Small, vol. 11, no. 19, pp. 2263–2268, 2015.

[147] A. Gupta, A. M. Seifalian, Z. Ahmad, M. J. Edirisinghe, and M. C. Winslet, Novel electrohydrodynamic printing of nanocomposite biopolymer scaffolds, J. Bioact. Compat. Polym., vol. 22, no. 3, pp. 265–280, 2007.

[148] S. Maktabi and P. R. Chiarot, Electrohydrodynamic printing of organic polymeric resistors on flat and uneven surfaces, J. Appl. Phys., vol. 120, no. 8, Art. no. 084903, 2016.

[149] J. U. Park, J. H. Lee, U. Paik, Y. Lu, and J. A. Rogers, Nanoscale patterns of oligonucleotides

formed by electrohydrodynamic jet printing with applications in biosensing and nanomaterials assembly, Nano Lett., vol. 8, no. 12, pp. 4210–4216, 2008.

[150] A. Kwok, S. Arumuganathar, S. Irvine, J. R. Mcewan, and S. N. Jayasinghe, A hybrid bio-jetting approach for directly engineering living cells, Biomed. Mater., vol. 3, no. 2, Art. no. 025008, 2008.

[151] L. Gasperini, D. Maniglio, A. Motta, and C. Migliaresi, An electrohydrodynamic bioprinter for alginate hydrogels containing living cells, Tissue Eng. Part C-Methods, vol. 21, no. 2, pp. 123–132, 2015.

[152] S. Khan, Y. H. Doh, A. Khan, A. Rahman, K. H. Choi, and D. S. Kim, Direct patterning and electrospray deposition through EHD for fabrication of printed thin film transistors, Curr. Appl. Phys., vol. 11, no. 1, pp. S271–S279, 2011.

[153] N. Duraisamy, N. M. Muhammad, H. C. Kim, J. D. Jo, and K. H. Choi, Fabrication of TiO2 thin film memristor device using electrohydrodynamic inkjet printing, Thin Solid Films, vol. 520, no. 15, pp. 5070–5074, 2012.

[154] S. Y. Kim, K. Kim, Y. H. Hwang, J. Park, J. Jang, Y. Nam, Y. Kang, M. Kim, H. J. Park, Z. Lee, J. Choi, Y. Kim, S. Jeong, B. S. Bae, and J. U. Park, High-resolution electrohydrodynamic inkjet printing of stretchable metal oxide semiconductor transistors with high performance, Nanoscale, vol. 8, no. 39, pp. 17113–17121, 2016.

[155] Y. Jang, J. Kim, and D. Byun, Invisible metal-grid transparent electrode prepared by electrohydrodynamic (EHD) jet printing, J. Phys. D-Appl. Phys., vol. 46, no. 15, Art. no. 155103, 2013.

[156] K. Kim, G. Kim, B. R. Lee, S. Ji, S. Y. Kim, B. W. An, M. H. Song, and J. U. Park, High-resolution electrohydrodynamic jet printing of small-molecule organic light-emitting diodes, Nanoscale, vol. 7, no. 32, pp. 13410–13415, 2015.

[157] B. H. Kim, M. S. Onses, J. B. Lim, S. Nam, N. Oh, H. Kim, K. J. Yu, J. W. Lee, J. H. Kim, S. K. Kang, C. H. Lee, J. Lee, J. H. Shin, N. H. Kim, C. Leal, M. Shim, and J. A. Rogers, High-resolution patterns of quantum dots formed by electrohydrodynamic jet printing for light-emitting diodes, Nano Lett., vol. 15, no. 2, pp. 969–973, 2015.

[158] M. S. Onses, E. Sutanto, P. M. Ferreira, A. G. Alleyne, and J. A. Rogers, Mechanisms, capabilities, and applications of high-resolution electrohydrodynamic jet printing, Small, vol. 11, no. 34, pp. 4237–4266, 2015.

[159] Y. W. Han and J. Y. Dong, Electrohydrodynamic printing for advanced micro/nanomanufacturing: current progresses, opportunities, and challenges, J. Micro Nano-Manuf., vol. 6, no. 4, Art. no. 040802, 2018.

[160] Y. W. Han, and J. Y. Dong, Fabrication of self-recoverable flexible and stretchable electronic devices, J. Manuf. Syst., vol. 48, pp. 24–29, 2018.

[161] S. Timoshenko, Analysis of bi-metal thermostats, J. Opt. Soc. Am. Rev. Sci. Instrum., vol. 11, no. 3, pp. 233–255. 1925.

[162] AZO materials, Silicone rubber, https://www.azom.com/properties.aspx?ArticleID=920, 2019.

[163] M. L. Ribas, A. Kumar, R. S. Pandher, S. Sarkar, and B. C. Singh, Comprehensive report on low temperature solder alloys for portable electronics, Proceedings of SMTA International, 2015.

[164] Z. X. Wang, A. A. Volinsky, and N. D. Gallant, Crosslinking effect on polydimethylsiloxane elastic modulus measured by custom-built compression instrument, J. Appl. Polym. Sci., vol. 131, no. 22, Art. no. 41050, 2014.

[165] E. Merced, D. Torres, X. B. Tan, and N. Sepulveda, An electrothermally actuated VO2-based MEMS using self-sensing feedback control, J. Microelectromech. Syst., vol. 24, no. 1, pp. 100–107, 2015.

[166] X. T. Tang, K. Li, W. S. Chen, D. Zhou, S. H. Liu, J. G. Zhao, and Y. X. Liu, Temperature self-sensing and closed-loop position control of twisted and coiled actuator, Sens. Actuator A-Phys., vol. 285, pp. 319–328, 2019.

[167] H. A. Sonar, A. P. Gerratt, S. P. Lacour, and J. Paik, Closed-loop haptic feedback control using a self-sensing soft pneumatic actuator skin, Soft Robot., vol. 7, no. 1, pp. 22–29, 2019.

[168] J. Ouyang and Y. Zhu, Z-shaped MEMS thermal actuators: Piezoresistive self-sensing and preliminary results for feedback control, J. Microelectromech. Syst., vol. 21, no. 3, pp. 596–604, 2012.

[169] T. A. Gisby, B. M. O'Brien, S. Q. Xie, E. P. Calius, and I. A. Anderson, Closed loop control of dielectric elastomer actuators, Electroactive Polymer Actuators and Devices (EAPAD) 2011, vol. 7976, Art. no. 797620, 2011.

[170] R. Zhang, P. Iravani, and P. Keogh, Closed loop control of force operation in a novel self-sensing dielectric elastomer actuator, Sens. Actuator A-Phys., vol. 264, pp. 123–132, 2017.

[171] S. Rosset, B. M. O'Brien, T. Gisby, D. Xu, H. R. Shea, and I. A. Anderson, Self-sensing dielectric elastomer actuators in closed-loop operation, Smart Mater. Struct., vol. 22, no. 10, Art. no. 104018, 2013.

[172] G. Rizzello, D. Naso, A. York, and S. Seelecke, Closed loop control of dielectric elastomer actuators based on self-sensing displacement feedback, Smart Mater. Struct., vol. 25, no. 3, Art. no. 035034, 2016.

[173] J. Y. Dong and P. M. Ferreira, Simultaneous actuation and displacement sensing for electrostatic drives," J. Micromech. Microeng., vol. 18, no. 3, Art. no. 035011, 2008.

[174] A. F. M. Sajidul Qadir, Electro-mechanical modeling of SEDM (separately excited DC

motor) & performance improvement using different industrial controllers, Morrisville, NC, USA: Lulu, 2013.

[175] R. Rogers, Building a benchtop PID controller, Keithley Instruments, Inc., Cleveland, OH, USA, 2013.

[176] M. A. Haidekker, Linear feedback controls: the essentials, 1st ed., Waltham, MA, USA: Elsevier, 2013.

[177] D. Chen and D. E. Seborg, PI/PID controller design based on direct synthesis and disturbance rejection, Ind. Eng. Chem. Res., vol. 41, no. 19, pp. 4807–4822, 2002.

[178] K. H. Ang, G. Chong, and Y. Li, PID control system analysis, design, and technology, IEEE Trans. Control Syst. Technol., vol. 13, no. 4, pp. 559–576, 2005.

[179] J. P. Li, J. J. Liang, X. Jian, W. Hu, J. Li, and Q. B. Pei, A flexible and transparent thin film heater based on a silver nanowire/heat-resistant polymer composite, Macromol. Mater. Eng., vol. 299, no. 11, pp. 1403–1409, 2014.

[180] J. J. Bae, S. C. Lim, G. H. Han, Y. W. Jo, D. L. Doung, E. S. Kim, S. J. Chae, T. Q. Huy, N. V. Luan, and Y. H. Lee, Heat dissipation of transparent graphene defoggers, Adv. Funct. Mater., vol. 22, no. 22, pp. 4819–4826, 2012.

[181] R. Whiting, M. A. Angadi, and S. Tripathi, Evaluation of elastic moduli in thin-film/substrate systems by the two-layer vibrating reed method, Mater. Sci. Eng. B, vol. 30, no. 1, pp. 35–38, 1995.

[182] V. E. Sidorov, S. A. Uporov, D. A. Yagodin, K. I. Grushevskii, N. S. Uporova, and D. V. Samokhvalov, Density, electrical resistivity and magnetic susceptibility of Sn-Bi alloys at high temperatures, High Temp., vol. 50, no. 3, pp. 348–353, 2012.

[183] S. H. Song, J. Y. Lee, H. Rodrigue, I. S. Choi, Y. J. Kang, and S. H. Ahn, 35 Hz shape memory alloy actuator with bending-twisting mode, Sci. Rep., vol. 6, Art. no. 21118, 2016.

[184] T. Y. Wang, L. S. Ge and G. Y. Gu, Programmable design of soft pneu-net actuators with oblique chambers can generate coupled bending and twisting motions, Sens. Actuator A-Phys., vol. 271, pp. 131–138, 2018.

[185] B. Gorissen, T. Chishiro, S. Shimomura, D. Reynaerts, M. De Volder, and S. Konishi, Flexible pneumatic twisting actuators and their application to tilting micromirrors, Sens. Actuator A-Phys., vol. 216, pp. 426–431, 2014.

[186] M. Wang, B. P. Lin, and H. Yang, A plant tendril mimic soft actuator with phototunable bending and chiral twisting motion modes, Nat. Commun., vol. 7, Art. no. 13981, 2016.

[187] L. T. de Haan, J. M. N. Verjans, D. J. Broer, C. W. M. Bastiaansen, and A. P. H. J. Schenning, Humidity-responsive liquid crystalline polymer actuators with an asymmetry in the molecular trigger that bend, fold, and curl, J. Am. Chem. Soc., vol. 136, no. 30, pp. 10585–

10588, 2014.

[188] I. Grinberg, N. Maccabi, A. Kassie, and D. Elata, A piezoelectric twisting beam actuator, J. Microelectromech. Syst., vol. 26, no. 6, pp. 1279–1286, 2017.

[189] J. C. Riddick, A. J. Hall, and O. J. Myers, Numerical investigation of the response of active bend-twist PZT actuator, Proceedings of the ASME Conference on Smart Materials, Adaptive Structures and Intelligent Systems, pp. 553–558, 2012.

[190] L. Z. Chen, M. C. Weng, F. Huang, and W. Zhang, Light-and humidity-driven actuators with programmable complex shape-deformations, Sens. Actuator B-Chem., vol. 282, pp. 384–390, 2019.

[191] K. U. Jeong, J. H. Jang, D. Y. Kim, C. Nah, J. H. Lee, M. H. Lee, H. J. Sun, C. L. Wang, S. Z. D. Cheng, and E. L. Thomas, Three-dimensional actuators transformed from the programmed two-dimensional structures via bending, twisting and folding mechanisms, J. Mater. Chem., vol. 21, no. 19, pp. 6824–6830, 2011.

[192] M. Lahikainen, H. Zeng, and A. Priimagi, Reconfigurable photoactuator through synergistic use of photochemical and photothermal effects, Nat. Commun., vol. 9, Art. no. 4148, 2018.

[193] J. N. Ma, Y. L. Zhang, D. D. Han, J. W. Mao, Z. D. Chen, and H. B. Sun, Programmable deformation of patterned bimorph actuator swarm, Natl. Sci. Rev., vol. 7, no. 4, pp. 775–785, 2020.

[194] J. Hu, X. Li, Y. Ni, S. D. Ma, and H. F. Yu, A programmable and biomimetic photo-actuator: A composite of a photo-liquefiable azobenzene derivative and commercial plastic film, J. Mater. Chem. C, vol. 6, no. 40, pp. 10815–10821, 2018.

[195] H. Song, H. Lee, J. Lee, J. K. Choe, S. Lee, J. Y. Yi, S. Park, J. W. Yoo, M. S. Kwon, and J. Kim, Reprogrammable ferromagnetic domains for reconfigurable soft magnetic actuators, Nano Lett., vol. 20, no. 7, pp. 5185–5192, 2020.

[196] L. Liu, S. H. Jiang, Y. Sun, and S Agarwal, Giving direction to motion and surface with ultra-fast speed using oriented hydrogel fibers, Adv. Funct. Mater., vol. 26, no. 7, pp. 1021–1027, 2016.

[197] M. Schaffner, J. A. Faber, L. Pianegonda, P. A. Ruhs, F. Coulter, and A. R. Studart, 3D printing of robotic soft actuators with programmable bioinspired architectures, Nat. Commun., vol. 9, Art. no. 878, 2018.

[198] D. Wang, L. Li, B. Zhang, Y. F. Zhang, M. S. Wu, G. Y. Gu, and Q. Ge, Effect of temperature on the programmable helical deformation of a reconfigurable anisotropic soft actuator, Int. J. Solids Struct., vol. 199, pp. 169–180, 2020.

[199] W. Sang, L. M. Zhao, R. Tang, Y. P. Wu, C. H. Zhu, and J. Liu, Electrothermal actuator on graphene bilayer film, Macromol. Mater. Eng., vol. 302, no. 12, Art. no. 1700239, 2017.

[200] Y. C. Sun, B. D. Leaker, J. E. Lee, R. Nam, and H. E. Naguib, Shape programming of polymeric based electrothermal actuator (ETA) via artificially induced stress relaxation, Sci. Rep., vol. 9, Art. no. 11445, 2019.

[201] C. W. Wang, Y. B. Wang, Y. G. Yao, W. Luo, J. Y. Wan, J. Q. Dai, E. Hitz, K. Fu, and L. B. Hu, A solution-processed high-temperature, flexible, thin-film actuator, Adv. Mater., vol. 28, no. 39, pp. 8618–8624, 2016.